ISSN 1580-2949
UDK 669+666+678+53 MTAEC9, 45(1)1–81(2011)

MATER. TEHNOL.	LETNIK VOLUME 45	ŠTEV. NO. 1	STR. P. 1–81	LJUBLJANA SLOVENIJA	JAN.–FEB. 2011

VSEBINA – CONTENTS

PREGLEDNI ČLANKI – REVIEW ARTICLES

Experimental study of some masonry-wall coursework material types under horizontal loads and their comparison
Eksperimentalna raziskava zgradbe nekaterih zidarskih zidov – vodoravna obremenitev in primerjava uporabljenih materialov
M. Kamanli, M. S. Donduren, M. T. Cogurcu, M. Altin 3

IZVIRNI ZNANSTVENI ČLANKI – ORIGINAL SCIENTIFIC ARTICLES

Synthesis of aluminium foams by the powder-metallurgy process: compacting of precursors
Sinteza aluminijevih pen po postopku metalurgije prahov: stiskanje prekurzorjev
I. Paulin, B. Šuštaršič, V. Kevorkijan, S. D. Škapin, M. Jenko 13

A new method for determining the remaining lifetime of coated gas-turbine blades
Nova metoda za izračun preostale trajnostne dobe lopatic plinskih turbin
L. B. Getsov, P. G. Krukovski, N .V. Mozaiskaja, A. I. Rybnikov, K. A. Tadlja 21

Reduction of ultra-fine tungsten powder with tungsten (VI)-oxide in a vertical tube reactor
Redukcija ultrafinih prahov volframovega(VI) oksida v reaktorju z vertikalno cevjo
Ž. Kamberović, D. Filipović, K. Raić, M. Tasić, Z. Anđić, M. Gavrilovski 27

Oxygen diffusion in the non-evaporable getter St 707 during heat treatment
Difuzija kisika v getru St 707 med toplotno obdelavo
S. Avdiaj, B. Šetina - Batič, J. Šetina, B. Erjavec 33

The modeling of auger spectra
Modeliranje augerjevih spektrov
B. Poniku, I. Belič, M. Jenko 39

Modelling of the directional solidification of a leaded red brass flange
Modeliranje usmerjenega strjevanja prirobnice iz rdeče svinčeve medenine
V. Grozdanić 47

Characterization of the inclusions in spring steel using light microscopy and scanning electron microscopy
Karakterizacija vključkov v vzmetnih jeklih s svetlobno in vrstično elektronsko mikroskopijo
A. Bytyqi, N. Pukšič, M. Jenko, M. Godec 55

Characterization of the carbides in a Ni-Ti shape-memory alloy wire
Karakterizacija karbidov v Žici zlitine s spominom Ni-Ti
M. Godec, A. Kocijan, M. Jenko 61

Fracture toughness of the vacuum-heat-treated spring steel 51CrV4
Lomna žilavost vakuumsko toplotno obdelanega vzmetnega jekla 51CrV4
B. Senčič, V. Leskovšek 67

Similarity criteria and effect of lubricant inertia at cold rolling
Merila podobnosti in vpliv vztrajnosti maziva pri hladnem valjanju
D. Ćurčija, F. Vodopivec, I. Mamuzić 75

IN MEMORIAM

Oskar Kürner 1925–2010 81

UDK 624.04:693:539.4
Review article/Pregledni članek

ISSN 1580-2949
MTAEC9, 45(1)3(2011)

EXPERIMENTAL STUDY OF SOME MASONRY-WALL COURSEWORK MATERIAL TYPES UNDER HORIZONTAL LOADS AND THEIR COMPARISON

EKSPERIMENTALNA RAZISKAVA ZGRADBE NEKATERIH ZIDARSKIH ZIDOV – VODORAVNA OBREMENITEV IN PRIMERJAVA UPORABLJENIH MATERIALOV

Mehmet Kamanli[1], Mahmut Sami Donduren[1], Mustafa Tolga Cogurcu[1], Mustafa Altin[2]

[1]Department of Civil Engineering, Engineering and Architecture Faculty, Selcuk University, 42060 Konya, Turkey
[2]Technical Science College, Selcuk University, 42060 Konya, Turkey
sdonduren@selcuk.edu.tr

Prejem rokopisa – received: 2010-06-11; sprejem za objavo – accepted for publication: 2011-01-11

In this study, the collapsing loads and shear stress of wall samples made of full blend bricks have been examined under horizontal loads within their planes using various bricking types and the results have been compared. To this end, samples were produced using the plain-bricking, lock-bricking and cross-bricking methods. In the performed experimental study, the standard sliding-resistance test technique for the masonry-wall samples was used as recommended in ASTM 1391-81.The behaviours observed with the experimental samples and the cracks that occurred at the end of the experiment were examined and the τ (shear stress) graphs and the horizontal load-displacement graphs were drawn and compared with the experiment results obtained with numerical modelling using the ANSYS program. When these three bricking types were compared, the biggest collapse load occurred for the cross bricking with 240 kN. The biggest shear stress was also found in the cross bricking, with a value of 55 000 kN/mm^2.

Keywords: materials, full blend brick, experimental, lateral load performance, shear stress

Raziskani sta bili rušilna obremenitev in strižna obremenitev zidov iz žgane opeke pri vodoravni obremenitvi v ravnini postavitve opek in primerjani so rezultati. Uporabljeni so vzorci, izdelani z enostavno, krožno in zaprto postavitvijo opek. Uporabljen je preizkus standardne drsne upornosti vzorcev zidov, priporočen v ASTM 1391-81. Vedenje vzorcev in razpoke, nastale na koncu preizkusa, in odvisnosti strižna napetost (τ) ter vodoravna obremenitev – premik so bile določene in rezultati primerjani z rezultati numeričnega modeliranja z uporabo programa ANSYS. Pri primerjavi treh vrst razporeditve opek je bila največja rušilna obremenitev 240 kN pri križni postavitvi. Pri tej postavitvi opeke je bila izmerjena tudi največja strižna sila 55 000 kN/mm^2.

Ključne besede: materiali, žgana opeka, preizkusi, bočna trdnost, strižna napetost

1 INTRODUCTION

Human beings have constructed buildings, bridges, and canals in order to maintain their lives using the existing possibilities and the technology of the day since the earliest times. The oldest building types in the history of humanity are the masonry buildings which are still being used today. Although reinforced concrete and steel constructions are the most common building types of today, masonry buildings are still being constructed in various countries of the world [1].

Especially in rural areas, people prefer masonry buildings for economic reasons, they are easy to construct from the local materials and they can construct buildings in places that are difficult to get at because of geographic conditions. These buildings which are constructed without complying with the existing regulations, getting engineering services and made of heavy and rusty materials are rather weak with respect to horizontal loads [2].

The carrier walls of a masonry building exposed to horizontal loads have two deficiencies. The first one is their failure that is not planar and the cracks are seen here all along the bed joint lines. The second one is planar failure and generally characterized by a diagonal shrinking crack. If the failure which is not planar can be avoided, then the structural resistance is radically affected by the planar behaviour of the cut wall [3].

The vertical carrier elements of masonry buildings are the walls. The horizontal loads may affect these vertical carrier walls due to earthquake, storm, or other reasons besides the vertical loads. In the case that the vertical and horizontal loads have an affect together, a two-axis loading condition occurs on the walls. It is of significant importance to know the behaviour of the wall, which is a composite material under two-axis resistance in terms of providing the loads overlaid on the building to carry securely [2].

The buildings should have the capacity of flexing and absorbing energy when they are exposed to an earthquake impact. This is related to the ductility of the building. As masonry buildings are rigid and friable, they have no capacity of flexing and absorbing energy like flexible buildings. Eventually, they are exposed to major horizontal forces as their capacity to decrease the energy

exposed during the earthquake is low. Furthermore, they demonstrate unwanted behaviours in term of engineering due to the fact that the materials used with masonry buildings are friable and cause sudden cracks and breaks when they go beyond their loading limits. Because of these reasons, masonry buildings cannot be considered as buildings that are resistant to an earthquake. Nevertheless, masonry buildings should not be completely perceived as negative buildings in terms of an earthquake. Just like all other buildings, masonry buildings can be strong and secure provided that they are built in compliance with the standards, regulations and engineering studies are applied. Masonry houses such as earthen, brick and stone structures are composed of building blocks with weak inter-binding action which have low tension capacity [19].

Before starting the improvement and strengthening activities for a masonry building, the earthquake behaviour of the masonry building exposed to an earthquake and their collapsing mechanism should be well known. The earthquake behaviours of masonry building are diverse although they have similarities in comparison with reinforced concrete buildings. It can be said that the most impressive difference is the break of the masonry wall in the out of plane direction. The cutting forces and moments are constituted with masonry walls under horizontal loads. Therewith, the in-plane break of the masonry wall occurs by axial pressure/tensile forces formed by the moment and/or the slant inert tension effects the created moment [2].

Several studies have been carried out related to the behaviours of masonry buildings. A multi-surface plastic has been used so as to define the pressure, cut and resisting behaviours of the filling plaster using an interesting approach developed by Laurence [6,7] and modelled by an interface element. Gamboratta and coworkers have generated a model evaluating the constructive parity of the interface in terms of two internal variables representing the friction surface and the filling plaster damage using a similar approach [5]. This model has been broken under the stretching resistance and shown a decreasing hardness and friction distribution. This feature is used with the definition of hysteretic planar behaviours of masonry building walls. These that have experienced earthquakes have damaged constructions significantly and caused the deaths of thousands of people [20].

The above-mentioned numerical procedures are quite effective and take many facts which are seen with the behaviours of masonry building. However, their application is figuratively very difficult. In addition to these, a few more simple methods are available. For instance, the homogenization application or anisotropy elasto-plastic foundation equalities [3], which are some of the approaches [4,8] based upon the crack modelling of masonry buildings, are much simpler methods.

The horizontal loads occurring during earthquakes reveal strong planar and non-planar forces on these walls. The behaviour and the damages to these constructions under seismic forces are relatively big [7]. The walls in the direction of the shearing force have a big role in increasing the seismic force durability [15]. The majority of the existing buildings in this region have not been designed to withstand earthquakes. Most of them are typically unreinforced masonry, low-rise buildings and have been exiguously designed [16]. They showed poor performance during earthquakes and most of the damage and casualties resulted from these structures. However, in terms of earthquake engineering, significant lessons were learned from the surveys of damaged masonry buildings after earthquakes [17]. Damage and losses arising from landslides can include cracks in the masonry, damage to the electricity and water supply, subsidence or at worst the complete collapse of buildings [18].

Masonry building constructions constitute a significant part of the construction inheritance in the world. Actually, the structural walls of these buildings have been designed so as to resist the force of gravity. The horizontal loads incurred by earthquakes reveal strong planar and non-planar forces with these walls. The damage that occurs in these buildings under seismic forces are relatively big [2]. **Figure 1** shows some pictures of masonry buildings that were damaged after the Sultandagi-Cay Earthquake, 2002.

The masonry buildings are built with different rows and bricking forms positioning the bricks end-to-end and side by side in a net way. In this study, the lock bricking, cross bricking and plain bricking, which are some of the most commonly used bricking types in the world, are compared. The plain bricking is formed by plain rows which are piled over and over. The second row is started with a half brick and the vertical sutures are ensured not to match up with each other (**Figure 2**).

The lock bricking is formed by placing the rows over each other by sliding a quarter brick. In order to provide a quarter-brick sliding, the second row is completed flatways and two pieces of three quarter brick are

Figure 1: Some damaged masonry buildings[14] (Sultandagi-Cay Earthquake, 2002)
Slika 1: Nekaj zgradb, poškodovanih v potresu Sultanagi-Cayju, 2002 [14]

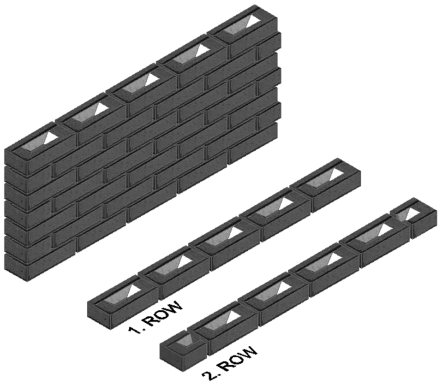

Figure 2: Plain Knitting
Slika 2: Enostavna postavitev opek

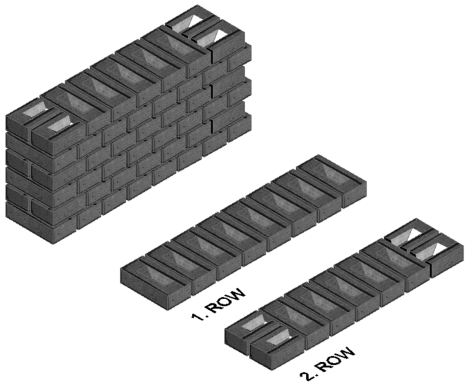

Figure 3: Lock Knitting
Slika 3: Zaporna razporeditev opek

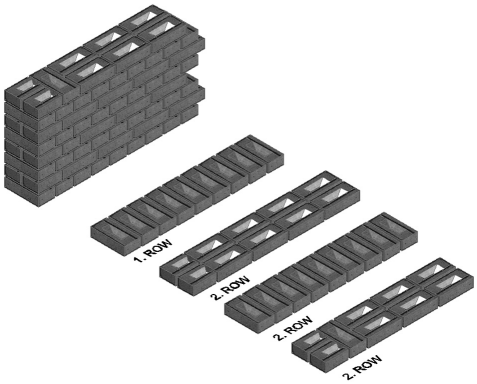

Figure 4: Cross Knitting
Slika 4: Križna postavitev opek

positioned flatways at the end. It is used to brick the plain and curved walls with a one brick thickness (**Figure 3**).

The cross bricking is made using lock and plain rows. The vertical sutures of the plain rows are skidded by half a brick from the vertical sutures of the plain row right under. Hence, the cross images are displayed on the surface of the wall (**Figure 4**). It is used for bricking in one-brick thickness or more thickness walls [5].

In this study a simple numerical modelling is recommended with an experimental approach in order to research the shear behaviours of the horizontal loads of

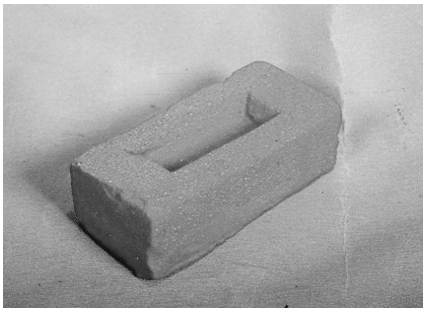

Figure 5: Full Blend Brick
Slika 5: Žgana opeka

walls made of full blend bricks within their planes. The wall samples prepared for this purpose were tested to see how they are forced to collapse and the shear stress of the wall samples in the non-linear zones and the change of the shear rigid of the wall sections were determined. The numerical modelling was performed using the ANSYS program with the finite elements taking into account the local mechanics parameters of the brick and plaster. The results that were obtained at the end of the modelling and the results obtained from the experiments were compared.

2 THE FEATURES OF THE USED MATERIALS

2.1 The features of the full blend brick

Full blend bricks were used in the experiments (**Figure 5**). The average pressure resistance of the bricks is 12 MPa; the elasticity module is 3 000 MPa and the tensile strength is 0.9 MPa. While calculating the average pressure resistance, the gross area of the brick is the area where the pressure force affects and a very neat distribution is ensured, neglecting the pressure resistance values of the samples from the ones too high and too low.

2.2. Features of the plaster

The same type plasters whose volumetric composition rates have been used in the production of the wall samples were employed. The cement, sand, water volumetric composition rate of this plaster has been produced as 5 : 15 : 3 ratio. The calculated pressure resistance of the used plaster is 2.26 MPa and the tensile strength at bending is 1.64 MPa. The plaster thickness was 3 cm.

3 EXPERIMENTAL STUDY

3.1 Features and production of experimental samples

A total of 9 pieces of samples with 600 mm × 600 mm × 200 mm sizes have been produced, with 3 from each of the various bricking types. The vertical and horizontal suture thickness of the samples was about 10 mm. Although the calculation methods in the ASTM

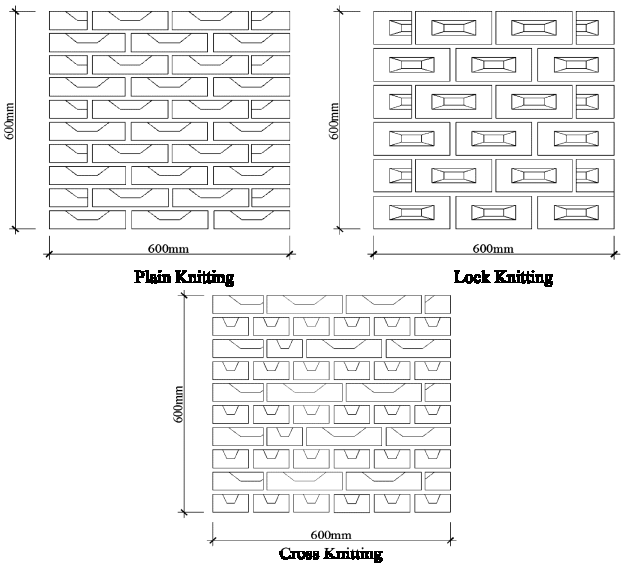

Figure 6: Bricking Types
Slika 6: Vrste križne postavitve opek

1391-81 are used [13], the sample size has been selected as 600 mm instead of 1200 mm, which is the sample size recommended in this standard taking into account the sizes of the bricks and the laboratory conditions (**Figure 6**).

All the samples were prepared in the laboratory under the same conditions. The full blend bricks were used in the formation of all the samples. The prepared plaster to brick the samples is also used in the same proportion. The wall samples were produced using the very first prepared plaster, according to the bricking rules (**Figure 7**). After completion of the wall bricking process, the plaster mortar was formed using the same composition rates and the facing process was started; after realizing the watering process for 7 days, they were left to dry for 3 days. The samples whose watering and drying process were completed have been made ready for the experiment by painting them using whitewash prepared in the laboratory.

3.2 Experimental technique and program

In this study, carried out for the purpose of finding the sliding resistance of the wall samples produced with full blend bricks using various bricking type, the force controlled experiment technique was used, trying to maintain the force increment rate. The displacements on the samples during the experiment were measured using ten units of Linear Variable Displacement Transducers. A vertical pressure force was applied to the wall samples whose horizontal sutures are positioned to make an angle of 45° by loading, and the breaking loads, breaking shapes, crack relieves and the displacement readings with the increasing load stages were recorded.

3.3 Experiment setup and loading

Two pieces of steel heads were made to provide the samples to stand at 45° angle vertically. A surface made of plaster of Paris was prepared inside the lower head standing in its guide and the wall sample was positioned to the head in its plumb line (**Figure 8**). Also preparing the surface made of plaster of Paris in the upper head, the upper head was placed on the sample. Keeping the sample in its plane during the loading was ensured by the metal arms pulled up the front and back of the sample, as illustrated in **Figure 8**. In order to decrease the frictional effect between these metal arms and the sample, the slipperiness of it was increased, putting oil to the interfaces.

The vertical load on the experimental samples was applied by means of a 500 kN capacity manual hydraulic jack. A steel plate was placed on the steel upper head in order to adjust the level of the height and a hydraulic jack was placed right on it. The value of the applied load was measured using a 500 kN capacity load cell.

3.4 Collection of the experimental data and measuring system

The load measuring was carried out by using load cells and the displacements by LVDT displacement meters in all the experiments. The values that these devices read were instantly transferred to the computer by means of a data-logger system called CoDA and taken under records. All the values read from the

Figure 7: Production of the samples
Slika 7: Izdelava preizkušancev

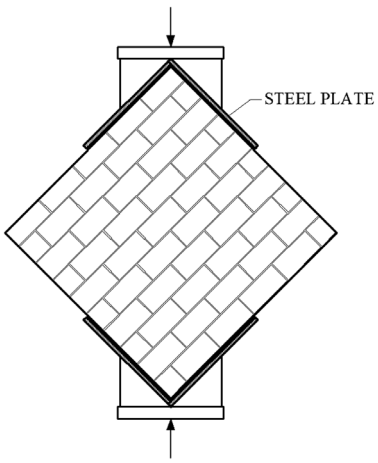

Figure 8: Loading form of the experimental samples
Slika 8: Način obremenitve preizkušancev

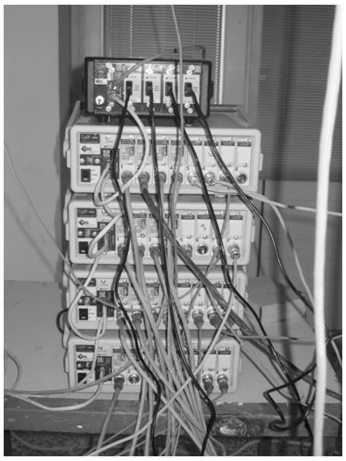

Figure 9: Data-collecting system
Slika 9: Sistem za zbiranje podatkov

channels are recorded to computers immediately and also all the readings taken from the requested channels can be monitored in graphics. All the print outs of the taken readings are in the form to be read by the "EXCEL" program. The data-collecting system used for the evaluation of the readings taken from the load cell and the LVDTs and the computer set up are shown in **Figure 9**.

The displacement readings with all the experiments were carried out using ten units of LVDT (Linear Variable Displacement Transducer). Two units of displacement transducers were placed on each surface of the front and back of the wall samples each, two displacement transducers on the loading axis and two units of displacement transducers in the vertical direction to the loading axis. Furthermore, two units of displacement transducers were placed on the front side of the sample in order to control the movement out of plane. The layout diagram and the illustration of the displacement transducers are given in **Figure 10**. Here, the direction of the arrows shows the approach direction

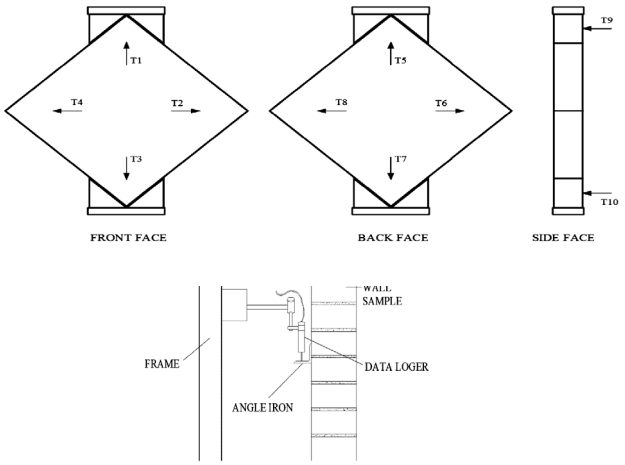

Figure 10: The layout diagram of the displacement transducers
Slika 10: Razporeditev transduktorjev premikov

to the panel consisting of the displacement transducers' measuring points.

The data read by the displacement transducers numbered T9 and T10 during the experiments are constantly controlled and the movement of the sample out of the plane is provided to be within the certain limits.

3.5 Experimental work

A total of 9 experiments – 3 from each bricking type – have been carried out in order to compare some of the bricking types in terms of horizontal load-bearing capacity and cutting force. The pictures of the samples before and after the experiment are given in **Figure 11**. The loading was accomplished with approximately 10 kN load steps and the displacement measuring was taken right after each step.

3.6 Modelling and numerical interpretation

For the finite-element modelling (FEM) of the masonry prisms, SOLID45 elements in the ANSYS element library were used for the 3-D modelling of the solid structures. The element is defined by eight nodes having three degrees of freedom at each node: translations in the nodal x, y, and z directions. The element has plasticity, creep, swelling, stress stiffening, large deflection, and large strain capabilities. The element is defined by eight nodes and the orthotropic material properties. With using this element, the analysis cannot capture the bending behaviour with a single layer of elements. In the loading system of these studies there are no bending effects on the masonry infill and the SOLID 45 elements are suitable for the analysis [9].

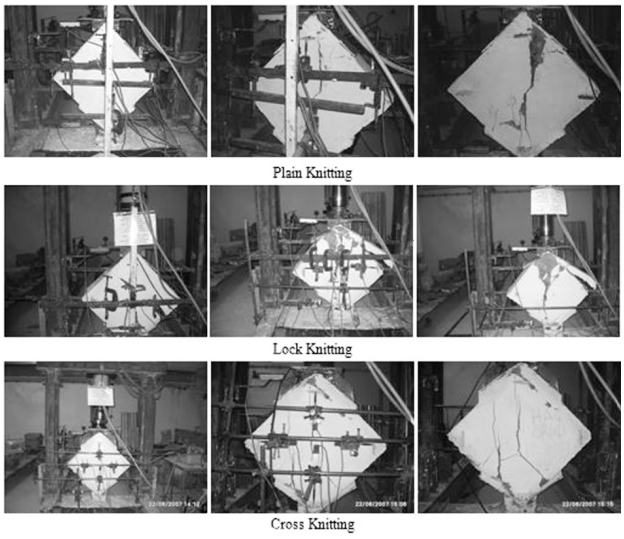

Figure 11: The pictures of the plain-, lock- and cross-bricking samples during the experiment
Slika 11: Posnetki preizkušancev z enostavno, zaporno in križno razporeditvijo opek med preizkusom

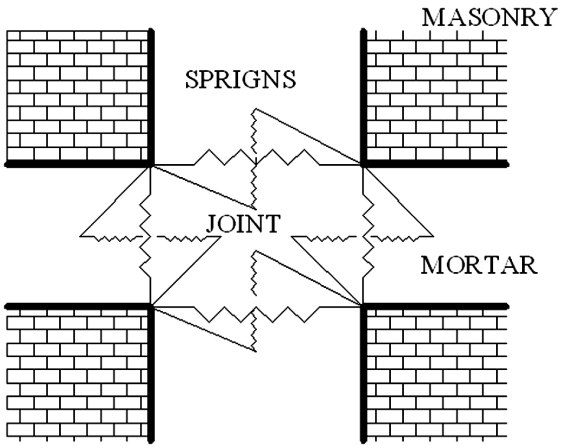

Figure 12: Mortar-brick joint interface modelling
Slika 12: Modeliranje povezave med opeko in malto

The masonry units and mortar layers are modelled independently and different material properties are obtained. In the elaborate FE model developed in this study, masonry units are linked to the mortar units by a series of nonlinear springs, which is also available in the ANSYS library. COMBIN39 is a unidirectional element with nonlinear generalized force-deflection capability that can be used in every analysis. The longitudinal option is a uniaxial tension-compression element with up to three degrees of freedom at each node: translations in the nodal *x*, *y*, and *z* directions. No bending or torsion is considered. The element has a large displacement capability for which there can be two or three degrees of freedom at each node.[10] The element is defined by two (preferably coincident) node points and a generalized force-deflection curve. The springs are introduced to handle the tensile and shear stress failure in the mortar joints, **Figure 12**.

The material model for the masonry panel was assumed to be orthotropic parallel and normal to the bed joints.[11] The material stress versus strain relationship is represented in **Figure 13**.

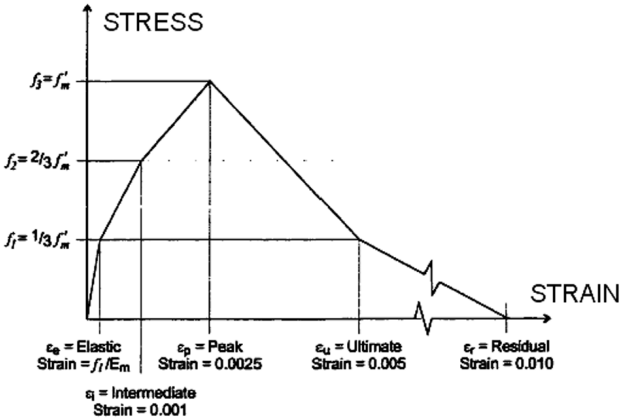

Figure 13: Stress versus strain relationship
Slika 13: Odvisnost napetost – deformacija

The incremental full Newton-Raphson iterative solution procedure was used in order to account for both large deformation effects and the material plasticity. In order to capture the complete load-deflection behaviour including the post peak response, the top node of the masonry prism was subjected to a vertical downward displacement.[12]

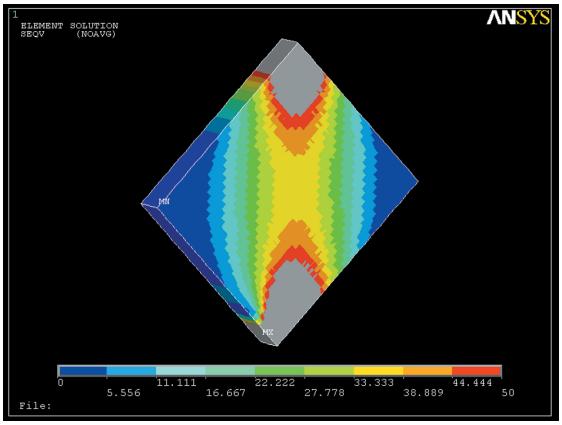

Figure 14: Von-Misses Stress distribution for specimen type 1
Slika 14: Von-Misesova razporeditev za vzorec 1

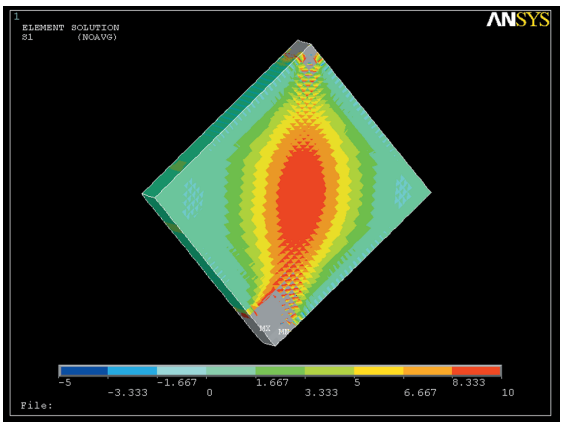

Figure 15: Principal Stress distribution for specimen type 1
Slika 15: Razporeditev glavnih napetosti za vzorec tipa 1

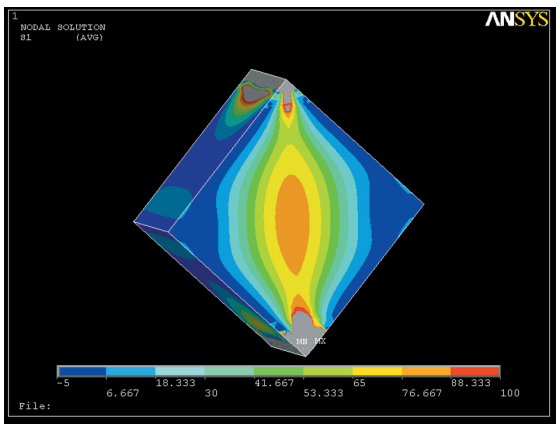

Figure 16: Von-Misses Stress distribution for specimen type 2
Slika 16: Von-Misesova razporeditev za vzorec 2

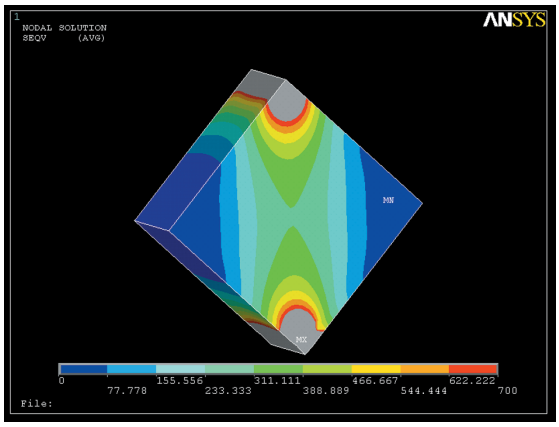

Figure 17: Principal Stress distribution for specimen type 2
Slika 17: Razporeditev glavnih napetosti za vzorec tipa 2

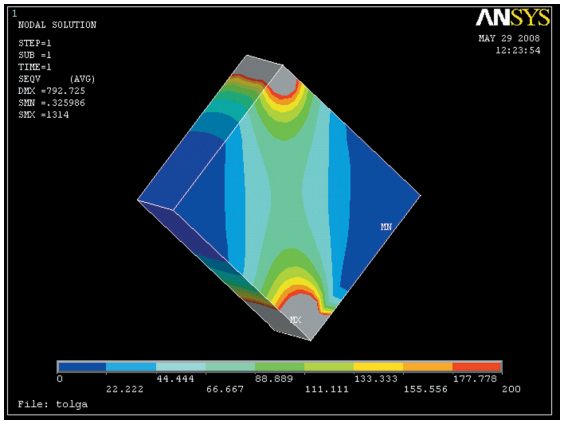

Figure 18: Von-Misses Stress distribution for specimen type 3
Slika 18: Von-Misesova razporeditev za vzorec 3

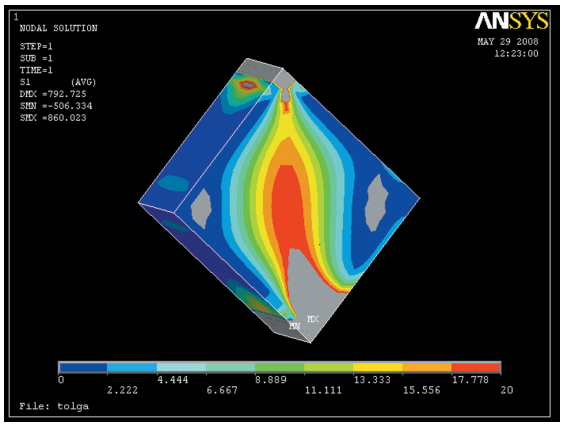

Figure 19: Principal Stress distribution for specimen type 3
Slika 19: Razporeditev glavnih napetosti za vzorec tipa 3

The Von-Misses stress distribution and principal stress graphics for the loaded masonry panels are represented in **Figure 14 through 19**. The applied maximum displacement level is chosen for comparison purposes. (Type 1: Plain Knitting, Type 2: Cross Knitting, Type 3: Lock Knitting).

3.7 Behaviours of the experimental samples and the experimental results

The first crack in the sample reached to the biggest collapsing load with the plain bricking samples occurred at around 40 kN. The first cracks started from the top-left side of the sample and continued downwards. The maximum collapsing load was monitored to be 60 kN and a break on the top-right of the sample is seen.

The first crack in the sample carried the biggest collapsing load with the lock-bricking samples occurred at 100 kN. This crack is formed on the right-bottom side of the sample. The loading was continued and the sample started not to carry the load at 160 kN and broke at the right-top side.

The first crack in the sample where the maximum collapsing load is obtained with the cross-bricking samples occurred on the right-top side of the sample at 170 kN. The collapsing load was determined to be 240 kN. The sample was broken from the right-top side.

The horizontal load-displacement graphics of the plain-, lock- and cross-bricking samples is given in **Figure 20**.

3.7.1 The comparisons among the bricking types

a) Comparison in terms of horizontal load-displacement

The samples reaching to the biggest collapsing load out of the plain-, lock- and cross-bricking samples were

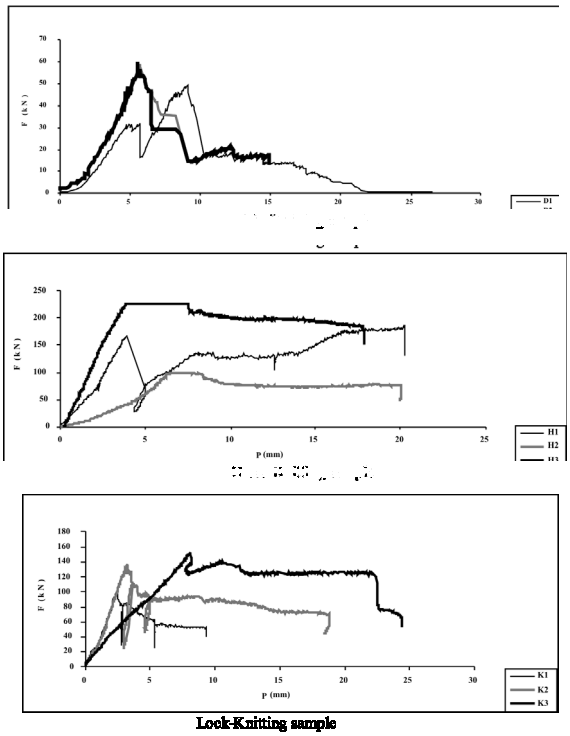

Figure 20: The horizontal load-displacement graphics of the plain-, lock- and cross-knitting samples
Slika 20: Odvisnost vodoravna obremenitev – premik za enostavno, zaporno in križno razporeditvijo opek

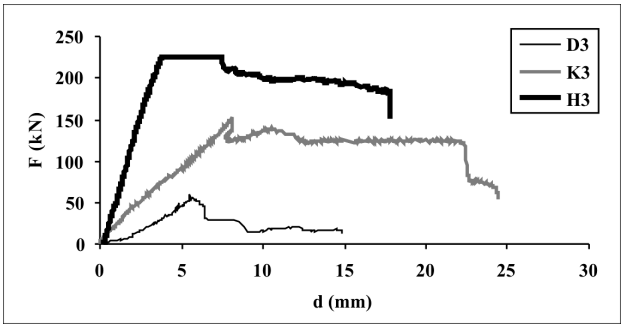

Figure 21: The comparisons of the horizontal load-displacement graphics
Slika 21: Primerjava največje rušilne sile za 3 vrste postavitve opek

compared in terms of the horizontal load-displacement. The comparisons of the horizontal load-displacement graphics obtained from the biggest collapsing load in 3 bricking types are given in **Figure 21**.

b) Comparison of the shear resistance-displacement

While the shear force is determined from the plain-, lock- and cross-bricking samples, the displacement values have been dictated finding out the average of the T1-T3 LVDT reading values and the T2-T4 LVDT values. The sliding resistance was obtained by taking the Cos45 value of the load and dividing it by the area. The shear resistance-displacement graphics obtained in this way are given in **Figure 22**.

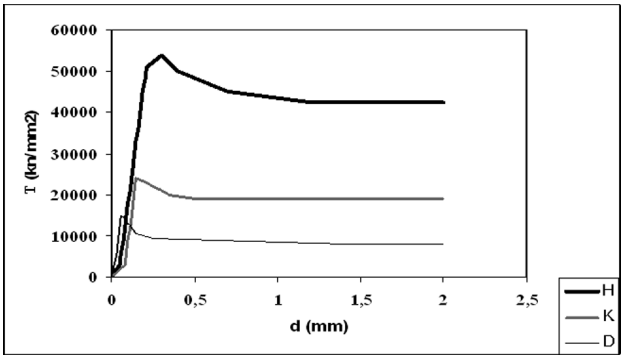

Figure 22: The shear resistance-displacement graphics
Slika 22: Odvisnosti strižna sila – premik

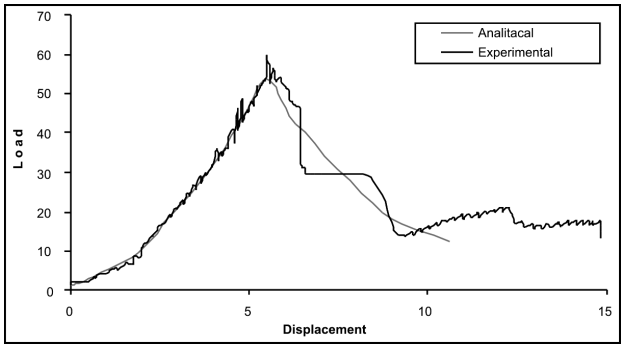

Figure 23: Load versus displacement comparison for specimen type 1
Slika 23: Primerjava breme – premik za vzorec tipa 1

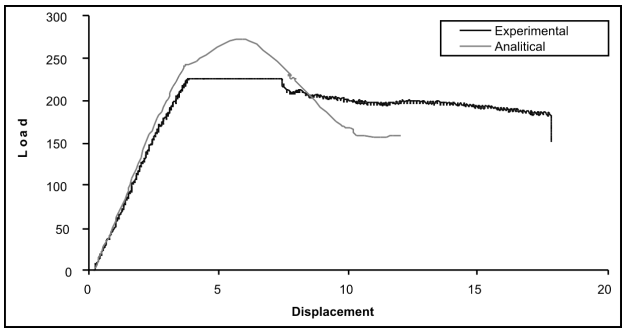

Figure 24: Load versus displacement comparison for specimen type 2
Slika 24: Primerjava breme – premik za vzorec tipa 2

c) Comparison related to the Numerical Modelling

The magnitude of this displacement was sufficiently greater than that observed in the actual test, after which a load-deflection plateau was attained indicating that the contribution of the infill almost entirely diminished and that no appreciable increase in the load resistance occurred. The three different masonry configurations are modelled and loaded in time steps, and the applied vertical load versus displacement values are obtained. The comparison of the analytical and experimental data is represented in **Figure 23, 24 and 25**.

4 DISCUSSION AND CONCLUSION

The total of 9 units of samples made up of three different bricking types to be used in the formation of a masonry building were compared in terms of the horizontal load and shear force using a standard sliding resistance experiment technique for the masonry-wall samples recommended in ASTM 1391-81, and the following outcomes have been obtained. The analytical results obtained by the solution with the finite-element method together with the results obtained as a result of the experiments were evaluated. The results are as follows:

The biggest collapsing load occurred with the cross bricking as per the horizontal loads. The collapsing load with this type of bricking is 240 kN. The collapsing load

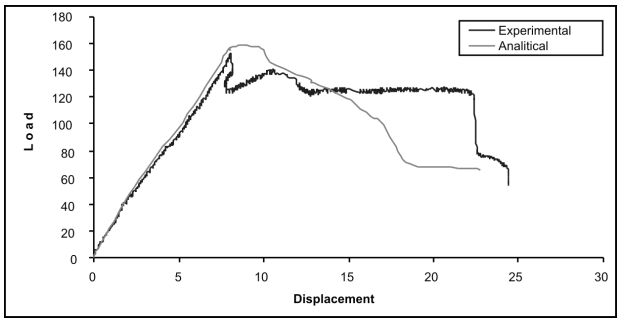

Figure 25: Load versus displacement comparison for specimen type 3
Slika 25: Primerjava breme – premik za vzorec tipa 3

with the lock bricking is 160 kN, and the plain bricking is found to be 60 kN.

It was determined that the strength of the shear stress formed in cross knitting is 2.25 times higher than lock knitting and 3.6 times more than plain knitting.

When horizontal load displacement graphs are taken into consideration, it was found that the energy-absorption capacity is 3 410 kN mm in cross knitting, 2 420 kN mm in lock knitting and 625 kN mm in plain knitting. It was concluded that cross knitting consumed 1.4 times more energy than lock knitting, whereas it consumed 5.8 times more energy than plain knitting.

According to the horizontal load-displacement graph, the displacement ductility of the cross-knitting wall was 19 mm, that of the lock-knitting wall was 23 mm and that of the plain-knitting wall was 14 mm.

The values obtained analytically by using the finite-elements method (ANSYS) were in accordance with the ones obtained as a result of the experiments.

5 CONCLUSIONS

When the results of both the empirical and analytical studies on the samples formed by using different knitting types were evaluated, a masonry construction with cross knitting is considered to be the most suitable knitting type in terms of collapse load, shear stress, and energy-absorption capacity. Although the collapse load of lock knitting is low, its displacement ductility is higher than other knitting types. It was observed that plain knitting has the lowest values among the other knitting types. These results show that different knitting types used in the masonry constructions of rural regions have an important role in the protection of the construction against earthquakes. Using a cross-knitting type in masonry constructions in rural regions that are especially at risk of earthquakes will make the construction more resilient to earthquake damage.

6 REFERENCES

[1] E. Yokel, S. G. Fattal, Failure hypothesis for masonry shear walls Journal of the Structural Division, ASCE, 102 (**1976**) ST3, 515–532

[2] R. Kanit, E. Atimtay, et al., The Experimental behavior of the masonry walls which are loaded out of plane, YDGA The Increase in the earthquake security of the Masonry Buildings Workshop, ODTÜ, 17th February, 2005, Ankara

[3] J. Lopez, S. Oller, E. Onate, J. Lubliner, Homogenous constitution model for masonry Int. J. Numer Meth Eng., 41 (**1999**), 1651–71

[4] J. Lee, G. Pande, J. Midleton, B. Kralj, Numerical modelling of brick masonry panels subject to lateral loadings, Comput. Struct., 61 (**1996**) 4, 735–45

[5] L. Gambarotta S. Lagomarsino, Damage models for the seismic response of brick masonry walls. Part I: the mortar joint model and its applications. Earthquake Eng Struct Dynamics, 26 (**1997**), 423–39

[6] P. Laurence, J. Rots, Multisurface interface model for analysis of masonry structures. J. Eng. Mech., 123 (**1997**) 7, 660–8

[7] P. B. Laurence, Computational strategles for masonry structures. Ph. D. Thesis, The Netherlands :Technical Universitiy Delft, Delfth University Pres: ISBN 90-407-1221-2 (1996)

[8] R. Luciano, E. Sacco, Homogenization technique and damage model for old masonry model Int. Solid Struct., 34 (**1997**) 24, 3191–208

[9] A. Gabor, A. Bennani, E. Jacquelin, F. Lebon, Modelling aapproaches of the in-plane shear behaviour of unreinforced and FRP strengthened masonry panels. Composite Structures, (**2005**), 277–288

[10] D. Abruzzese, L. Miccoli, J. Yuan, Mechanical behavior of leaning masonry, Huzhu Pagado Journal of Cultural Heritage, (**2009**), 480–486

[11] M. Fathy, J. Planas, M. Sancho, A numarical study of masonry cracaks, Engineering Failure Analysis, (**2008**), 675–689

[12] V. Mallardo, R. Malvezzi, E. Milani, G. Milani, Seismic vulnerability of historical masonry buildings: A case study in Ferrara, Engineering Structures, (**2007**), 2223–2241

[13] ASTM 1391-81 Standard test method for diagonal tension (shear) in masonry Assem-Blages

[14] M. Y. Kaltakci, M. H. Arslan, H. H. Korkmaz, M. Kamanli, Failure of superstructures after the February 03, 2002 Sultandagi-Cay Earthquake, Journal of Engineering and Applied Sciences, 2 (**2007**) 10, 1569–1575

[15] A. Gabor, E .Ferrier, E. Jacquelin, P. Hamelin, Modelling approaches of the in-plane shear behaviour of unreinforced and FRP strengthened masonry panels, Composite structures, (**2005**), 277–288

[16] K. Korkmaz, Seismic safety assessment of unreinforced masonry low-rise buildings in Pakistan and its neighbourhood, Nat. Hazards Earth Syst. Sci., 9 (**2009**), 1021–1031

[17] H. Ramazi, H. S. Jigheh, The Bam (Iran) earthquake of December 26, 2003: From an engineering and seismological point of view, J. Asian Earth Sci., 27 (**2006**), 576–584

[18] A. Blöchl B. Braun, Economic assessment of landslide risks in the Swabian Alb, Germany – research framework and first results of homeowners and experts surveys, Natural Hazards and Earth System Sciences, 5 (**2005**), 389–396

[19] H. H. Korkmaz, S. Z. Korkmaz, M. S. Donduren, Earthquake hazard and damage on traditional rural structures in Turkey, Natural Hazards and Earth System Sciences, 10 (**2010**), 605–622

[20] M. Kamanli, F. S. Balik, The behaviour of roof gable walls under the effect of earthquake load, Natural Hazards and Earth System Sciences, 10 (**2010**), 1–13

UDK 66.017:669.715:621.746
Original scientific article/Izvirni znanstveni članek

ISSN 1580-2949
MTAEC9, 45(1)13(2011)

SYNTHESIS OF ALUMINIUM FOAMS BY THE POWDER-METALLURGY PROCESS: COMPACTING OF PRECURSORS

SINTEZA ALUMINIJEVIH PEN PO POSTOPKU METALURGIJE PRAHOV: STISKANJE PREKURZORJEV

Irena Paulin[1,2], Borivoj Šuštaršič[2], Varužan Kevorkijan[3], Srečo D. Škapin[4], Monika Jenko[2]

[1]TALUM, d. d., Kidričevo, Tovarniška cesta 10, SI-2325 Kidričevo, Slovenia
[2]Institute of Metals and Technology, Lepi pot 11, SI-1000 Ljubljana, Slovenia
[3]Independent Researcher, Betnavska cesta 6, SI-2000 Maribor, Slovenia
[4]Jozef Stefan Institute, Jamova 39, SI-1000 Ljubljana, Slovenia
irena.paulin@imt.si

Prejem rokopisa – received: 2010-12-20; sprejem za objavo – accepted for publication: 2011-01-19

Aluminium foams, produced by the powder-metallurgy route, have a good potential for use in weight-sensitive structural parts. The goal of this study was to evaluate the properties and to optimize the preparation of precursors by a powder-compacting process. Various compacting pressures, from 200 MPa to 900 MPa, were used in the double-axial powder-compacting process for two different aluminium powders: pure aluminium and an AlSi12 alloy with the addition of 1 % of TiH_2 as a foaming agent. The green density of the precursors and the distribution of the foaming agent were examined. The powder particles was also characterised. The results of the effective preparation of precursors are shown as the effectiveness of the foaming of the precursors.
The relation between the powder characteristics, the aluminium-alloy properties and the preparation of precursors was studied by SEM/EDS analysis, powder-metallurgy standard testing of metallic powders, granulometry, etc. Different parameters were used for the precursor preparation and foaming. The foaming temperature varied between 680 °C and 770 °C, and the foaming time was from 6 min to 13 min. The relation between the properties and the applied production parameters was studied in detail and is described in this paper.

Keywords: aluminium foam, Al, AlSi12 alloy, powder-metallurgy, powder compacting, sintering

Aluminijeve pene, narejene po postopku metalurgije prahov, imajo velik potencial v uporabi lahkih konstrukcij. Cilj raziskave je ugotoviti lastnosti in parametre za optimizacijo priprave prekurzorja po postopku hladnega stiskanja. Za pripravo prekurzorjev smo uporabili obojestransko stiskanje s tlaki od 200 MPa do 900 MPa. Stiskali smo mešanico prahov tehnično čistega aluminija 99,7 % in zlitine AlSi12, v obeh primerih z dodatkom 1 % TiH_2 kot penila. Določili smo zelene gostote in porazdelitev penila v prekurzorjih. Naredili smo tudi karakterizacijo vseh treh uporabljenih prahov kot vstopnega materiala. Rezultat uspešne priprave prekurzorjev se kaže v uspešnosti penjenja materiala.
Povezavo med lastnostmi prahov, lastnostmi aluminijevih zlitin in priprave prekurzorjev smo raziskovali s SEM/EDS-analizami, s preizkušanjem prahov s standardnimi metodami, uveljavljenimi v metalurgiji prahov, granulometrijo itd. Uporabljeni so bili različni parametri za pripravo in penjenje prekurzorjev. Temperature penjenja so bile med 680 °C in 770 °C, čas penjenja pa med 6 min in 13 min. Povezava med lastnostmi in uporabljenimi parametri za pripravo aluminijevih pen je bila raziskana in je podrobno opisana v tem članku.

Ključne besede: aluminijeve pene, aluminij, zlitina AlSi12, metalurgija prahov, stiskanje prahov, sintranje

1 INTRODUCTION

Aluminium foams are metallic materials with various physical and chemical properties that can be used for several purposes[1,2]. Production methods can be classified into four groups: powder-metallurgy (PM), molten-metal foaming, metallic deposition, and sputter deposition[3]. Each production method gives its own characteristic range of densities, cell sizes and shapes. In this study a method that is adapted to produce complex shapes of metallic foams is discussed, i.e., the powder-metallurgy process.

PM is one of the possible techniques to produce metallic foams. This production process is not as widely used as the less-expensive, molten-metal foaming process, but it also has advantages [4,5]. Its general application in the metal-foaming industry is not very extensive due to the relatively high costs of the input materials. The principle of PM is simple and the process consists of three stages: 1) mixing the metallic powder and the powder of the foaming agent, usually TiH_2, ZrH_2, etc; 2) compacting the powder mixture and; 3) sintering as the final stage of the process. All three steps are important for the quality of the final production and the properties of the aluminium-foam products.

The first step of the PM process is mixing of the metallic powder and the powder of the foaming agent in the proportions needed for the final properties of the product. The higher is the fraction of foaming agent, the greater and/or more numerous are the pores. The addition of the powder ceramic compounds (SiC, CaO) is desired for the stabilization of the foams, but this is not essential [6–8]. The important task of mixing is to achieve a

homogeneous distribution of foaming-agent particles and of the ceramic-powder particles if they are added.

The next important step of the foaming process is the compacting of the powder mixture. The density of the compacted material, the so-called green or theoretical density, is a significant property of precursors and it must be very high (up to 99 %). The shape and size of the metallic-powder particles plays an important role in achieving the highest possible green density of the precursors. However, depending on those properties of the powders, various angles of the repose and bulk densities are achieved. The green density of the precursors also depends on the possible plastic deformation of the metallic powder particles. The lower is the porosity of the precursors, the more of the liberated gas during the sintering is captured in the matrix material.

Sintering is the final stage of the PM production process. During the sintering process at a temperature that is above the temperature of the melting point, and which is specific for each alloy and depends on the foaming agent used, hydrogen is released from the hydride and forms pores in the material. A larger fraction of liberated gases is captured in the matrix material if the molten metal has a higher viscosity [9–11].

The sintering time varies from 3 min up to 10 min, depending on the alloy used for foaming, the foaming agent and the size of the sintered piece. In the decomposition of the TiH_2 used as a foaming agent, the Ti remains and hardens the matrix material while the hydrogen captured in the matrix forms foams with closed-cell structures.

In this study we have focused on the second stage of the PM process. The production of precursors by compacting powder mixtures can be performed in a variety of ways, e.g., by uni-axial, double-axial or isostatic pressing, extrusion, rolling, etc., and all the methods can be hot or cold. Furthermore, the compacting process can be performed in an inert atmosphere, in air or in vacuum [12]. The most economical way is double-axial pressing in air, but the most efficient one is high-temperature extrusion.

2 EXPERIMENTAL WORK

The PM foaming process was applied in our research work. Air-atomized Al powder with a purity of 99.7 % and a D_{50} of 98 μm, air-atomized AlSi12 alloy powder with D_{50} of 42 μm, and TiH_2 powder with a purity of 98 % and a D_{50} of 12.6 μm were used as the starting materials (the purity was specified by manufacturer). The metallic powders were prepared as Ecka granules (Non Ferrum Kranj, d. o. o.), while the TiH_2 powder (325 mesh, 98 %) was purchased from the Sigma-Aldrich Company. In all cases, the metallic powder was mixed with mass fraction 1 % of TiH_2 powder in a turbular mixer (TURBULA WAB Type T2C, 50 Hz, 180 W) for an hour. The characteristics of the powders are shown in **Table 1**. The size and the distribution of the powders were determined by laser granulometry (Alcatel CILAS HR 850-B, isopropanol as analysis medium).

The bulk density, tapped density and free-flowability of the powders were determined. The free-flowability and the bulk density of the powders were determined by the Hall flowmeter funnel that contains a standard flowmeter funnel for metallic powders [13]. A dry test specimen must be carefully loaded into the flowmeter funnel and permitted to run into the density cup through the discharge orifice. In order to determine the free-flowability of the powders it is necessary to measure the time needed for 50 g of powder to pass through the orifice. When the bulk density is determined the powder must completely fill the density cup till it starts to overflow, then the powder is levelled with the top of the cup using a spatula with a blade held perpendicular to the top of cup. Afterwards, the powder is weighed. For a determination of the powder's tapped density a standard mechanical device is used that enables tapping of the graduated cylinder containing powder at a rate of 100 taps per minute [13]. The analyzed powder must be weighed (50 g) and the volume of the powder is read after the tapping.

Powder mixtures were compacted cold, using a double-axial compaction, in a 24-mm-diameter, lubricated, tool-steel die with pressures in the range from 200 MPa to 900 MPa to achieve different green densities [14]. The samples were compacted in INSTRON 1255 equipment with an INSTRON 8800 computer system and the Bluehill2 program. Different pressures were used for both metallic powder mixtures and the green densities were calculated by assuming that the density of the base metal is 2.7 kg/dm^3 when aluminium is used, and 2.65 kg/dm^3 for the AlSi12 alloy. The samples were later sintered at a pre-determined temperature in the air. After various times of sintering, samples were taken out of the retort furnace and quenched into water to solidify the foam structures.

The sintered samples were characterized with a light microscope (LM, Nikon microphot – FXA) and analyzed

Table 1: Characteristics of the used powders
Preglednica 1: Lastnosti uporabljenih prahov

Powders	Manufacturer	Mean particle size d/μm	Purity w/%	Method of manufacturing
Al	Non ferrum, Kranj	106	99.7	Air atomization
AlSi12	Non ferrum, Kranj	47	composition w(Si) = 11.29 %	Air atomization
TiH_2	Sigma-Aldrich	14	98	Ball milling

with the AnalySIS PRO 3.1 program. The size and the distribution of the pores were determined by a standard metallographic method for determining the size and the distribution of the grains in the microstructures [15]. Metallographic samples of the precursors and the foam samples were prepared using a standard metallographic procedure, examined with scanning electron microscope (FE-SEM JEOL JSM-6500F) and analyzed by energy-dispersive electron spectroscopy (EDS, INCA X-SGHT LN2 detector, INCA ENERGY 450 analyzing program) for the elemental analyses. SEM images of the powders were also made.

3 RESULTS AND DISCUSSION

Metallic powders produced in a gas atomizer, in our case in air, have an oblong, quasi-spherical shape with varying size distributions. **Figure 1** shows SEM images of the used powders; (a) Al 99.7 %, (b) AlSi12 and (c) TiH_2. The size and he characteristics of the powders are shown in **Table 1**. The aluminium powder particles (**Figure 1** (**a**)) have a mean size of 106 μm, while the AlSi12 powder particles (**Figure 1** (**b**)) have a mean size of 47 μm, which is half the size of the Al powder particles. However, the morphology of the powders is typical for gas-atomized powders from a liquid metallic melt, and it can be described as a bulk prolonged, semi-spherical shape. On the other hand, the morphology of the TiH_2 powder particles is quite different from that of the metallic powders (**Figure 1** (**c**)). The TiH_2 powder was prepared by the ball milling of titanium in a hydrogen atmosphere under pressure [16–18] and it exhibits an irregular, sharp, polygonal morphology. The mean particle size was 14 μm, significantly smaller than that of the matrix-material powder particles [19].

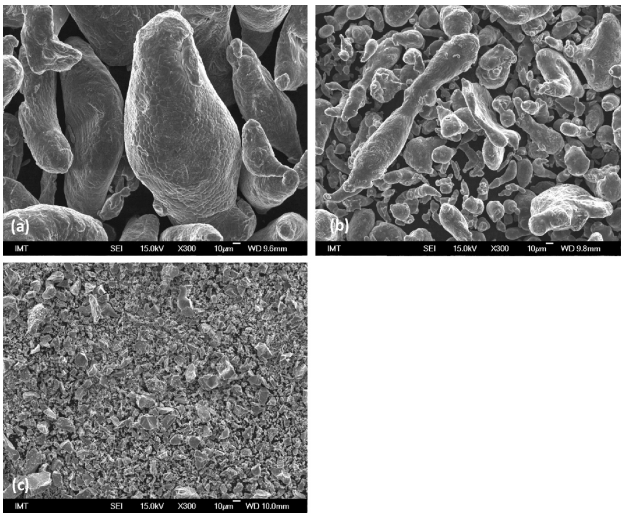

Figure 1: SEM images of as-received powders at the same magnification; (a) Al powder of 99.7 % purity, (b) powder of the AlSi12 alloy, and (c) TiH_2 powder

Slika 1: SEM-slike prahov, narejene pri enaki povečavi; (a) Al prah s čistoto 99,7 %, (b) prah zlitine AlSi12 in (c) prah TiH_2

Table 2: Influence of compacting pressures on the green densities of precursors

Preglednica 2: Vpliv pritiska stiskanja na zeleno gostoto prekurzorjev

	Green density of precursor	
Compacting pressure *p*/MPa	*w*(Al + 1 % TiH_2)/%	*w*(AlSi12 + 1 % TiH_2)/%
200	94.8	75.6
300	97.9	82.4
400	98.1	86.1
500	98.5	89.9
700	98.8	93.2
750	/	94.8
800	/	95.8
900	/	96.2

The surface of all the powder particles was oxidized. The thickness of the oxide layer depended on the affinity of the basic material for oxygen, which was very high for both the aluminium and TiH_2 [20–24]. This oxide layer was examined in our previous work [21,23] and found to be one of the influential parameters for the formation of metallic foams by the powder-metallurgy process. The oxide layer on TiH_2 powders caused a delayed gas evolution, while the oxide layer on the aluminium powder particles increased the viscosity of the melt, which had a favourable influence on the foaming process [11,25].

The free flowability of the Al powder particles was 75 s per 50 g of powder, while the AlSi12 and TiH_2 particles did not flow freely, since they did not have good flowing properties. The bulk density (cumulative volume fraction as a function of the particle size of powder/Al) of the Al powder was 1.23 kg/dm^3, and 1.20 kg/dm^3 for the AlSi12 powder. The TiH_2 powder had a bulk density of 1.34 kg/dm^3. Both powders, the Al and of the AlSi12, had a tapped density of 1.43 kg/dm^3, while the TiH_2 powder had a tapped density of 1.61 kg/dm^3. There was no major difference in the densities of both metallic powders, but there was a difference in the flow properties of the two. Though produced in the same way, with similar tapped densities, the two metallic powders had different final green densities after the compacting process. The characteristics of the TiH_2 powder did not influence

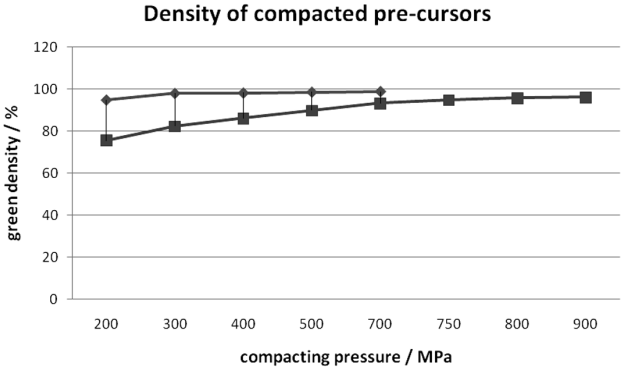

Figure 2: Green density of the compacted precursors

Slika 2: Zelene gostote stisnjenih prekurzorjev

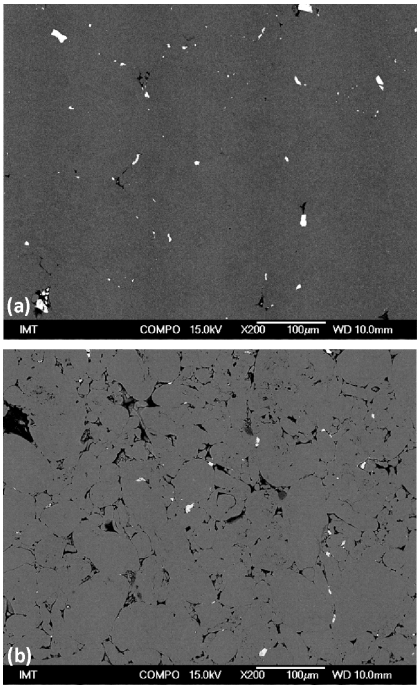

Figure 3: Precursors; double-axially compacted with pressure of 400 MPa, (a) Al precursor of 99.7 % pure Al, determined density was approximately 98.1 %, (b) AlSi12 precursor, determined density was approximately 86.1 %. BE image – bright spots are titanium particles and dark spots the porosity.

Slika 3: Prekurzorji, obojestransko stisnjeni s 400 MPa, (a) Al prekurzor iz Al prahu čistote 99,7 % z zeleno gostoto 98,1 %, (b) AlSi12 prekurzor z zeleno gostoto 86,1 %. BE slike – svetli predeli so titanovi delčki, temni predeli so poroznost.

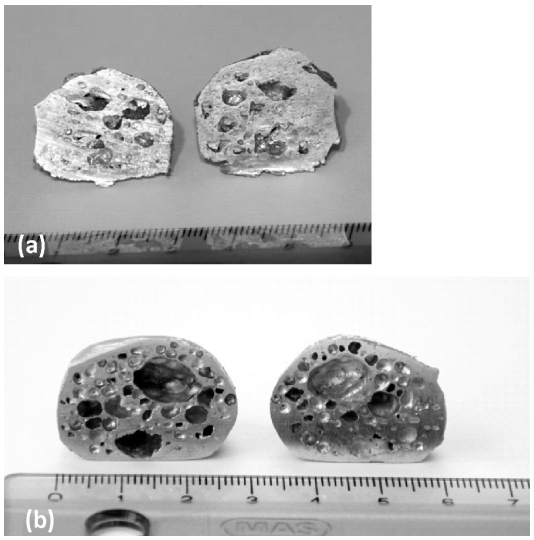

Figure 4: Cross-section of pure Al foams; (a) cold pressed with 200 MPa, sintered at 750 °C for 7 min, (b) cold pressed with 400 MPa, sintered at 750 °C for 6 min 30 s.

Slika 4: Prerez Al-pene iz tehnično čistega aluminija; (a) hladno obojestransko stisnjeno z 200 MPa, sintrano pri 750 °C, 7 min, (b) hladno obojestransko stisnjeno s 400 MPa, sintrano pri 750 °C, 6 min 30 s.

the properties of the precursors, since a relatively small amount of TiH_2 powder was used in the mixture, but its properties did have an influence on the distribution of the TiH_2 powder in the metallic powder matrix. In any case, it was preferable to have a homogenous distribution of TiH_2 particles in the precursor material.

After one hour of mixing the powder mixtures were compacted with various pressures. The influence of the compaction pressures on the green densities of the precursors is presented in **Table 2** and in **Figure 2**. The precursors were examined by SEM and analyzed by EDS. The aluminium precursor that was compacted by the double-axial process with a pressure of 400 MPa is shown in **Figure 3** (**a**). The porosity of the precursor was approximately 2 %. TiH_2, as the foaming agent, was homogenously distributed in the matrix material. On the other hand, the powder of the AlSi12 alloy was also double-axially compacted, with pressures in the range from 200 MPa to 900 MPa. With a pressure of 400 MPa the porosity of the precursors was approximately 14 %. When the compacting pressure was raised up to 900 MPa, the porosity was reduced to only 4 %. Different theoretical densities of the precursors depended on the different qualities of matrix powders, e.g., on the size and the shape of the particles, the bulk and the tapped density. Though the matrix powders had practically the same shape, but different sizes, the compressibility of the powders differed. Compressibility also depended on the bulk and tapped densities of the powders. Double-axial compacting of both, the Al and the AlSi12 powders, at room temperature did not enable us to achieve the same green density through using higher pressures than for the alumosilicates. The limitation of the used compacting pressures was also related to the lubricated tool-steel die that started to stick due to the too high forces in compacting aluminium, while the AlSi12 alloy powder was harder and had a higher compacting resistance. In other words, a larger green density could be achieved with materials that had a better plastic deformability. Though high compacting pressures were applied, the porosity, especially in the AlSi12 precursors, still remained relatively high.

The EDS analysis determined the distribution of Si and Ti in the matrix material. The Si in the AlSi12 matrix was distributed uniformly throughout the whole

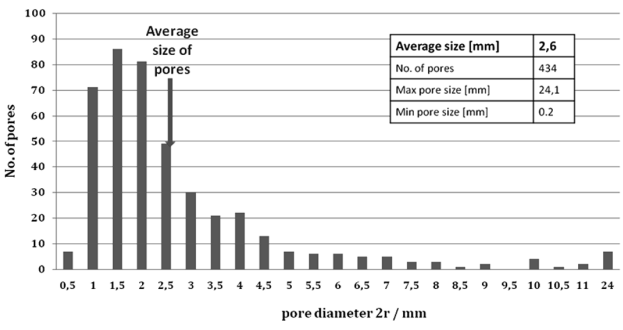

Figure 5: Histogram of pore-size distribution of pure Al foams

Slika 5: Histogram velikosti in porazdelitve por v Al-penah

matrix material, which proved that the AlSi12 powder was manufactured from the AlSi12 aluminium alloy and was not a mixture of Al and Si powder in the demanded ratio. The titanium was randomly but uniformly distributed as individual particles that could be seen in **Figure 3** (**b**) as bright phases in the BE image. On the other hand, only titanium particles were detected in the aluminium matrix, and they were similarly distributed as individual particles in the matrix material, as in the sample of the AlSi12 alloy (**Figure 3** (**a**)). The distribution of TiH_2, with the captured liberated gases around the particles of foaming agent, enabled a homogeneous distribution of pores in the aluminium foams.

The precursors were heat treated in a retort furnace at temperatures that were slightly higher than the melting temperature of the matrix material. All the samples were sintered at temperatures between 680 °C and 770 °C, for various sintering times. The temperatures of the retort in the furnace were controlled with CrNi thermocouple. After sintering at a pre-determined temperature and for a chosen time, the samples were taken out of the retort and quenched in air and/or water. The densities of the samples were then determined with the Archimedes' method.

The samples of pure aluminium that were compacted at lower pressures had fewer pores, and those were not spherical, while the samples that were pressed at 400 MPa or higher pressures contained more pores that were semi-spherical. Cross-sections of the obtained aluminium foams are shown in **Figure 4**.

Light microscopy was employed to determined the size and the distribution of the pores. A diagram of the pore-size distribution in our samples is presented in **Figure 5**. The same comparison was also made with samples of the AlSi12 alloy that were pressed with various forces and sintered at various temperatures and for various times. The cross-sections of the foams are shown in **Figure 6** and a diagram of the pore size distribution is shown in **Figure 7**.

The Al precursors were foamed at 750 °C from 6 min to 10 min. A histogram of the Al foampore size distribution (**Figure 5**) gave evidence that the majority of the pore sizes varied from 1 mm to 3 mm, giving an average

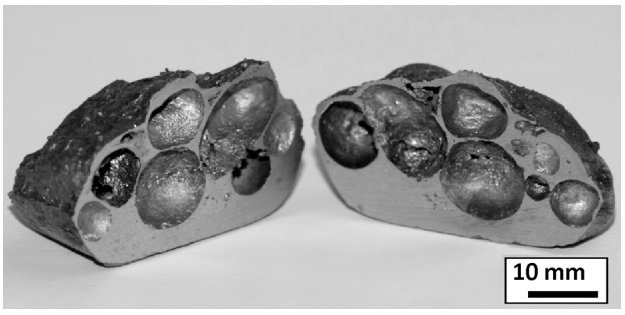

Figure 6: Cross-section of AlSi12 foam, cold pressed with 900 MPa, sintered at 770 °C for 9 min
Slika 6: Prerez pene zlitine AlSi12, hladno obojestransko stisnjeno z 900 MPa, sintrano pri 770 °C, 9 min

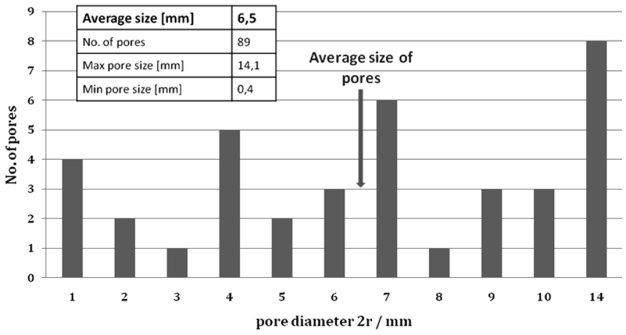

Figure 7: Histogram of pore-size distribution of the AlSi12 foam
Slika 7: Histogram velikosti in porazdelitve por v penah zlitine AlSi12

pore size of 2.6 mm. Only a smaller amount of pores larger than 5 mm was found. On the other hand, the AlSi12 foams were sintered at 770 °C and for times from 6 min to 13 min. A histogram of the pore-size distribution is presented in **Figure 7**. The distribution was very scattered and there was a larger amount of pores with sizes of more than 10 mm.

The difference between the size and the distribution of pores in both foamed materials was due to the green densities of the precursor materials. The compacted material with the higher green density was more easily and uniformly foamed. Therefore, the foaming effectiveness of the AlSi12 precursors was relatively low due to their low green densities (only up to 96 % in our case). The pores in this material were larger due to the prolonged foaming times that were needed to foam the material. This process causes further coarsening of the pores (the large pores were growing at the expense of the small ones).

The density of the foamed material, determined by the Archimedes' method, was from 0.58 kg/dm^3 to 1.2 kg/dm^3 for pure Al foams and from 0.9 kg/dm^3 to 1.6 kg/dm^3 for the AlSi12 foams. The reason for the difference in the densities was in foamability, which depends on the green density of the precursors.

Another difference in the foaming of both aluminium foams was caused by the Si. The AlSi12 alloy is a so-called casting alloy, and according to the Al-Si phase diagram, it is lying near the eutectic point, thus its melting-cooling properties are different from those of pure aluminium. The area between the liquidus and solidus lines is much larger for pure aluminium than for an alloy of the near-to-eutectic composition. Therefore, the temperature range between the liquidus and solidus state in which the pores can be formed is higher with pure aluminium.

4 CONCLUSIONS

It is very important for better foaming results to achieve a green density of at least 98 %. This can be easily achieved with pure aluminium powder. On the

other hand, it is practically impossible to achieve green densities higher than 96 % with AlSi12 powder using only a double-axial compression at pressures even up to 900 MPa at room temperature. For industrial applications it is also important to use as simple industrial machines as possible or to use techniques that are already used in the PM industry for the preparation of different types of complex products. Higher green densities can be achieved by increasing the compacting pressure and/or pre-heating the precursors to increase their compressibility [26,27].

The difference in size of our powder particles does no play such an important role in the difference in the green densities of both precursors, Al and AlSi12, though the bulk density is slightly higher with larger aluminium powder particles. The tapped density is approximately the same for both powders. The most important parameter for achieving higher green densities is the compressibility of powder particles, which depends on the properties of the metallic alloy.

A very important parameter in the foaming process is the foaming temperature. In our study, a temperature of 750 °C was chosen as the most suitable temperature for pure aluminium and 770 °C for the AlSi12 alloy. The results of our study and from the references confirm that the foaming temperature differs from the melting temperature of the matrix material and it cannot be correlated directly from the relation with the melting point of the material. However, while there is no direct correlation between the foaming and the melting temperature, so the foaming temperature should be determined for each matrix material separately, depending on the applied foaming agent. Also, the foaming time has to be chosen in a similar way. It should be determined separately for each alloy and for each foaming temperature.

The most efficient aluminium alloys used for foaming by the PM route are the alloys with higher contents of aluminium and technically pure Al powder. Therefore, so-called aluminium wrought alloys that have a lower content of impurities and of alloying elements (usually less than $w = 1$ %) are more often used for foaming than the casting alloys that have higher amounts of alloying elements. The reason for the selection of wrought alloys is also due to the fact that according to the Al-Si phase diagram the alloys closer to the aluminium corner of the diagram have a higher temperature interval between the liquidus and the solidus temperature in which pores can be formed. In any case, the viscosity of wrought alloys is higher than that of casting alloys, and therefore pores are formed due to the capture of liberated gases from the foaming agents.

Acknowledgements

This work has been supported by the "Physics and Chemistry of Porous aluminium for Al panels capable of highly efficiently energy absorption" project L2-2410 (D), funded by the Slovenian Research Agency. The views expressed in this publication reflect only the views of the authors and the SR Agency is not liable for any use that may be made of the information contained therein.

5 REFERENCES

[1] J. Banhart, Manufacture, characterisation and application of cellular metals and metal foams, Progress in Materials Science, 46 (**2001**), 559–632

[2] F. Simancik, J. Jerz, J. Kovacik, P. Minar, Aluminium foam – A new light-weight structural material, Kovove Materialy-Metallic Materials, 35 (**1997**), 265–277

[3] G. J. Davies, S. Zhen, Review Metallic foams: their production, properties and applications, Journal of Materials Science, 18 (**1983**), 1899–1911

[4] C. J. Yu, H. H. Eifert, J. Banhart, J. Baumeister, Metal foaming by a powder metallurgy method: production, properties and applications, Materials Research Innovations, 2 (**1998**), 181–188

[5] J. Banhart, H. W. Seeliger, Aluminium foam sandwich panels: Manufacture, Metallurgy and Applications, 10 (**2008**), 793–802

[6] M. Haesche, J. Weise, F. Garcia-Moreno, J. Banhart, Influence of particle additions on the foaming behaviour of AlSi11/TiH2 composites made by semi-solid processing, Materials Science and Engineering a-Structural Materials Properties Microstructure and Processing, 480 (**2008**), 283–288

[7] M. Guden, S. Yuksel, SiC-particulate aluminum composite foams produced from powder compacts: foaming and compression behavior, Journal of Materials Science, 41 (**2006**), 4075–4084

[8] S. Esmaeelzadeh, A. Simchi, Foamability and compressive properties of AlSi7-3 % SiC-0.5 % TiH2 powder compact, Materials Letters, 62 (**2008**), 1561–1564

[9] R. E. Raj, B. S. S. Daniel, Manufacturing challenges in obtaining tailor-made closed-cell structures in metallic foams, Springer London Ltd, (**2008**), 605–612

[10] R. Surace, L. A. C. De Filippis, A. D. Ludovico, G. Boghetich, Experimental analysis of the effect of control factors on aluminium foam produced by powder metallutgy, Proc. Estonian Acad. Sci. Eng., 13 (**2007**), 156–167

[11] Z.-L. Song, L.-Q. Ma, Z.-J. Wu, H. De-Ping, Effects of viscosity on cellular structure of foamed aluminum in foaming process, Journal of Materials Science, 35 (**2000**), 15–20

[12] C. Jimenez, F. Garcia-Moreno, M. Mukherjee, O. Goerke, J. Banhart, Improvement of aluminium foaming by powder consolidation under vacuum, Scripta Materialia, 61 (**2009**), 552–555

[13] M. p. i. federation, Standard test methodes for metal powders and powder metallurgy products, Metal Powder Industries Federation, Princeton, New Jersey 08540 USA, 1985–1986

[14] B. Šuštaršič, L. Kosec, T. Špan, M. Jelenko, M. Torkar, An instrumented cell to analyse the behaviour of metal powders during cold uniaxial die compaction, Mater. Tehnol., 35 (**2001**), 351

[15] M. Nosko, F. Simancik, R. Florek, Reproducibility of aluminum foam properties: Effect of precursor distribution on the structural anisotropy and the collapse stress and its dispersion, Materials Science and Engineering a-Structural Materials Properties Microstructure and Processing, 527 (**2010**), 5900–5908

[16] H. Zhang, E. H. Kisi, Formation of titanium hydride at room temperature by ball milling, Journal of Physics-Condensed Matter, 9 (**1997**), L185–L190

[17] R. S. Vennila, A. Durygin, M. Merlini, Z. Wang, S. K. Saxena, Phase stability of TiH2 under high pressure and temperatures, International Journal of Hydrogen Energy, 33 (**2008**), 6667–6671

[18] J. W. Zhao, H. Ding, X. F. Tian, W. J. Zhao, H. L. Hou, Thermodynamic Calculation on the Formation of Titanium Hydride, Chinese Journal of Chemical Physics, 21 (**2008**), 569–574

[19] A. Ibrahim, C. Korner, R.F. Singer, The effect of TiH2 particle size on the morphology of Al-foam produced by PM process, Advanced engineering materials, 10 (**2008**), 845–848

[20] I. Paulin, D. Mandrino, C. Donik, M. Jenko, AES and XPS characterization of titanium hydride powder, Mater. Tehnol., 44 (**2010**) 2, 73–76

[21] C. Donik, A. Kocijan, J. T. Grant, M. Jenko, A. Drenik, B. Pihlar, XPS study of duplex stainless steel oxidized by oxygen atoms, Corrosion Science, 51 (**2009**), 827–832

[22] C. Donik, A. Kocijan, D. Mandrino, I. Paulin, M. Jenko, B. Pihlar, Initial oxidation of duplex stainless steel, Applied Surface Science, 255 (**2009**), 7056–7061

[23] D. Mandrino, Č. Donik, M. Jenko, AES of thin oxide layers on a duplex stainless steel surface, Surface and Interface Analysis, 42 (**2010**), 762–765

[24] B. Matijasevic, J. Banhart, Improvement of aluminium foam technology by tailoring of blowing agent, Scripta Materialia, 54 (**2006**), 503–508

[25] S. Asavavisithchai, A. R. Kennedy, The effect of compaction method on the expansion and stability of aluminium foams, Advanced engineering materials, 8 (**2006**), 810–815

[26] M. Shiomi, S. Imagama, K. Osakada, R. Matsumoto, Fabrication of aluminium foams from powder by hot extrusion and foaming, Journal of Materials Processing Technology, 210 (**2010**), 1203–1208

[27] K. Mori, H. Nishikawa, Cold repeated forming of compact for aluminium foam, Journal of Materials Processing Technology, 210 (**2010**), 1580–1586

UDK 669.1:621.4:620.179
Original scientific article/Izvirni znanstveni članek

ISSN 1580-2949
MTAEC9, 45(1)21(2011)

A NEW METHOD FOR DETERMINING THE REMAINING LIFETIME OF COATED GAS-TURBINE BLADES

NOVA METODA ZA IZRAČUN PREOSTALE TRAJNOSTNE DOBE LOPATIC PLINSKIH TURBIN

Leonid Borisovich Getsov[1], P. G. Krukovski[2], N .V. Mozaiskaja[1], Aleksander I. Rybnikov[1], K. A. Tadlja[2]

[1]NPO ZKTI Russian, [2]ITTPh NAN Ukraina
guetsov@yahoo.com

Prejem rokopisa – received: 2010-02-01; sprejem za objavo – accepted for publication: 2011-01-03

In the course of the exploitation of gas-turbine units (GTE) their turbine blades accumulate defects. These defects result from both the static stress caused by the centrifugal forces and by the thermo-cyclic stress. Since gas turbines usually operate under variable conditions, the time of exploitation cannot be taken as a reliable parameter for a determination of the remaining lifetime. Unfortunately, in many cases, at the moment when a GTE is stopped for maintenance, the thermal conditions of the previous exploitation of the blades are unknown.
In this presentation a new method of determining the remaining lifetime for coated blades is considered. A long-term strength-decay evaluation is carried out on the basis of the equivalent exploitation temperature T_{eq}, the known exploitation time τ and the static stresses σ.

Key words: Larson-Miller dependence, turbine blade, remaining lifetime, coating, diffusion, equivalent temperature

Med uporabo plinskih turbin (GTE) se v lopaticah kopičijo napake. Te so posledica statičnih napetosti zaradi centrifugalnih in termo-cikličnih napetosti. Ker plinske turbine obratujejo v spremenljivih razmerah, časa eksploatacije ni mogoče upoštevati kot zanesljivega parametra za določitev preostale trajnostne dobe. Na nesrečo v mnogih primerih, ko je GTE ustavljena zaradi vzdrževanja, niso poznane termične razmere prejšnje uporabe lopatice.
V tem sestavku predstavljamo novo metodo za določanje preostale trajnostne dobe za lopatice s prekritjem. Ocena dolgotrajnega zmanjšanja trdnosti je izvršena na podlagi ekvivalentne temperature uporabe T_{eq}, znanega časa uporabe τ in statičnih napetosti σ.

Ključne besede: Larson-Miller odvisnost, turbinska lopatica, preostala trajnostna doba, pokritje, difuzija, ekvivalentna temperatura

1 MAIN THESES

Four different cases can be considered:

1. Uncooled blades, working in constant conditions (at a constant temperature). Blades of this type (type 1) in a stationary mode of operation have a constant temperature and constant stress in each cross section;
2. Cooled blades in a stationary mode of operation (at a constant gas temperature). In this case blades have a specific distribution of stresses and temperatures in each cross-section. For the calculation of the remaining lifetime of these blades (type 2) the thermostatic stress is usually omitted and only the static centrifugal stress is used;
3. Uncooled blades in a variable mode of operation (type 3) – for each mode of operation in each cross-section they have a constant temperature and stress;
4. Cooled blades working under variable conditions (type 4).

In recent works [1–6] the surface-layer processes in the blades were investigated as a function of the long exposures to high temperature. By means of solving the direct and inverse diffusion problem, the authors have developed some models and methods of prediction for these processes. On the basis of these results the temperature distribution in the surface layer for the weak cross-section can be found using an X-ray analysis and a quantitative metallographic analysis of the blade, taken out from the engine. These calculations are based on the temperature dependences of the coating elements' diffusion characteristics. In this way, for example, an evaluation of the average operating temperatures of the coating, type NiCoCrAlY with the initial concentration of the $c(\mathrm{Al}) = 8.4$ %, was performed [6] – **Figure 1** (cooled blades, IN738 alloy; worked for 26 400 h in the turbine).

2 DETERMINATION OF T_{eq}^{σ}

Due to the differences in the temperature dependence for the diffusion coefficients and long-term strength, the temperature T_{eq}^{D} (obtained from the surface-layer elements redistribution) can be used for the remaining lifetime determination only in the case of Type-1 blades. In all the other cases a comparison of T_{eq}^{σ} and T_{eq}^{D} is required (see **Figure 2**).

The method, described below, is based on the following assumptions:

1. The remaining lifetime of the blade is determined by the remaining lifetime of its bulk metal;
2. The temperature of the blade cross-section is supposed to be constant and it corresponds to the maximum

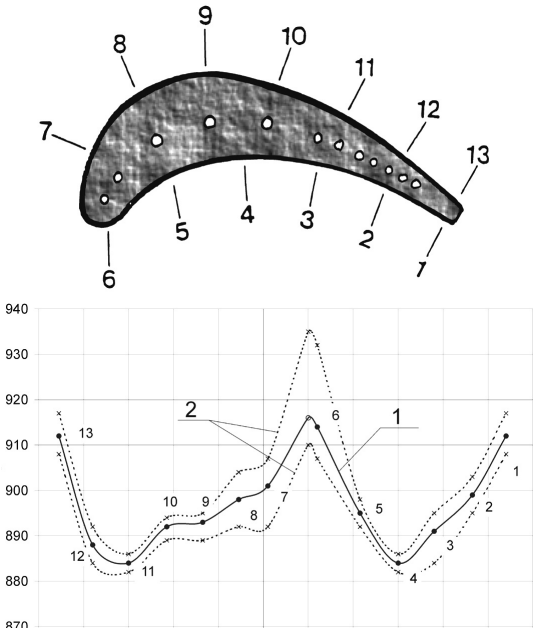

Figure 1: Working temperature (°C) distribution around the cross-section contour after exploitation for 26 400 h. The numbered points on the plot correspond to the numbered positions on the blade. Curve 1 – calculated; curves 2 – error range of measurements.

Slika 1: Porazdelitev delovne temperature (°C) vzdolž oboda preseka po 26 400 h eksploatacije. Oštevilčene točke označujejo oštevilčene točke na lopatici. Krivulja 1 – izračunano, 2 – območje merilne napake.

temperature value in the maximally loaded cross-section;

3. The damages for different temperatures and different stresses are summed according to a linear law and at the moment of destruction the following relationship is true:

$$\Sigma(\tau_i / t_i) = 1 \qquad (1)$$

where τ_i is the exploitation time at the temperature T_i and under the stress σ_i; t_i is the time of destruction under the same conditions. It is necessary to mention that for a traditional estimation, it is more appropriate to use "0.87" instead of "1" in the right-hand part of Eq.1.

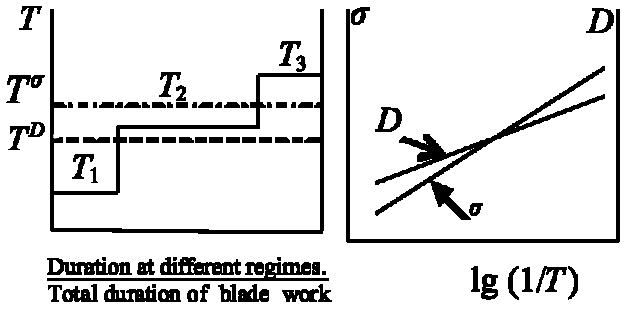

Figure 2: The diagram of the change of temperature during operation (a) and the temperature dependences of long durability and the factors of diffusion (b)

Slika 2: Diagram spremembe temperature med operacijo (a) in temperaturna odvisnost dolge trajnosti in difuzijski faktorji (b)

Let us suppose that we have the following distribution of work-times for a gas-turbine unit: $\tau_1 : \tau_2 : \tau_3 : \tau_4 : \tau_5$ etc. under different conditions with the corresponding power N_1, N_2, N_3, N_4, N_5 etc. and according to the blades temperatures T_1, T_2, T_3, T_4, T_5 etc. In this case the time of exploitation can be found as $\tau = \boldsymbol{a}\Sigma\tau_i$.

Let us use the Larson-Miller dependence:

$$P(\sigma) = T(C + \lg t) \qquad (2)$$

where t is the time of destruction at the temperature T and stress σ. The value of the parameter C (in the first approximation $C = 20$) can be specified for the involved temperature interval from the experimental long-term strength of the blade material.

Using (2):

$$t_1 = 10\ [P(\sigma_1)/T_1] - C\ ;\ t_2 = 10\ [P(\sigma_2)/T_2] - C\ ;$$
$$t_3 = 10\ [P(\sigma_3)/T_3] - C\ ;\ t_4 = 10\ [P(\sigma_4)/T_4] - C\ ;$$
$$t_5 = 10\ [P(\sigma_5)/T_5] - C\ \ldots \qquad (3)$$

where σ_i is determined by the rotation frequency in the regime N_i, $P(\sigma_i)$ and C can be obtained from the reference data for the corresponding material.

Taking into account that the damage summation is linear (1) and the relationship (3), we can determine the value $\boldsymbol{a}$. It corresponds to the given time distribution for the different operation regimes $\tau_1 : \tau_2 : \tau_3 : \tau_4 : \tau_5$ etc.

The value of the equivalent temperature T_{eq} can be obtained from the dependences:

$$T_{eq}^{\sigma} = \frac{2{,}3P(\sigma_{eq})}{\ln\left(\sum \tau_i / \sum \tau_i \exp\left(-2{,}3P(\sigma_{eq})/T_i\right)\right)}$$

$$P(\sigma_{eq}) = T_{eq}^{\sigma}\,(C + \lg \tau_{p\,eq})$$

$$\sum \frac{\tau_i T_i}{P(\sigma_i) - CT_i} = 1 \qquad (4)$$

which parameters are values of the operating time $\tau_1 : \tau_2 : \tau_3 : \tau_4 : \tau_5$ etc. by the various power settings characterized by the values T_i and σ_i. Here, $P_{(\sigma eq)}$ – parameter of dependence of Larson-Miller. Thus, the remaining lifetime of the blades 2–4 after the turbine operation during the time τ can be determined for the stress σ_{eq} multiplied by the long-term strength coefficient (obtained from the initial turbine project or taken from the strength standards) as the destruction time at the temperature $\boldsymbol{T}_{eq}^{\sigma}$ minus the turbine operating time.

If we suppose that the exploitation temperatures changed according to the requirements' specification (or according to the recorded exploitation parameters), then it is possible, as it is described above, to determine the remaining lifetime. Thus, the calculated $\boldsymbol{T}_{eq}^{\sigma}$ is based on the time ratio $\tau_1 : \tau_2 : \tau_3 : \tau_4 : \tau_5$ etc., but in most cases this ratio is unknown. For a determination of the real (objective) ratio $\tau_1 : \tau_2 : \tau_3 : \tau_4 : \tau_5$ etc. the calculated $\boldsymbol{T}_{eq}^{D}$ can be used.

3 METHOD OF DETERMINING THE WORKING-TIME RATIO FOR DIFFERENT REGIMES

By solving the inverse diffusion problem for the experimental Al distribution in the surface layer, the value of the diffusion coefficient can be determined (for the real temperature-change law during the turbine exploitation). Then, if the diffusion temperature dependence is known for the selected element, the value of T_{eq}^{D} can be determined. This temperature (T_{eq}^{D}) will be equivalent to the average temperature determined using the Al diffusion parameters. It can be used as an equivalent temperature for the determination of the residual corrosion lifetime of the coating. But for the determination of the blade's remaining lifetime under applied stress (centrifugal bending stress, or especially thermo-cyclic stress), this temperature (T_{eq}^{D}) must be corrected according to the aforesaid statements.

Let us suppose that the element distribution in the diffusion layer does not depend on the consecution of the temperature-time conditions of the process. Then, by solving the direct diffusion problem, step by step (for different initial conditions), at different temperatures T_i and times of exploitation τ_i, the distributions of the Al and oxide layer thickness can be obtained (corresponding to the exploitation times). By comparing this data with the calculated T_{eq}^{D} for the different points of the profile (**Figure 1**), the ratio of times $\tau_1 : \tau_2 : \tau_3 : \tau_4 : \tau_5$ etc. can be obtained.

4 METHOD OF T_{eq}^{D} DETERMINATION

Let us consider the processes in the solid coating **MeCrAlY** (**Figure 3**).

The oxide **Al_2O_3** is formed during the blade exploitation by a combination of **Al** and oxygen absorbed from the gas environment and diffused trough the oxide layer ($x_1 - x_0$) to the oxide-coating interface marked as x_1. The diffusion of **Al** from the coating occurs in two directions:

- to the oxide-coating interface x_1, where it reacts with diffused oxygen;
- to the coating-bulk alloy interface x_4, where it is accumulated in the inter-diffusion zone and then, depending on the Al concentration in the bulk metal, diffuses either into the bulk alloy orin to the coating.

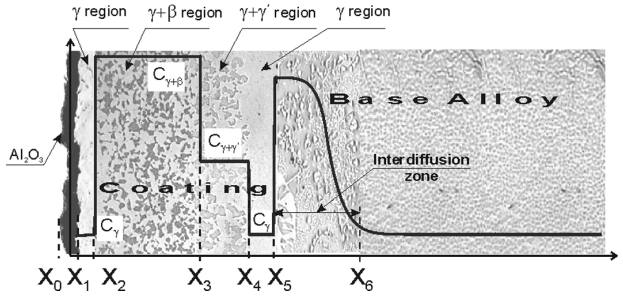

Figure 3: Typical Al concentration distribution in the coating layer and the bulk alloy

Slika 3: Tipična porazdelitev koncentracije Al v plasti pokritja in v zlitini

Due to the Al diffusion from the $\gamma + \beta$ two-phase coating region, the depleted **Al** single-phase zones with a reduced concentration of Al (γ-phase) are formed on both sides of the coating – on the side of the oxide and on the side of the bulk alloy (depleted zones I and II, **Figure 2**). All **Al**, diffused from the coating, is diffused from the $\gamma + \beta$ two-phase coating region due to the disappearance (consumption) of the β-phase. The **Al** concentration curve in the MCrAlY coating has the shape of a stepped line, and in the bulk alloy region – a curve with the maximum in the inter-diffusion zone.

The process of the Al mass-exchange within the calculation region $x_1 < x < x_\infty$ can be described with the following diffusion equation:

$$\frac{\partial C}{\partial \tau} = \frac{\partial}{\partial x}\left[D_{\text{eff}} \frac{\partial C}{\partial x} \right] + W \tag{5}$$

$$\tau > 0 \quad x_1 < x < x_\infty \quad C = C(x,\tau)$$

$$W = W(x,\tau) \quad D_{\text{eff}} = D_{\text{eff}}(x)$$

$$x_1 = x_1(\tau) \quad x_2 = x_2(\tau) \quad x_3 = x_3(\tau) \quad x_5 = x_5(\tau)$$

with the initial condition:

$$C(x,0) = C(x) = \begin{cases} C_n^0 & 0 < x < x_4 \\ C_{oc}^0 & x \geq x_4 \end{cases} \tag{6}$$

the boundary condition for infinity:

$$\frac{\partial C(x_\infty, \tau)}{\partial x} = 0 \tag{7}$$

and the boundary condition on the moving interface x_1, describing the diffusion flux (due to the concentration gradient) of the **Al** from the coating to the left (Figure 3), forming the oxide:

$$J_{\text{OK}}(x_{1+}, \tau) = -D_{\text{eff}} \frac{\partial C(x_1, \tau)}{\partial x} \tag{8}$$

The flux (8) conjointly with the flux $C(x_1, \tau)(dx_1/d\tau)$ (formed by moving the interface x_1 to the right) produce the total **Al** flux, which creates an oxide film with a thickness of Δx. The kinetics of the oxide film growth can be described with two parabolic equations:

$$\Delta x(\tau) = x_1(\tau) - x_0(\tau) =$$

$$= \begin{cases} k_{\text{OK}}^{*} \cdot \tau^{0.5} & 0 < \tau < \tau^{*} \\ k_{\text{OK}}^{**} \cdot \sqrt{\tau - \tau^{0}} & \tau^{*} < \tau < \infty \end{cases} \tag{9,10}$$

where k_{ox}^{*}, k_{ox}^{**} – are the coefficients of the oxide-film-growth intensity (the so-called constants of oxidation), τ^{*} – boundary time point, before it the kinetics obey the oxidation law (9), after – the oxidation law (10). The curves (9) and (10) for intersect at the time point τ^{*} ; τ^{0} – time point (negative value) of the intersection for the curve (10) and the time axis τ. The

necessity of using two parabolic laws (9) and (10) for the description of the Al-oxide growth can be explained by the faster formation (growth) of the θ-oxide phase before the time point τ^*, and by the slower growth of the Al_2O_3 α-oxide phase for $\tau > \tau^*$. The coefficients $k_{OK}{}^*$, $k_{OK}{}^{**}$, τ^0 and the value τ^* in (9) and (10) are determined from the experimental data of the oxide growth as a function of time.

The following concentration conditions are taken for the moving boundaries x_2 and x_3:

$$C(x_{2-},\tau)=C(x_{3+},\tau)=C_{y}$$
$$C(x_{2+},\tau)=C(x_{3-},\tau)=C_{y+\beta} \qquad (11)$$

Thus, by analogy with the boundary condition (8) for the fixed boundary x_4, the diffusion flux of the Al from the coating to the left (which forms the diffusion zone $\Delta y = x_5 - x_4$) and the diffusion of Al to the bulk alloy can be written as:

$$J_{oc}(x_{4-},\tau)=-D_{\text{eff}}\frac{\partial C(x_{4-},\tau)}{\partial x} \qquad (12)$$

According to the physical model (**Figure 3**), the flux of the Al (12) from the coating induces a new phase formation in the diffusion zone having the thickness $\Delta y = x_5 - x_4$, i.e.:

$$J_{oc}(x_{4-},\tau)=W(x,\tau)\cdot\Delta y(\tau) \qquad (13)$$

where W is the Al mass, which diffused from the coating to the diffusion zone $x_4 < x < x_5$ depending on $C_{\gamma+\beta} - C_\gamma$ and determined by the relationship

$$\Delta y(\tau)=x_5(\tau)-x_4=k_{\text{D}}\cdot\sqrt{\tau-\tau_{\text{D}}^0} \qquad (14)$$

The coefficient k_D and the value $\tau_D{}^0$ in (14) are determined from the experimental data of the diffusion-zone increase with time. $\Delta y = x_5 - x_4$ – the diffusion-zone width, which increases with time due to boundary x_5 shift to the right according to the parabolic law:

$$W=W(x,\tau)=$$
$$=\begin{cases}k_{\text{w}}\cdot(C_{\gamma+\beta}-C_{\gamma})^{\text{m}} & x_4<x<x_5\\ 0 & x_1<x<x_4,\ x>x_5\end{cases} \qquad (15)$$

where k_w is the coefficient of the Al precipitation in the diffusion zone.

Since in the system the coating/oxide film/bulk alloy mass balance should be fulfilled, according to (8) and (12) the total flux of Al from the two-phase coating will take the form:

$$J_{\Sigma}(\tau)=J_{OK}(x_{1+},\tau)+J_{oc}(x_{4-},\tau) \qquad (16)$$

According to the physical model, all the Al outgoing from the coating, actually outgoes from the $\gamma + \beta$-two-phase coating zone by consuming the β-phase. Then the movement of the boundaries x_2 and x_3, and the Al concentration decrease in the $\gamma + \beta$-two-phase zone can be described by the equation of the mass balance between the Al diffusion fluxes through these boundaries and for the diffusion fluxes due to the Al concentration differences in the $\gamma + \beta$- and γ-phases ($\Delta C = C_{\gamma+\beta} - C_\gamma$):

$$J_{\Sigma}=J_{\gamma}(x_{2-},\tau)+J_{\gamma}(x_{3+},\tau)=$$
$$=\Delta C\cdot\frac{\text{d}x_2}{\text{d}\tau}+\Delta C\cdot\frac{\text{d}x_3}{\text{d}\tau}+(x_3-x_2)\frac{\text{d}C_{\gamma+\beta}}{\text{d}\tau} \qquad (17)$$

where $J_{\gamma}(x_{2-},\tau)=-D_{\text{eff}}\dfrac{\text{d}C(x_{2-},\tau)}{\text{d}x}$

and $J_{\gamma}(x_{3+},\tau)=-D_{\text{eff}}\dfrac{\text{d}C(x_{3+},\tau)}{\text{d}x}$

are the diffusion fluxes towards the oxide and bulk alloy due to the Al concentration gradients to the left and to the right of the boundaries x_2 and x_3, respectively.

The expression (17) after dividing by J_Σ takes the form:

$$1=\Delta C\cdot\frac{\text{d}x_2}{\text{d}\tau}/J_{\Sigma}+\Delta C\cdot\frac{\text{d}x_3}{\text{d}\tau}/J_{\Sigma}+$$
$$+(x_3-x_2)\frac{\text{d}C_{\gamma+\beta}}{\text{d}\tau}J_{\Sigma}=g_2+g_3+g_{2,3} \qquad (18)$$

where g_2 and g_3 are the portions of the total Al mass, which left the coating due to the boundaries x_2 and x_3 shifting correspondingly; $g_{2,3} = (1 - g_2 - g_3)$ – the portion of the total Al mass, which left the coating due to the decrease of the Al β-phase concentration in the region $x_2 < x < x_3$. The values g_2 and g_3 directly affect the speed of the shifting of the borders x_2 and x_3 and are taken as functions of the concentration differences $\Delta C = C_{\gamma+\beta} - C_\gamma$:

$$g_2=k_2\cdot\frac{\Delta C}{C_n^0}\qquad g_3=k_3\cdot\frac{\Delta C}{C_n^0} \qquad (19)$$

From the equations (15) and (16) it is possible to obtain the laws of the borders x_2 and x_3 shifting and the law of the decrease of concentration of Al $C_{\gamma+\beta}$ in the two-phase zone:

$$\frac{\text{d}x_2}{\text{d}\tau}=J_{\Sigma}\frac{k_2}{C_n^0}\qquad\frac{\text{d}x_3}{\text{d}\tau}=J_{\Sigma}\frac{k_3}{C_n^0}$$
$$\frac{\text{d}C_{\gamma+\beta}}{\text{d}\tau}=J_{\Sigma}(x_3-x_2)(1-g_2-g_3) \qquad (20)$$

the constants k_2 and k_3 in (19) can be obtained from the equation (20) using the experimental data of the borders x_2 and x_3 shifting dynamics and of the $C_{\gamma+\beta}$ plateau value in the region $x_2 < x < x_3$ for different times of the tests or exploitation.

The total concentration of Al $C_{\gamma+\beta}$ depends on the β-phase concentration $C_\beta(\tau)$ in the coating as:

$$C_{\gamma+\beta}(\tau)=C_{\beta}(\tau)\cdot C_{\beta}^{Al}+\left[1-C_{\beta}(\tau)\right]C_{y} \qquad (21)$$

where C_β^{Al} – concentration of Al in the β-phase.

The diffusion coefficient D_{eff}, the coefficient k_w and the power m in the mathematical model (5)–(21) can be obtained from the experimental data by means of the inverse-problem solution.

The diffusion coefficient D_{eff} in (5) is correct for the whole solution region, excluding the sub-region $x_2 < x < x_3$, where it was taken as a greater value due to the absence of the Al-concentration space gradient.

Al accumulated in the diffusion zone partially diffuses back into the coating, due to the absence of the Al-concentration space gradient.

The Al accumulated in the diffusion zone partially diffuses back into the coating, due to the gradient in the concentration to the right of the border x_4. The related diffusion flux:

$$J_{\text{md}}(x_{4+}, \tau) = -D_{\text{eff}} \frac{\partial C(x_{4+}, \tau)}{\partial x}$$

returns back into the intra-diffusion zone and is added to the main flux (13).

The program complex COLTAN created in the ITTPh NAN Ukraina allows us to calculate the Al concentration distribution in the coating and in the base blade material, $T_{\text{eq}}{}^{D}$ and time ratios $\tau_1 : \tau_2 : \tau_3 : \tau_4 : \tau_5$ etc. in the cooled blades for different operation modes. In the case of the uncooled blades (type 3) in order to obtain the time ratios the inverse problem must be solved for the blades taken from the GTE for different times of operation $\tau_1 : \tau_2 : \tau_3 : \tau_4 : \tau_5$ etc.

5 ALGORITHM FOR THE CALCULATION OF THE RESIDUAL LIFE TIME

On the basis of the aforesaid the following several steps are used for the determination of the residual lifetime of the coated blade removed from the turbine that has been running for the operation time τ:

1) determination of the parameters of diffusion for the blade coating by means of experiments and calculations,

2) experimental determination of the distribution of aluminium in different points of the surface layer of the coated blade taken out from the turbine,

3) calculation of the equivalent temperature $T_{\text{eq}}{}^{D}$ according to a special method based on the solution of the reverse diffusion problem for experimental data on the distribution of aluminium (see step 2),

4) calculation of the allocation of the time of GTE operation in different modes $\tau_1 : \tau_2 : \tau_3 : \tau_4 : \tau_5$ etc. $= r_1 : r_2 : r_3 : r_4 : r_5$ etc. , corresponding to the power values N_1, N_2, N_3, N_4, N_5 etc. (operation time $\tau = \boldsymbol{a} \Sigma r_i$, a $\tau_I = a r_i$. according to the data obtained during the step 2,

5) calculation of the equivalent temperature $T_{eq}{}^{\sigma}$ using equation (4)

6) calculation of residual lifetime of the set of blades (after the operation during the time τ).

The algorithm of the solution of the problem mentioned in step 4 consists of a number of successive calculations of the direct diffusion problem (with different initial conditions) for different temperatures T_i (within the real range for the examined GTE) and operation times τ_i (in different modes) as a result of which we obtain the relevant distributions of aluminium and the width of the oxide layer, corresponding to the operation times. Having these set of points for different conditions we chose those in which:

- the calculated Al distribution coincides with its experimental distribution,
- the equivalent temperature coincides with $\boldsymbol{T_{eq}{}^{D}}$.

The accord between these data and those obtained with the help of the calculations for the definition $T_{\text{eq}}{}^{D}$ in different points of the blade profile allows us to calculate the ratio of times $\tau_1 : \tau_2 : \tau_3 : \tau_4 : \tau_5$ etc. (see **Figure 1**, included as an example of the solution of the problem of finding $T_{\text{eq}}{}^{\text{D}}$ distributions) allows us to calculate the ratio of times $\tau_1 : \tau_2 : \tau_3 : \tau_4 : \tau_5$ etc.

In other words:

1. Knowing $T_{\text{eq}}{}^{D}$ and the total operation time of the examined blade, we are able to write the following equation representing the sum of solutions of reverse problems for different operating modes contributing to the resulting distribution curve

$$F_1(\tau, T_{\text{eq}}{}^{D}) = \Sigma F_1(\tau_i, T_i^{D}) \qquad (22)$$

2. Knowing $T_{\text{eq}}{}^{D}$, we obtain a number of possible values $\tau_I - T_i^{D}$ from the equation (22).

3. Knowing different values $T_{\text{eqj}}{}^{D}$ for different blade points we find the true values $\tau_i - T_i^{D}$ from the equation (22).

4. Having found the true values $\tau_i - T_i^{D}$ (step 3), we determine the value $T_{\text{eq}}{}^{\sigma}$ using the formula (4).

The residual lifetime of the set of blades (after the operating time τ) is calculated as the time value before fracture at the temperature $T_{\text{eq}}{}^{\sigma}$ under the stress σ_{eq}, multiplied by the strength safety factor (obtained in the course of the strength calculations for blades at the design stage or by the safety factor chosen from the strength standards) minus the elapsed operating time τ.

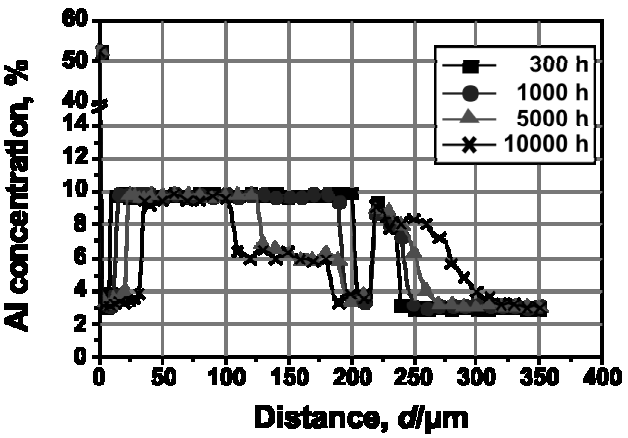

Figure 4: Al concentration distribution across the coating layer [NiCoCrAlYRe (Sicoat 2464) coating after exposition at 950 °C]

Slika 4: Porazdelitev koncentracije Al na prerezu plasti pokritja [NiCoCrAlYRe (Sicoat 2464) pokritje po žarjenju pri 950 °C]

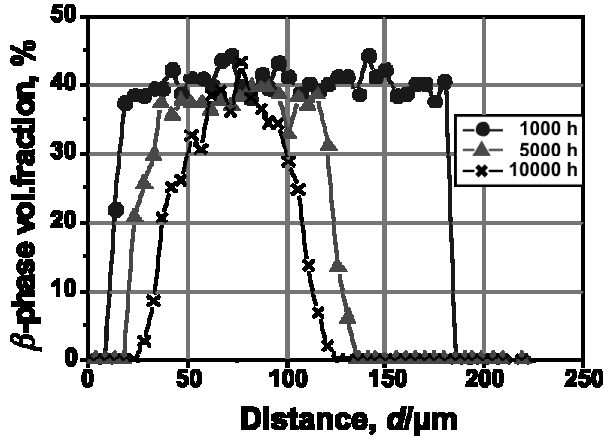

Figure 5: β-phase volume fraction distribution across the coating layer (different duration of exposure at 950 °C)
Slika 5: Porazdelitev volumskega deleža β-faze (različno trajanje žarjenja pri 950 °C)

As a basis for the above-mentioned calculations for MeCrAlY coatings the experimental data obtained in the present work can be used, namely:

- determination of the Al concentration distribution on the basis of the coating-layer thickness using the X-ray microanalysis method;
- determination of the volumetric share of the β-phase on the basis of the coating-layer thickness using digital optical metallography (for example, with the help of software made by "IstaVideoTest");
- measurement of the oxide film thickness on the coating surface and the thicknesses of inner and outer de-alloyed layers.

These experimental data must be obtained for not less than three temperatures from the real GTE temperature range and for several exposures that must produce meaningful results for the sought parameters.

6 X-RAY AND METALLOGRAPHIC ANALYSIS METHOD

The experimental data required for the above calculations for the MeCoCrAlY coatings include:

- a determination of the Al concentration distribution across the coating layer using the X-ray microanalysis method;
- a determination of the β-phase volume-fraction change across the coating layer using Digital Optical Metallography (for example with the software made by "IstaVideoTest");
- measurements of the oxide film thickness on the surface of the coating, and the inner and outer de-alloyed layers thicknesses (**Figure 3**).

This experimental data should be obtained for at least three different temperatures in the range of the real gas-turbine operating conditions with several time exposures that should bring meaningful results.

For the coatings of a different type, an element sensible to the working-temperature history should be taken as a diffusing element.

Some illustrative examples of the NiCoCrAlReY coating study on the alloy Rene80 can be seen in Figure 4–5.

The samples were isothermally exposed for times up to 20 000 h at the temperatures 900–980 °C. From **Figure 4** it can be seen that on the surface (up to 40 μm depth) and at the interface coating-alloy (at 180–220 μm) the formation of a de-alloyed layer is observed.

7 CONCLUSION

A new method of determining the remaining lifetime of coated blades was developed for stationary conditions. This method requires one blade's removal from the turbine after a long operating time, metallographic analysis and calculations using the data obtained from the laboratory experiments performed in advance.

The method is based on the Larson-Miller dependence, the law of linear summation of damages, and the assumption that the elements-distribution in the diffusion layer of the coating does not depend on the sequence of the temperature-time conditions.

8 REFERENCES

[1] Getsov L. B., Rybnikov A. I., Krukovski P. G., Kartavova E. S. De-alloying and fatigue of high temperature alloys used for gas turbine blades. *Materials at high temperature*, 13 (**1995**) 2, 81–86

[2] Getsov L. B., Rybnikov A. I., Krukovski P. G. Oxidizing modification of surface composition of high-temperature alloys. *Protection of Metals*. 4 (**1995**), 376–381

[3] P. Krukovsky, V. Kolarik, K. Tadlya, A. Rybnikov, I. Kryukov, M. Juez-Lorenzo, Theoretical and experimental approach for long term modelling of oxidation and diffusion processes in MCrAlY coatings. *European Federation of Corrosion Publications,* Number 34, Proceedings of an EFC Workshop 2001, Edited by M. Schutze, W. J. Quadakkers and J. R. Nicholls, ISSN P.1354-5116

[4] Krukovsky P. G, Kartavova E. S., Getsov L. B. Prediction model of high temperature diffusion and gas corrosion of gas turbine blade. *Thin Solid Films* 270 (**1995**), 679–688

[5] Getsov L. B. Rybnikov A. I. Krukovskiy P. G. et al. A procedure for determination the change of material fatigue resistance characteristics in long-term operation. *Materials at high temperatures.* 14 (**1997**) 1, 15–18

[6] Rybnikov A. I., Krukovsky P., Kolarik V., Tadlya K., Mojaiskaia N. V., Kryukov I. I., Juez-Lorenzo M. Lifetime prediction for gas turbine blades MCrAlY coatings. *Microscopy and Microanalysis*, V10, Suppl.

UDK 669.27
Original scientific article/Izvirni znanstveni članek

ISSN 1580-2949
MTAEC9, 45(1)27(2011)

REDUCTION OF ULTRA-FINE TUNGSTEN POWDER WITH TUNGSTEN (VI)-OXIDE IN A VERTICAL TUBE REACTOR

REDUKCIJA ULTRAFINIH PRAHOV VOLFRAMOVEGA(VI) OKSIDA V REAKTORJU Z VERTIKALNO CEVJO

Željko Kamberović[1], Dušica Filipović[2], Karlo Raić[1], Miloš Tasić[3], Zoran Anđić[3], Milorad Gavrilovski[3]

[1]Faculty of Technology and Metallurgy, Karnegijeva 4, 11120 Belgrade, SRB-11000
[2]IMPOL Seval a. d., Sevojno, SRB-11000
[3]Scientific Research Center, Veliki Park 1, 31000 Užice, SRB-11000
kamber@tmf.bg.ac.rs

Prejem rokopisa – received: 2010-09-14; sprejem za objavo – accepted for publication: 2010-11-09

The reduction of WO_3 with hydrogen in a vertical tube reactor is a new approach to the reduction of tungsten oxide compared to conventional procedures in a stationary layer. The advantage of this method is the intensive contact between the reducent and the oxide particles, a higher degree and a shorter time of reduction of only a few seconds, compared to the several hours processing time in a horizontal tube reactor.

The characterization of the WO_3 powder and of the tungsten powder included a SEM microstructural examination and DT/TG analyses. The SEM examination of the tungsten powder indicates the presence of small particles with a size of about 1 μm, also within an agglomerated porous foam structure. Tungsten powder with a particle size of less than 1 μm is obtained at an optimal temperature with a suitable flow of hydrogen, as a result of stretching and the cracking of large particles, first in the reaction zone, and then, due to appropriate shock of the temperature, outside of this zone.

Using an appropriate mathematical model, the degree of reduction and the time required for the formation of tungsten particles during the hydrogen reduction of WO_3 in a vertical tube reactor were determined. Experimental studies have shown that the degree of reduction of WO_3 with hydrogen in a vertical tube reactor increases with the temperature and the flow of hydrogen.

Keywords: tungsten (VI)-oxide, reduction, vertical tube reactor, tungsten powder

Redukcija WO_3 z vodikom v reaktorju z vertikalno cevjo je nov postopek v primerjavi s konvencionalnimi postopki v stacionarni plasti. Prednost postopka je intenziven kontakt med reducentom in oksidnimi zrni, kar izboljša in skrajša čas redukcije na nekaj sekund, medtem ko traja procesiranje v reaktorju z vodoravno celo nekaj ur.

Karakterizacija prahov WO_3 je obsegala SEM-opazovanje in DT/TG-analize.

SEM-opazovanje volframovega prahu odkrije prisotnost majhnih delov z velikostjo 1 μm s strukturo iz penastih aglomeratov. Volframov prah z velikostjo manjšo od 1μm dobimo pri optimalni temperaturi in ustreznem toku vodika kot rezultat obremenitve in razpokanja večjih delcev, najprej v reakcijski zoni nato pa zaradi temperaturnega šoka zunaj te zone.

Razvit je bil računalniški model za nastanek zrn volframa z redukcijo WO_3 z vodikom v reaktorju z vertikalno cevjo. Rezultati raziskave kažejo, da stopnja redukcije WO_3 raste s temperaruro in s tokom vodika.

Ključne besede: volframov(VI) oksid, redukcija, reaktor z vertikalno cevjo, volframov prah

1 INTRODUCTION

The more intensive development of science and industry requires the application of new materials with specific properties. The basis for most of these materials is rare metals and their alloys. Due to their good mechanical, electrical, electro-erosive, tribological and magnetic properties, tungsten and its alloys are frequently used materials in industry [1]. Besides, tungsten has a high melting temperature, a high boiling point, a low evaporation rate at high temperatures and a low thermal expansion coefficient.

In industrial conditions, these materials, are often submitted to a reduction process with a gas as the most commonly used reducent, which easily penetrates into the oxide pores and ensures a good contact with the surface and in the interior of the reduced material [2]. Recently, a number of authors investigated the synthesis of tungsten-based powders using different methods, such as: the sol-gel method, chemical method co-precipitation, processes of mechanical activation, and plasma reduction [3–7]. With the aim to obtain a pure tungsten powder, the latest world research is oriented toward the application of new reducing agents and the development of new or a modification of existing technological processes. The process of the reduction of tungsten oxide, due to the low reaction temperature and the high degree of purity of the obtained products, was the subject of extensive research [3,6,7]. The results indicated that the properties of the synthesized tungsten powder depend, above all, on the properties of the starting powders and of the parameters of the technological process, mostly its simplification. At the same time, the variation of the parameters of the technological process, such as the temperature and the flow of hydrogen, as well as the processing in isothermal and non-isothermal conditions,

led to the conclusion that with the process it is possible to obtain ultra fine, homogenous and loose tungsten powders. With the aim to shorten the time of the process, Lackner [8] performed the reduction of tungsten oxide in a vertical tube for four temperatures at (800, 900, 1000 and 1100) °C. The starting powder tungsten(VI)-oxide had an average particles size of 28 μm and tungsten powder particles with a size of 17.3 μm were obtained by a reduction at 1100 °C in 1.7 s.

A study of the mechanism and kinetics of hydrogen reduction of tungsten oxide pointed out that the main problem of this process is the formation of several sub-oxides as intermediate products [9–12]. The reduction of WO_3, occurs through the following stages of oxidation [8,13]: WO_3 (α-oxide) → $WO_{2,9}$ (β-oxide) → $WO_{2,72}$ (γ-oxide) → WO_2 (δ-oxide) → metal, α- or β-tungsten.

According to Fouad [10], the reduction of WO_3 with hydrogen occurs through three stages: WO_3 → $WO_{2.72}$ → WO_2 → W, where the activation energy is in the range from 100.48 kJ/mol to 133.98 kJ/mol. In accordance with [10,13,14], the reduction of WO_3 with hydrogen under isothermal conditions occurs in two stages: WO_3 → WO_2 → W, with the activation energy, according to Bustnes [15], of the reduction of WO_2 to W of 83kJ/mol. A kinetic analysis of the reduction of tungsten oxide in a vertical tube [8] indicates that the process occurs with an activation energy of 126 kJ/mol.

Although the most common method of producing tungsten powder is tungsten oxide reduction with hydrogen, the reaction conditions and the kinetics of other reducing agents, such as the reduction of WO_2 with carbon in the form of graphite or soot [16,17], resulting in pure tungsten, and the reduction of oxide tungsten with CO, when the WC is the final products were also investigated[18].

As a part of this study the process of hydrogen reduction of WO_3 powder in a vertical tube reactor was examined. It is a completely new approach to the reduction of oxides of tungsten, compared to conventional procedures in a horizontal tube reactor. The advantage of the procedure is the intensive contact between the reducing agents and the oxide particles, which results in a higher degree of reduction and a shortening of the reduction time to only a few seconds, while the process in a horizontal tube lasts for several hours.

2 EXPERIMENTAL

For the synthesis of ultra-fine tungsten powder with the reduction of tungsten oxide a vertical tube reactor was used. In **Figure 1**, the scheme of the apparatus for the reduction of WO_3 by hydrogen in a vertical tube reactor is shown. The apparatus consists of:

- a system of supply,
- gas-purifier system,
- units for heating,
- system to add a starting powder (vibration feeder),

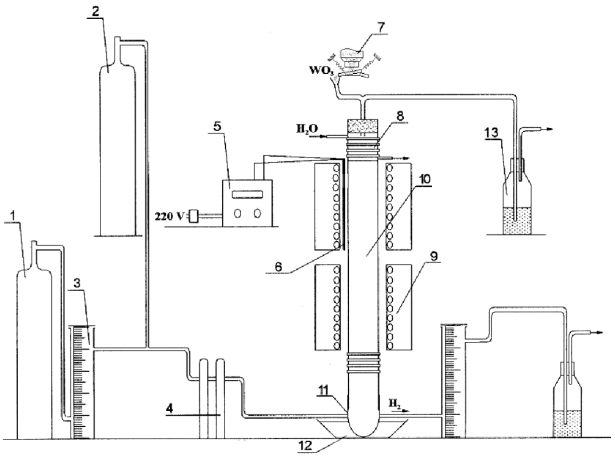

Figure 1: Schematic review of the apparatus for tungsten trioxide reduction in a vertical tube reactor. 1. Hydrogen bottle, 2. Nitrogen bottle, 3. Rotameter, 4. Purificiation columns, 5. Thermoregulator, 6. Thermopar, 7. Vibration supplier, 8. Radiator, 9. Electroresistant furnace, 10. Quartz tube, 11. Glass supplement, 12. Ice bowl, 13. Cleanser

Slika 1: 1. Jeklenka z vodikom, 2. Jeklenka z dušikom, 3. Rotameter, 4. Čistilne kolone, 5. Termoregulator, 6. Termopar, 7. Vibrator, 8. Radiator, 9. Elektrouporovna peč, 10. Kremenova cev, 11. Stekleni dodatek, 12. Posoda z ledom, 13. Čistilnik

- instruments for measurement and controlling the process,
- quartz tubes, diameter of 22 mm and height h = 540 mm,
- cooling system.

The system for gas supply consists of two bottles, one with compressed hydrogen and one with nitrogen. The bottle with hydrogen is connected through the rubber hose to the column containing $CaCl_2$, which is further connected through the rubber hose to a rinser with sulphuric acid, both used to remove moisture from the hydrogen. The flow of gas at the exit from the bottle with hydrogen is measured with a flowmeter. The quartz heating tube is used in an electric furnace. The process parameters are the temperature and the flow of hydrogen. The holding time of the WO_3 powder particles in the furnace reaction zone is calculated using an equation based on values of the relevant parameters: tube length, particle diameter, particle density, gas speed, gas density, viscosity and gravity. The temperature is measured and controlled with a thermoregulator, connected to the furnace with a PtRh-Pt thermocouple. The quartz tube (inner diameter, ϕ = 22 mm and height, h = 540 mm) is placed vertically through the furnace and it is attached to the metal frame. The tube is closed from both sides with rubber seals. The part of the quartz tube in the furnace is cooled using a copper heat sink, of spiral form, through which water circulates. The oxygen supply and the drain occur from the bottom of the quartz tube. At the end the hydrogen hose outlet has a rinser with water that serves as a powder collector. During the process of reduction, the bottom of the quartz tube is placed in a glass cup filled with cold water and ice, and the Pyrex powder

collector is completely submerged to prevent the re-oxidation of the reduced particles. This will achieve additional stresses in the particles due to cracking thermoshocks, which leads to their fracture. On the quartz tube top a rubber seal is placed and it is drawn into the glass tube with a rubber hose. A glass funnel is placed to the rubber hose in which a certain amount of powder is inserted. The inner diameter of the glass funnel is 4.75 mm and outside is 7.75 mm. The powder dosing is accomplished with a vibratory feeder. At the end of this hose there is a rinser with water.

Synthetic powder of tungsten (VI)-oxide (Merck, Dermstadt) with a particle size of less than 30 μm was used as a base material. This material is hygroscopic and prone to agglomeration. Before the reduction process, WO_3 powder is dried at a temperature of 100 °C. Occasionally, the powder was taken out from the dryer and mechanically ground. To remove the remaining agglomerates, after the completion of the drying process, the powder is sifted through a sieve with 63 μm holes.

The WO_3 powder's hydrogen reduction was carried out at six temperatures (700, 725, 750, 800, 850 and 900) °C and four hydrogen flow rates (10, 20, 30 and 50) dm^3/h.

The characterization of the used WO_3 powder and of the obtained tungsten consisted of a SEM microstructural examination and a DT/TG analysis. The SEM analysis was carried out using a JEOL T20 JSM 5300 microscope. For the DT/TG analysis, a NETZCH STA model 409EP with a maximum temperature of 1100 °C was used. A thermocouple Pt-Pt-Rh S type (10 % Rh) and a reference material α-Al_2O_3 were used.

The degree of reduction was determined and, using the appropriate mathematical model, the time required for the formation of tungsten particles during the hydrogen reduction of tungsten in a vertical tube reactor was deduced. Based on the obtained results the influence of the temperature, the time and the hydrogen flow on the reduction degree of tungsten trioxide were determined.

3 RESULTS AND DISCUSSION

In **Figure 2**, the initial powder of synthetic WO_3, and in **Figure 3**, the initial powder of synthetic WO_3 after drying, grinding and sifting are shown. The examination of the initial powder of synthetic WO_3 (**Figure 2**) indicates large agglomerates with a size of 80 μm and particles smaller than 30 μm. After drying, grinding and sifting, an irregular shape of particles with a size below 15 μm and large agglomerates of size below 40 μm consisting of a great number of small particles connected to one another are observed. In addition, small particles cover the large as a patch and cause a spongy morphology. Since the initial powder is very fine and hygroscopic, the primary 'condition' for agglomerate formation is fulfilled. Namely, the agglomeration of the small particles is due to their large surface, i.e., a high surface energy and the interaction through Van der Waals forces that exist between them.

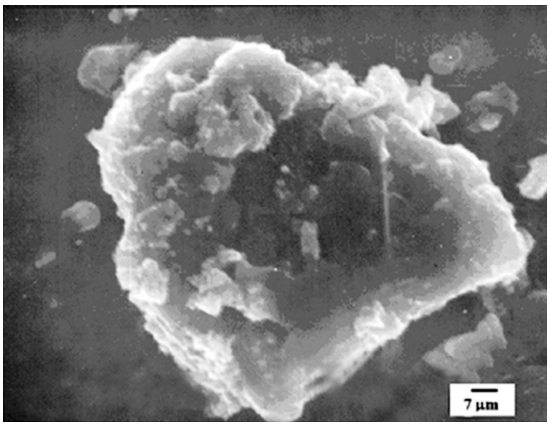

Figure 2: SEM of the initial WO_3 powder
Slika 2: Posnetek začetnega prahu WO_3

Figure 4 shows the resulting tungsten powder in the form of a porous agglomerate of size less than 30 μm. Also, particles of tungsten of size about 1 μm and smaller, particles are present suggesting that the reduction process contributed to the fragmentation of the powder particles.

Figure 5 indicates clearly the presence of a large, porous foam structure agglomerate with a size of about 50 μm with smaller agglomerates in the background. All the agglomerates consist of single particles smaller than 1 μm. The occurrence of the porous tungsten powder is explained by the fact that the reduction reaction was heterogeneous and chemically controlled.

The reduction speed was determined from the speed of the chemical reaction at the interface of the oxide/product, which causes the porosity of tungsten powder. Tungsten powder particles with a size of less than 1 μm are produced with stretching and cracking of the large particles in the reduction zone. The hydrogen molecules diffuse through the surface of the WO_3 particles and metal tungsten nucleation may occur at the begin-

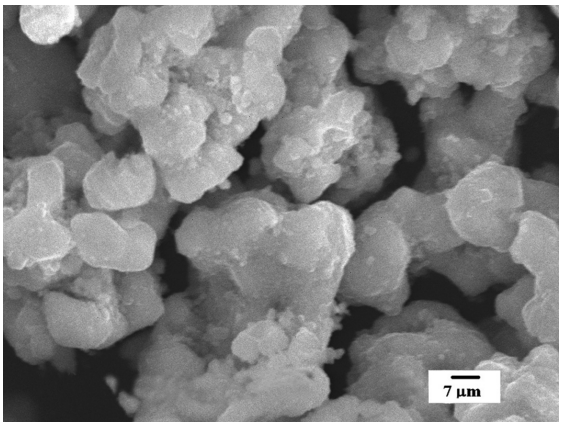

Figure 3: SEM of the initial WO_3 powder after drying, grinding and sifting
Slika 3: Začetni prah WO_3 po sušenju, drobljenju in sejanju

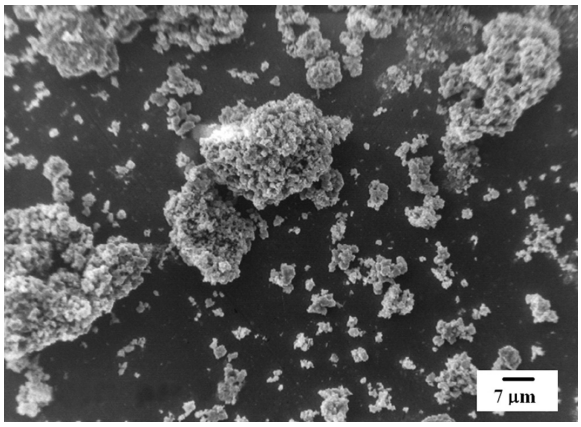

Figure 4: SEM of the obtained tungsten powder
Slika 4: SEM-posnetek pridobljenega volframovega prahu

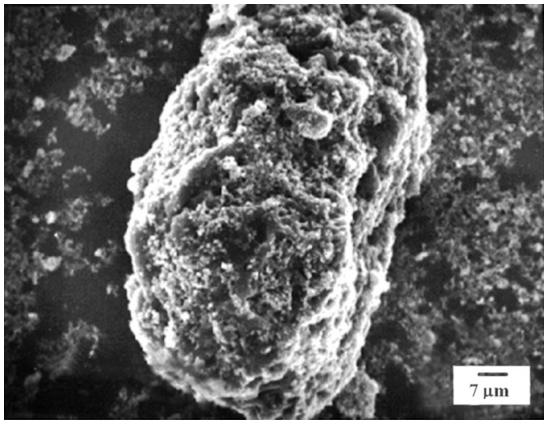

Figure 5: SEM of the obtained tungsten powder
Slika 5: SEM-posnetek pridobljenega volframovega prahu

ning of the process of reduction; however, tungsten nuclei begin to grow when most of the WO_3 is changed into WO_2. The released oxygen surplus created during the transformation of WO_3 into WO_2 diffuses through the surface and reacting with hydrogen, creates steam, which as reduction product becomes trapped in the WO_3 lattice. The steam and the growth of tungsten nuclei cause stresses and later the cracking of larger oxide particles into smaller fragments. Additional stresses occur during the transition of reduced particles from the furnace reaction zone, heated to a temperature of 900 °C in the unheated to the quartz tube zone and during cooling in the collector iced water. The temperature shock causes the rupture and further fragmentation of particles. The described reduction mechanism suggests that the process advances in two stages.

The degree of reduction was determined stoichiometrically from the weight difference of the starting WO_3 powder and the reduced tungsten powder, i.e., the differences in the amounts of oxygen. **Table I** shows the obtained experimental values of the degree of reduction.

The time when the WO_3 particles fall through the quartz tube of the vertical reactor during the reduction process could not be precisely determined with a simple measurement using a stopwatch. For this reason, it was determined using the appropriate mathematical model based on the physical laws of the movement of particles through a fluid, i.e., on the application of Stock's law to the moving of one particle through the fluid. One of the conditions of the application Stock's law is that the particles diameter is not greater than 50 µm [19,20], a condition that was fulfilled as the starting WO_3 powder mean particles size was about 30 µm.

According to Stock's law, the speed limit of small spherical particles which fall out of the fluid is:

$$V_t = \frac{2R^2(\rho_s - \rho)g}{9\eta} \quad (1)$$

where:
ρ_s – particle density,
ρ – fluid density,
η – dynamic viscosity,
g – acceleration due to gravity,
R – diameter of a spherical particle,
V_t – speed of depositing particles.

In this case, the time for a small spherical particle to fall through the fluid which streams in the opposite direction is:

Table 1: Experimental values of the degree of reduction and the mathematically calculated values of the reduction time of the tungsten trioxide particles

Temperature, T/°C	700	725	750	800	850	900
q/dm^3/h	10	10	10	10	10	10
α/%	24	29	34	44	53	59
t/s	3.04	3.1	3.16	3.29	3.42	3.53
q/dm^3/h	20	20	20	20	20	20
α/%	35	42	49	60	67	74
t/s	3.28	3.36	3.44	3.62	3.78	3.95
q/dm^3/h	30	30	30	30	30	30
α/%	45	53	60	70	78	84
t/s	3.55	3.65	3.76	3.99	4.21	4.44
q/dm^3/h	50	50	50	50	50	50
α/%	65	72	78	88	95	99
t/s	4.32	4.51	4.69	5.12	5.58	6.09

$$t = \frac{1}{v_t - v_{gas}} \quad (2)$$

where:
l – length of the tube reaction zone,
v_t – speed of a spherical particle,
v_{gas} – fluid rate.

Since the particle does not flow through an unlimited fluid, but through a fluid in a dish, the influence of the walls on the dish during the particles' falling must be taken into account. If a particle falls on the axis cylinder dish, the actual fall time is shorter and it is [20]:

$$t^* = \frac{t}{1+\left(\frac{9}{4}\frac{r}{R}\right)+\left(\frac{9}{4}\frac{r}{R}\right)^2} \quad (3)$$

where:
R – dish diameter,
r – distance from the dish's central axis.

In **Table I** the obtained experimental values for the degree of reduction and the mathematically calculated values of the reduction time for the tungsten trioxide particles are shown.

The described mathematical model to determine the time refers to a single particle. However, during the reduction of tungsten trioxide powder in a vertical tube reactor the particles fall in the form of small agglomerates. The particle agglomerates mass is significantly greater than the mass of one particle and for this reason, the falling speed of the agglomerated particles is higher than the falling speed of single particles. For this reason, the actual reaction time with hydrogen is less than 1 s.

Based on the obtained results, shown in **Table I**, the analysis of the influence of temperature, time and hydrogen flow on the degree of reduction of tungsten trioxide was carried out. The influence of the temperature and time on the degree of reduction of WO_3 is shown in **Figure 6**. The reduction degree of tungsten trioxide increases with the temperature and the highest values (reduction degree 99 %) were achieved at a temperature of 900 °C. In **Figure 7** the dependence of the degree of reduction of tungsten trioxide on hydrogen flow is shown.

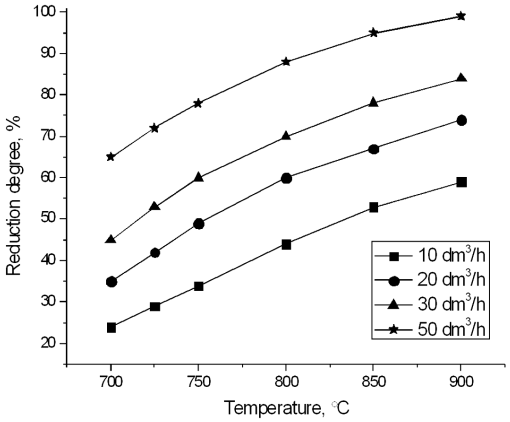

Figure 7: Influence of the flow of hydrogen on the degree of reduction for the WO_3
Slika 7: Vpliv toka vodika na stopnjo redukcije WO_3

With an increasing of the gas flow, the reduction degree increases and the greatest degree of reduction is achieved with a hydrogen flow of 50 dm³/h. This phenomenon is explained as a result of the increasing gas-adsorption properties with its quantity increase per unit of time and the increase of the diffusion coefficient, which is greater with a smaller molecular weight of gas. Bearing in mind that hydrogen has the smallest molecular mass of all known gas reducers, i.e., a high coefficient of diffusion, it is clear that the speed of penetration of hydrogen into small, spherical particles of tungsten trioxide is high, and therefore the degree of reduction of the oxide is greater.

During the experiment the analyses of the DT and DG (**Figure 8**) of obtained tungsten powder were also carried out. The described mechanism of reduction indicates that the process goes through two stages and it is completely in accord with the results of the DT analysis, where two exothermic peaks, at 365 °C and 469

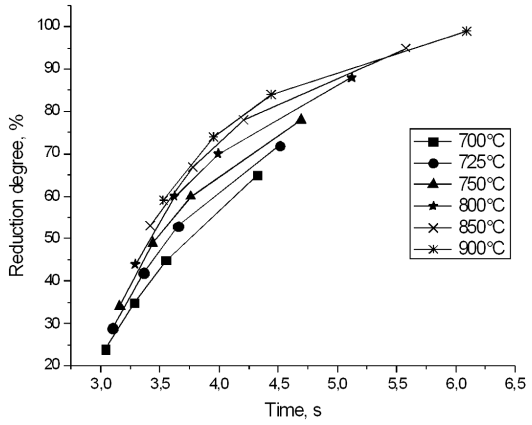

Figure 6: Influence of temperature and time on the degree of reduction for the WO_3
Slika 6: Vpliv temperature in časa na stopnjo redukcije WO_3

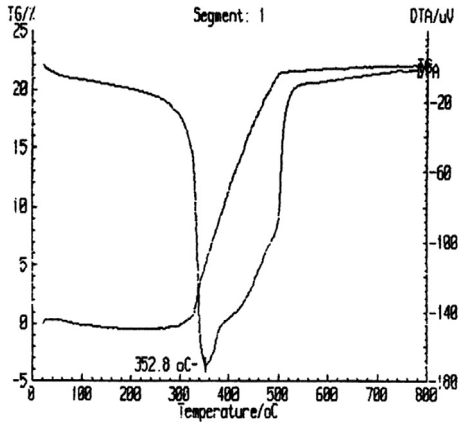

Figure 8: DT/TG analysis of tungsten powder
Slika 8: DT/TG-analiza volframovega prahu

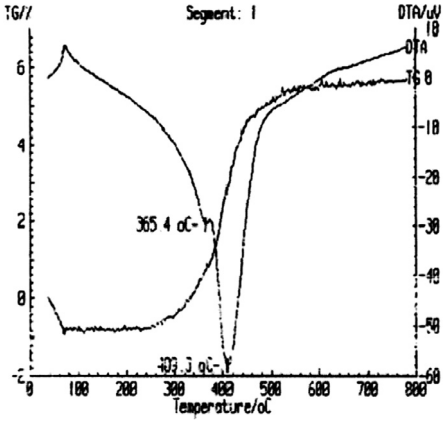

Figure 9: DT/TG analysis of sample W + W_xO_y
Slika 9: DT/TG-analiza vzorca W + WO_3

°C, respectively (**Figure 9**) were observed for the sample W + W_xO_y.

The TG analysis shows a mass increase in the oxidation of tungsten (250–500 °C) to a value of 22.61 %. The increase in mass in this temperature zone for pure tungsten is 26.14 %, and this indicates that the examined tungsten sample was not totally pure, i.e., that it contained a significant content of oxides of tungsten. Based on these results, the calculated degree of reduction is 86.49 %, and in agreement with the experimental results obtained (88 %) with the appropriate stoichiometric analysis.

4 CONCLUSION

With the reduction procedure in a vertical tube reactor, tungsten powder with particles of size less than 1 μm were obtained. Compared to conventional procedures performed in a stationary layer the procedure is a new approach to the reduction of oxides of tungsten. The advantage of this method is intensive contact between the reducent and the oxide particles, which results in a higher degree of reduction and a shortening of the reduction time to only a few seconds, when compared to the process in a horizontal tube reactor of several hours that results in a less-reduced powder.

Tungsten powder particles with a size of less than 1 μm were obtained for the optimum temperature conditions and flow of hydrogen as result of the stretching and cracking of large particles, first in the reaction zone and then, due to an appropriate temperature shock, outside of this zone. The obtained tungsten powder shows a similar tendency to agglomerate as the basic tungsten trioxide powder and the agglomerate formed is due to its large area and the high surface energy and the effect of the attractive forces.

The described mechanism of reduction indicates that the process occurs in two stages and in accordance with the results of the DT analysis, where two exothermic peaks can be observed, at 365 °C and 469 °C, respectively, for the sample W + W_xO_y. Based on the results of the TG analysis a degree of reduction of 86.49 % is calculated, which is in good agreement with the experimental results obtained (88 %) with the stoichiometric analysis.

The results showed that the degree of hydrogen reduction of WO_3 in a vertical tube reactor increases with temperature and the highest values (99 %), achieved at 900 °C, of less than 1 s indicate that the process is very fast and intensive. With an increasing of the gas flow, the degree of reduction increases and the highest values were achieved with a hydrogen flow of 50 dm^3/h.

Further research will be aimed towards optimizing the process of reduction in a vertical tube reactor with intensification of the reactions and cost-reduction. Also, it would be useful to achieve a separation of the large fractions of powder at the exit of the quartz tube and their redirection in the process of reduction and obtain a circular system and therefore a higher efficiency of the process.

5 REFERENCES

[1] A. Hesham, E. Abdel-Hady, S. Sesnadri, Metallurgical and Materials Transactions B, 41B (**2010**), 161–172
[2] W. Tremel, H. Kleinke, V. Derstroff, C. Reisner, J. Alloys Compd., 219 (**1995**), 471–475
[3] A. Al Mohammad, Acta Physica Polonica A, 116 (**2009**), 240–244
[4] M. C. Yang, J. Xu, Z. Q. Hu, Int. J. Refractory Metals Hard Mater. 22 (**2004**), 1
[5] Z. Xiong, G. Shao, X. Shi, X. Duan, L. Yan, Int. J. Refractory Metals Hard Mater. 26 (**2008**), 242
[6] A. Al Mohammad, Phys. Status Solidi A 205 (**2008**), 2880
[7] G. Da Silva G, C. Alves, V. Hajek, A. Da Silva, G. P., International journal of powder metallurgy, 41 (**2005**) 4, 43–50
[8] A. Lackner, A. Filzwieser, P. Paschen, Int. J. Refractory Metals Hard Mater. 14 (**1996**), 383
[9] L. Jiqiao, C. Shaoyi, Z. Zhiqiang, L. Haibo, H. Baiyun, Int. J. Refractory Metals Hard Mater. 17 (**1999**), 233
[10] N. E. Fouad, Journal of analytical and applied pyrolysis, 44 (**1997**), 13–28
[11] N. Fouad, A. Nohman, M. Zaki, Thermochimica Acta 343 (**2000**), 139–143
[12] S. Eroglu, T. Baykar, Journal of Materials Processing Technology 103 (**2000**), 288–292
[13] P. Taskinen, M. H. Tikkanen, Scandinavian Journal of Metallurgy 6 (**1997**), 228–232
[14] J. A. Bustnes, D. Sichen, S. Seetharaman, EPD Congres, The Minerals, Metals & Materials Society, (**1993**), 581–600
[15] J. A. Bustnes, D. Sichen, S. Seetharaman, Metall. Trans. B, 24B (**1993**), 475
[16] D. Venables, M. Brown, Thermochimica Acta 282/283 (**1996**), 251–264
[17] D. Venables, M. Brown, Thermochimica Acta 282/283 (**1996**), 265–276
[18] D. Venables, M. Brown, Thermochimica Acta 291 (**1997**), 131–140
[19] D. R. Poirier, G. H. Geiger, Transport Phenomena in Materials, Processing, TMS, Warrendale, Pennsylvania, USA (1994)
[20] D. Filipović, K. Raić, M. Knežević, M. Tasić, A. Vujović, Reduction of tungsten oxide in vertical tube reactor. Mathematical model for estimate time of reduction, 4th Balkan Conference on Metallurgy, Proceedings, Zlatibor, Serbia, 2006, 311–316

UDK 533.5:543.428.2
Original scientific article/Izvirni znanstveni članek

ISSN 1580-2949
MTAEC9, 45(1)33(2011)

OXYGEN DIFFUSION IN THE NON-EVAPORABLE GETTER St 707 DURING HEAT TREATMENT

DIFUZIJA KISIKA V GETRU St 707 MED TOPLOTNO OBDELAVO

Sefer Avdiaj[1,2], Barbara Šetina - Batič[2], Janez Šetina[2], Bojan Erjavec[2]

[1]Lotrič, d. o. o, Selca 163, 4227 Selca, Slovenia
[2]Institute of Metals and Technology, Lepi pot 11, 1000 Ljubljana, Slovenia
sefer.avdiaj@imt.si

Prejem rokopisa – received: 2010-08-26; sprejem za objavo – accepted for publication: 2011-01-11

The oxygen diffusion and microstructure were investigated in specimens of commercial Non Evaporable Getter under the trademark of St 707, which is an alloy of Zr(70)-V(24.6)-Fe(5.4) using EDS, AES and XRD. Specimens were in the form of tablets compressed from St 707 powder of typical particle size from 50 μm to 100 μm. To obtain an observable amount of oxygen in the bulk material, we loaded the getter specimen at 450 °C at oxygen partial pressure of $1.2 \cdot 10^{-4}$ Pa for 1 h. Using AES and EDS we investigated the distribution of oxygen in different phases of the alloy. From the concentration profile, we can see the considerable diffusion length of the oxygen into the getter. This diffusion length is much larger in the Laves phase compared to the zirconium phase. On the zirconium phase two different layers are formed, an oxide layer composed of ZrO_2 followed by a diffusion layer, while on the Laves phase only a diffusion layer can be found. In this paper, we also determined the phases present in our materials, as well as the changes of these phases after oxidation.

Keywords: diffusion, oxidation layer, getter, zirconium, Laves phase

Preučevali smo mikrostrukturo in difuzijo kisika v neuparljivih getrih St 707(zlitina Zr(70)-V(24,6)-Fe(5,4)) z metodami EDS, AES in XRD. Preizkušanci so bili v obliki stisnjenih tablet z značilno velikostjo delcev med 50 μm in 100 μm. Pri temperaturi 450 °C smo preizkušance izpostavili kisiku pri tlaku $1.2 \cdot 10^{-4}$ Pa za 1 h. Z metodami AES in EDS smo opazili različno povečanje vsebnosti kisika v različnih fazah zlitine. Iz koncentracijskega profila je razvidna velika difuzijska dolžina za kisik v getrskem materialu. V Lavesovih fazah opazimo znatno daljšo difuzijsko dolžino kot v cirkonijevi fazi. Na površini cirkonijeve faze smo našli dve različni plasti. Na vrhu je oksidna plast ZrO_2, ki ji sledi difuzijska plast. V Lavesoih fazah pa najdemo le difuzijsko plast. Prav tako smo ugotovili fazno sestavo materiala in spremembe zaradi oksidacije.

Ključne besede: difuzija, plast oksidacije, geter, cirkonij, Lavesove faze

1 INTRODUCTION

Getters are solid materials capable of chemisorbing gas molecules to their surface: getters are chemical pumps. Non-evaporable getters are applied in vacuum systems where a very low partial pressure of hydrogen is required, e.g., in ultra-high-vacuum (UHV) chambers [8]. Because they exhibit selective pumping, they are also used for inert-gas purification. In general, getters are classified into two main groups: evaporated getters (EGs) and non-evaporated getters (NEGs). During the handling of NEGs under usual ambient conditions their surface becomes covered with a passive layer consisting mainly of chemisorbed oxygen and carbon. But a surface phenomenon is not the only characteristic of NEGs. This passive layer must be eliminated to start the gettering action and the metal surface is less oxidized after O_2 exposure to high temperatures than at low temperatures, because the oxygen diffuses from the surface into the bulk [7]. The process of activation of the getter is described in [1,5,11,12]. Lately, getters have found widespread application in various fields, such as ultra-high-vacuum systems of particle accelerators, sealed vacuum devices such as vacuum tubes, and field emission displays. In this study (St 707) non-evaporable getter material has been investigated. Techniques such as Energy-Dispersive Spectroscopy (EDS), Auger Electron Spectroscopy (AES) and X-Ray Diffraction (XRD) were used for the material characterization.

2 EXPERIMENTAL

Our specimen is an alloy with mass fractions of Zr(70)-V(24.6)-Fe(5.4) %. In the typical procedure, specimens were prepared through grinding and polishing, and then immersing in an ultrasonic bath with alcohol for cleaning. Then the specimens were inserted into the test chamber (CH2), **Figure 1**. Then we pumped the gases out of the CH2 (through the turbomolecular pump) until the pressure in the vacuum chamber reached 10^{-7} mbar. Afterwards, the specimen was heated for activation, and simultaneously the temperature was measured by a thermocouple attached to CH2. In the experiment the specimen surface was exposed to the given partial pressure of test gas at elevated temperature. The sources of the test gases are gas cylinders. When desired temperature was reached, the regulating valve was opened and the gas (in our case pure oxygen) is permitted to flow into the system. Opening of the regulating valve was controled to reach the pressure of $1.2 \cdot 10^{-4}$ Pa in the CH2, while, the temperature was 450 °C. The specimen was treated at this conditions, for a time of one hour. During this treatment the diffusion of

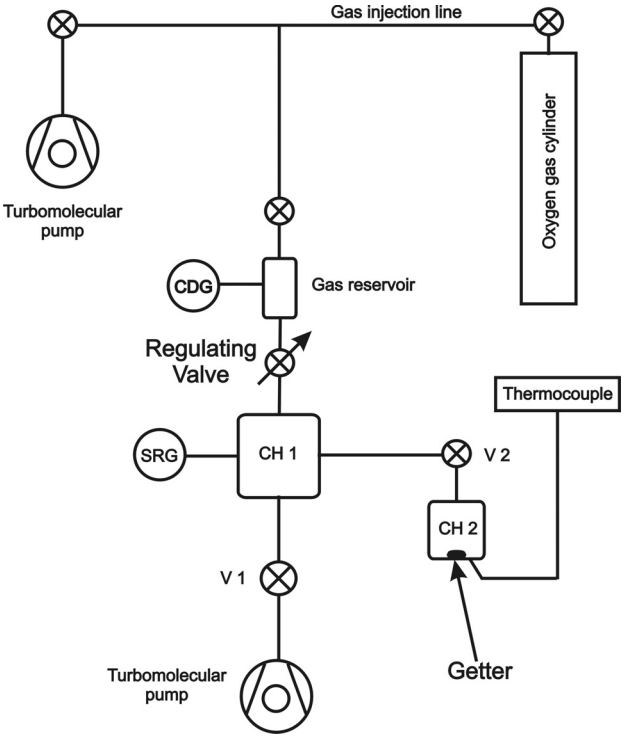

Figure 1: Experimental setup of the vacuum system. SRG is Spinning Rotor Gauge, CDG is Capacitance Diaphragm Gauge.

Slika 1: Eksperimentalna postavitev vakuumskega sistema. SRG je viskoznostni vakuumski merilnik in CDG kapacitivni membranski merilnik.

O_2 into the specimen started. The purity of the oxygen admitted to the getter sample was better than 99.99 %.

The investigation of the diffusion depth of oxygen was performed using SEM and AES with different accelerating voltages and different magnifications. The crystal structures of the obtained specimen were characterized by powder X-ray diffraction (XRD). The specimens were characterized in both the as-received and oxidized states.

3 RESULTS

3.1 EDS analyses

The compositions of the constituents of the as-received St 707 specimen and after their oxidation in the vacuum system were investigated by EDS. The results of the EDS investigations are summarized in **Table 1** and **Figures 2a and 3a**. The specimen in the as-received state contained particles which consisted of two different compositions of zirconium-rich phase and Laves phase, as can be seen from **Figure 2a**. Areas rich in zirconium are surrounded by those with which vanadium is the major component. It was found that iron is present only in the vanadium-rich areas [2]. According to **Figure 2** and **Figure 3**, the bright areas in the secondary electron images could be assigned to areas rich in elemental zirconium, whereas the dark ones indicate the dominance of the Laves phase.

When the getter is exposed to air, it absorbs oxygen and the gases present in the atmosphere. As consequence, a layer is formed at its surface which prevents further adsorption. For further use of the getter it should be activated, which is achieved through increasing the temperature. For this reason, a small amount of oxygen will be found in the "as-received" getter, **Figures 2a and 3a**. The presence of oxygen in the "as-received" specimen is barely noticeable compared to the oxygen presence in the oxidized specimen **Figures 2b and 3b**, and **Table 1**. Also in the "as-received" specimen the presence of oxygen is almost similar in all phases, the zirconium-rich phase and the Laves phase.

From the EDS spectra as well as the EDS elemental mapping images of the as-received getter material it is obvious that the amount of oxygen is almost the same in

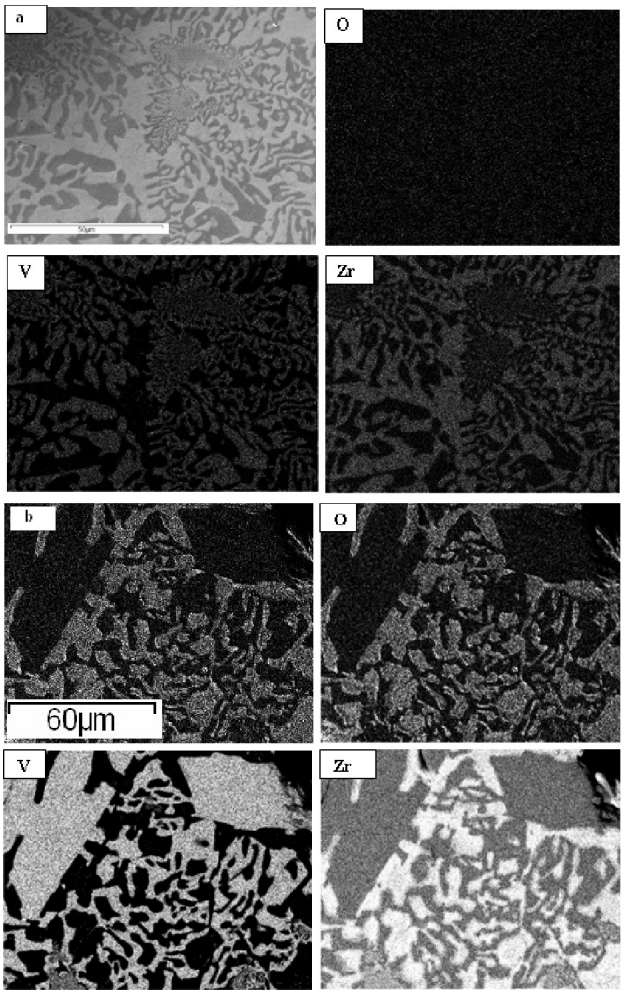

Figure 2: (a) Secondary-electron image of a polished surface of the as-received St 707 specimen and element distribution images for O, V, and Zr. (b) Secondary-electron image of a polished surface of the oxidized specimen St 707 at temperature T = 450 °C, pressure P = $1.2 \cdot 10^{-4}$ Pa, and time t = 1 h and the element distribution images for O, V, and Zr

Slika 2: (a) Polirana površina preizkušanca St 707 in porazdelitev elementov O, V in Zr. (b) Polirana površina oksidiranega preizkušanca St 707 pri temperaturi T = 450 °C, tlaku P = $1.2 \cdot 10^{-4}$ Pa za čas t = 1 h ter porazdelitev elementov O, V in Zr

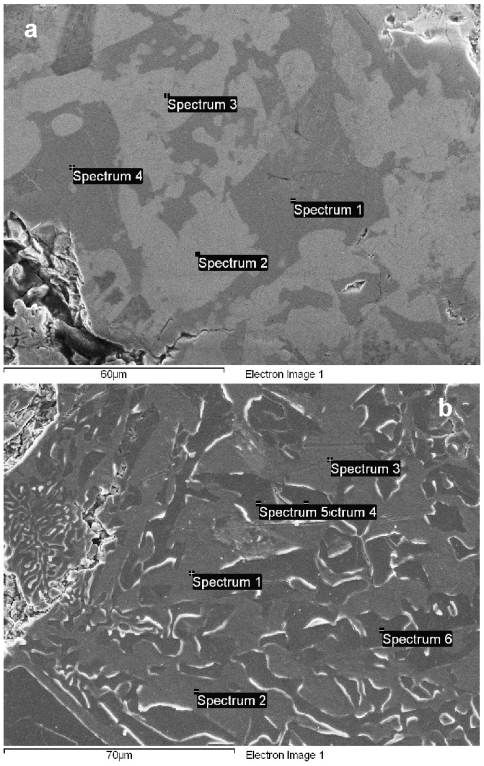

Figure 3: EDS analyses: a) as-received specimen, the presence of oxygen is almost the same in both phases b) EDS analyses for "oxidized" specimen in different phases, oxygen is more present in the zirconium than in the Laves phase

Slika 3: EDS-analize: a) začetni material, kjer je vsebnost kisika v obeh fazah podobna, b) pri oksidiranem preizkušancu je vsebnost kisika v zirkonski fazi večja kot v Lavesovi.

Table 1: Composition of "as-received" specimen and "oxidized" specimen using EDS

Tabela 1: Sestava začetnega in oksidiranega preizkušanca

	O	V	Fe	Zr	Total
Spectrum "as-received " specimen					
Spectrum 1	13.32	45.28	9.31	32.09	100
Spectrum 2	14.94	4.93	0.00	80.12	100
Spectrum 3	12.52	8.99	0.00	78.48	100
Spectrum 4	18.82	42.07	8.99	30.12	100
Spectrum "oxidized" specimen					
Spectrum 1	59.75	4.47	0.00	35.78	100
Spectrum 2	60.99	0.45	0.00	38.56	100
Spectrum 3	60.48	1.81	0.00	37.70	100
Spectrum 4	19.29	40.69	9.07	30.95	100
Spectrum 5	16.46	41.41	9.85	32.28	100
Spectrum 6	0.00	51.88	10.86	37.25	100

both phases, the zirconium-rich phase and the Laves phase **Figure 2a**. On the other hand, through the same techniques we observed a larger oxygen content in the zirconium-rich phase compared to the Laves phase (**Figure 2b**). Also from **Figure 3** and **Table 1** it is evident that there is more oxygen in the zirconium-rich phase than in the Laves phase. The spectrums 1, 2, 3 are of the zirconium-rich phase and spectrums 4, 5, 6 are of the Laves phase. Measured oxygen concentration in spectrums 1, 2 and 3 of oxidized specimen is close to 60%. This happened due to the fact that close to 500 °C the formation of ZrO_2 bond occurres [2] and also the solubility values indicate that metals of the 4th group (in our case zirconium) have higher storage capacities for oxygen than those of the 5th group (V), or, putting it another way, that hcp crystalline structures have in general higher storage capacities than the bcc ones [11].

3.2 AES analyses

The surface of the getter materials is particularly difficult to analyze because of their high chemical reactivity. The results obtained can, therefore, be strongly influenced by the experimental set-up and the procedures [3,4], as recently confirmed through our measurements. The AES results are also compared with complementary

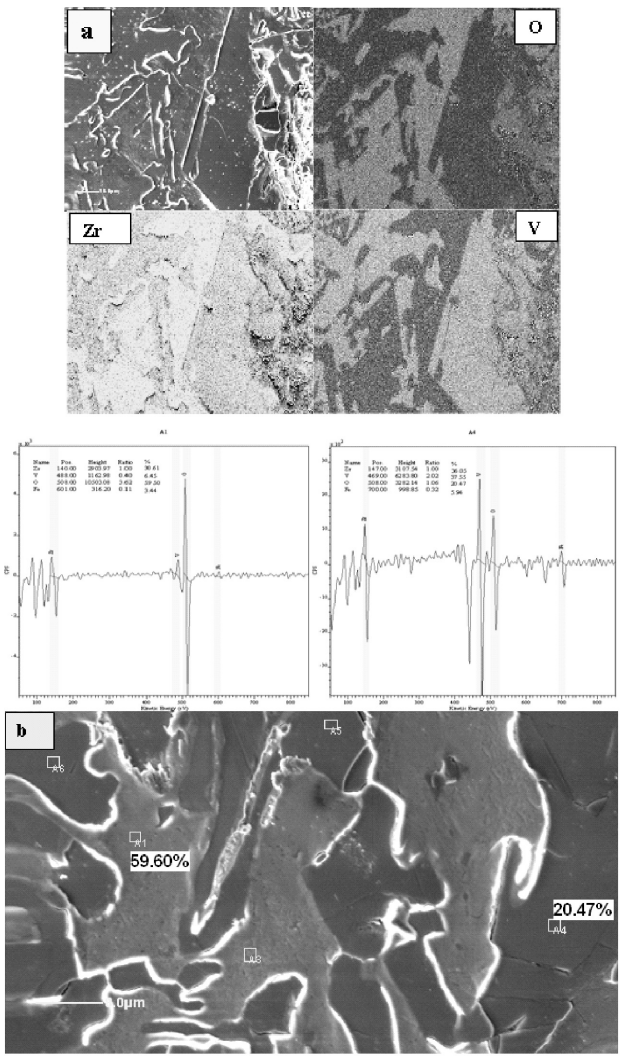

Figure 4: (a) Two-dimensional element distribution images for O, V, and Zr by Auger Electron Spectroscopy on a polished surface of the oxidized St 707 alloy, (b) AES analyses for "oxidized" specimen in different phases, more oxygen is present in Zr (spectrum A1-59.50 %) than in the Laves phase (spectrum A4-20.47 %)

Slika 4: (a) AES ploskovna porazdelitev elementov O, V in Zr na polirani površini oksidiranega St 707 (b) AES točkovna analiza oksidiranega preizkušanca v različnih fazah, kjer je razvidno, da je v Zr-fazi povečana koncentracija kisika glede na Lavesovo fazo.

EDS measurements. The results from the AES, **Figure 4**, are similar to those obtained with EDS, **Figure 3**. Again, we can observe that oxygen is more present in the Zr-rich phase than in the Laves phase. From **Figure 4** we see that the presence of oxygen in atomic percent (in the depth 41 nm) in the Zr (spectrum 1) is 59.50 %, and in the Laves phase (spectrum 4) is 20.47 %. Also, from mapping, a larger oxygen content in Zr compared to the Laves phase (**Figure 4a**) was observed. In addition, a larger amount of oxygen in the grain boundary and grain particles is observable, because the grain boundaries, as dislocations, are considered as short-circuits for atomic diffusion in metals [11].

AES depth profiling measurements were made at some points of the specimen in order to be able to estimate the penetration depth of the oxygen within the getter, concretely for the zirconium-rich phase, (**Figure 5a**) and the Laves phase (**Figure 5b**). This measurement technique makes it possible to distinguish the oxidized zone (the presence of ZrO_2) and the diffused zone (the zone where oxygen is inserted). Because of the formation of ZrO_2 chemical bond in the zirconium-rich phase there is the presence of the oxidized layer. This oxidized layer is absent in the Laves phase. On the other hand, the thickness of the diffused layers is higher for the Laves phase compared to the zirconium-rich phase.

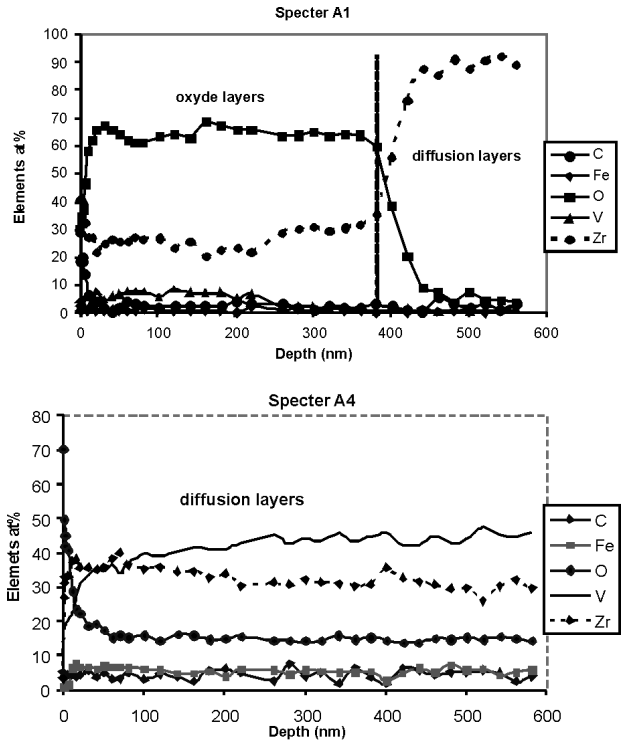

Figure 5: AES depth profiles for a) Zr phase and b) Laves phase at 450 °C for 60 min

Slika 5: AES globinski profil za a) Zr-fazo ter b) Lavesovo fazo. Preizkušanec je bil oksidiran pri temperaturi 450 °C, 60 minut.

3.3 X-ray diffraction analysis

XRD analyses were carried out in order to determine the phases present in the materials. We confirmed that the as-received alloy is biphasic at room temperature (300 K), consisting of hexagonal α-Zr and the cubic Laves phase $Zr(V_{1-x}Fe_x)_2$ as shown in **Figure 6a** and indicated in references [2,10]. We can see in **Figure 6b** that for the sample treated at 450 °C under oxygen partial pressure of $1.2 \cdot 10^{-4}$ Pa the intensity of the Laves phase will decrease and, at the same time, a new phase of ZrO_2 will emerge. This new phase comes as consequence of ZrO_2 bond formation at high temperatures. The ZrO_2 has a monoclinic structure. The as-received specimen exhibits narrower XRD peaks, while with the oxidized specimen a certain broadening of the peaks (mainly Laves phase) due to lattice strains and distortions can be observed.

4 DISCUSSION

The diffusion length during the time t at temperature T is given by [13]:

$$L = \sqrt{D(t) \cdot t}$$

where L/cm is the thickness, D/(cm^2 s^{-1}) is the diffusion coefficient and t/s is the time. The diffusion coefficient (or diffusivity) in the metal at temperature T is:

$$D = D_0(t) \cdot \exp\left(-\frac{E}{RT}\right)$$

D_0 is a constant, E is the activation energy for diffusion, and R is the universal gas constant. In the literature 15 we have found following values for hexagonal α-Zr (mean of two data): D_0 = 0.21 cm^2/s and E = 184.1 kJmol^{-1}K^{-1}, and for cubic V: D_0 = 0.013 cm^2/s and E = 121.3 kJmol^{-1}K^{-1}. Using these values we get for Zr: $D(T = 723\ \text{K}) = 1.3 \cdot 10^{-14}$ cm^2/s and for V: $D(T = 723\ \text{K}) = 2.6 \cdot 10^{-11}$ cm^2/s.

The corresponding diffusion lengths for 1 h treatment at 450 °C are 70 nm for Zr and 3050 nm for V. We can

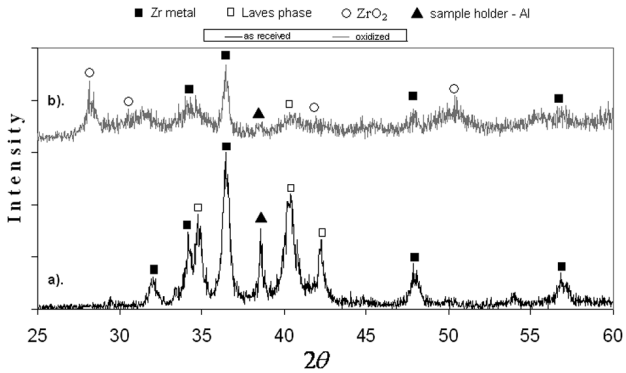

Figure 6: X-Ray diffraction spectra: a) as-received specimen, b) oxidized specimen at 450 °C for 1 h

Slika 6: XRD-spektri: a) začetni preizkušanec, b) oksidiran preizkušanec pri temperaturi 450 °C in času 1 h

see from **Figure 5a** that in the diffusion layer in Zr the drop of oxygen concentration from 66 % to nearly zero occurs in approximately 100 nm. Because of almost 50 times larger diffusion length in V we can not see in **Figure 5b** a considerable change of oxygen concentration in Laves phase over the investigated depth of 600 nm.

The data for the diffusivity and the solubility limit from the literature give us a global view about the diffusivity and solubility limit in single-crystal pure metals. However, the NEG materials under investigation are alloys. The diffusivity and the solubility-limit values that can be found in the literature are valid for single crystals, so they are not very helpful to evaluate the diffusivity and the solubility limit in the case of alloy. It is known that the diffusivity and the solubility limit increase in the presence of grain boundaries. From the literature we find that metals of the 5th group (in our case vanadium) have a higher diffusivity for oxygen than elements of the 4th (in our case zirconium) group, whereas the solubility limit values indicate that metals of the 4th group (Zr) have higher storage capacities for oxygen than those of the 5th group [11]. This can be clearly seen from the results of our measurements, which are presented in **Figure 5**. There are two layers in the zirconium-rich phase, the first one is the oxidized layer, and the second is the diffused layer. On the other hand, in the Laves phase there is only the diffused layer. The appearance of the oxidized layer in the zirconium-rich phase is the consequence of the affinity of Zr to form chemical bonds with O_2 at elevated temperatures. As a consequence of the composition of ZrO_2, the presence of oxygen in the zirconium-rich phase in mole fractions (%) can be twice that of the zirconium atoms at most, which is evident in **Figure 5a**. By increasing the temperature or time of oxidation, we will observe an increase in the thicknes of the oxidized layer, whereas the structure of diffused layer will remain similar. Thus we have a saturation of the zirconium-rich phase with oxygen in the oxidized layer. On the other hand, in the Laves phase the oxidized layer practically does not exist. Only the diffused layer is present there, which is in accordance with theory [11]. According to theory, the elements of the 5th group have a greater affinity for oxygen diffusion compared to those of the 4th group, whereas the solubility in these elements is quite small.

5 CONCLUSION

According to the results reported in this paper, it can be stated that:

- The XRD together with EDS and AES confirms that the as-received alloy is biphasic.
- The hexagonal zirconium and cubic Laves phases coexist in this material.
- The presence of oxygen in the oxidized specimens is more observable in the zirconium than in the Laves phase, whereas in the as-received specimen, the presence of oxygen is almost the same in both phases.
- XRD analysis of the sample oxidised at 450 °C showed a decrease in the intensity of the Laves phase reflections and the formation of ZrO_2 was indicated.
- With AES depth profiling it is possible to determine the size of the zones affected by the oxygen. The presence of the oxide layer composed of the ZrO_2. was confirmed on the Zr phase.

Acknowledgement

The presented work was partly financed by the European Union, the European Social Fund. Operation implemented in the framework of Operational Program for Human Resources Development for the period 2007-2013, Priority axis1: Promoting entrepreneurships and adaptability, Main type of activity 1.1.: Experts and Researcher for competitive enterprises.

6 REFERENCES

[1] Lafferty J., Foundations of Vacuum Science and Technology, John Wiley & Sons, New York (1998)

[2] Gunter M., et al., Microstructure and bulk reactivity of nonevaporable gettter $Zr_{57}V_{36}Fe_7$, J. Vac. Sci. Technol. A, 16 (**1998**) 6, 3526–3535

[3] Prodromides A., Scheuerlein, Taborelli M., The characterization of non-evaporable getters by Auger electron spectroscopy: analytical potential and artefacts, Applied Surface Science, 191 (**2002**), 300–312

[4] Prodromides A., Scheuerlein, Taborelli M., Lowering the activation temperature of TiZrV non-evaporable getter films, Vacuum 60 (**2001**), 35–41

[5] Jousten K., Handbook of Vacuum Technology, Wiley-WCH Verlag GmbH & Co. KgaA, Weinheim (2008)

[6] Malyshev O., Middleman K., Activation and measurements of nonevaporable getter films, J.Vac. Sci. Technol. A, 27 (**2009**) 2, 321–327

[7] Vedel I., Schlapbach L., Surface reactivity of ZrVFe getter alloys exposed to H_2O, CO and O_2 at 300 K and 700 K, J. Vac. Sci. Technol. A, 11(1993) 3, 539–542

[8] Roupcova P., Schneeweiss O., Changes in phase composition of Zr-Fe-V getter after hydriding and vacuum dehydriding cycles, Journal of Alloys and Compounds, 492 (**2010**), 160–165

[9] Knize R., Cecchi J., Theory of bulk gettering, J. Appl. Phys., 54 (**1983**) 6, 3183–3189

[10] Boffito C., Ferrario B., Della Porta P., Rosai L., A nonevaporbale low temperature activatable getter material, J. Vac. Sci. Technol., 18 (**1981**) 3, 1117–1120

[11] A. Prodromides, Non-Evaporbale Getter Thin Film Coatings for Vacuum Applications, Ecole Polytechnique Federale de Lausanne, PhD thesis, (**2002**), 16–32

[12] B. Ferrario, Chemical pumping in vacuum technology, Vacuum, 47(**1996**) 4, 363–370

[13] C. Schuman, E. Lenarduzzi, S. Weber, M.J. Philippe, D. Petelot, P. Bounie, Modelling the oxygen diffusion profile in TA3V and T40 during heat-treatment under air between 620 and 850 °C, Surface and Coating Technology, 200 (**2006**), 4572–4578

[14] Flinn B., Zhang C., Norton P., Oxygen diffusion along the [0001] axis in Zr(0001), Physical review B, 27 (**1993**) 4, 16499–16505

[15] J. D. Fast, Gases in Metals, The Macmillan Press Ltd. (1976), 127

UDK 543.428.2:519.68
Original scientific article/Izvirni znanstveni članek

ISSN 1580-2949
MTAEC9, 45(1)39(2011)

THE MODELING OF AUGER SPECTRA

MODELIRANJE AUGERJEVIH SPEKTROV

Besnik Poniku, Igor Belič, Monika Jenko

Institute of Metals and Technology, Lepi pot 11, 1000 Ljubljana, Slovenia
besnik.poniku@imt.si

Prejem rokopisa – received: 2010-12-10; sprejem za objavo – accepted for publication: 2011-01-11

The presented work deals with the process of simulated AES spectra creation. The purpose of virtual spectra creation is to use them as a testing ground for different background-removal and noise-reduction algorithms. Numerous methods for background removal and noise reduction exist already, but there is uncertainty about their performance and the accuracy of the data produced, since it is well known that the raw data is altered any time it undergoes any kind of processing conducted for different purposes. This is due to the fact that the levels of background and noise are at unknown levels in the measured AES spectra. By using simulated spectra the case is different. The levels of background and noise are added by the user, thus their levels are known exactly prior to processing. For this reason, they make a valuable means for assessing the performance of different algorithms intended for background removal and noise reduction.
The article describes the principles of simulation of AES spectra and shows the basic elements of the developed software.

Keywords: AES spectra, data processing, simulation, neural networks, VBA

Predstavljeno delo obravnava proces simulacije Augerjevih spektrov. Osnovni namen generiranja virtualnih spektrov je vzpostavitev okolja, namenjenega preizkušanju različnih algoritmov za odstranjevanje spektralnega ozadja in šuma. Obstaja veliko splošnih metod za odstranjevanje ozadja in šuma, ki pa so bile narejene za druge namene, zato njihov vpliv na interpretacijo sestavin spektra ni znan. Znano je, da vsaka metoda, ki odstranjuje ozadje in šum, neizogibno popači tudi osnovno informacijo. Do sedaj je bilo nemogoče zanesljivo oceniti napake, ki jih povzročajo posamezni algoritmi, ker so bili vedno uporabljeni na merjenih spektrih, za katere ni točno znano, kako so sestavljeni, prav tako tudi ne vemo, kakšno je ozadje in koliko je zares šuma. Pri simuliranih spektrih pa v vsakem primeru posebej natančno vemo, kako so sestavljeni, zato je ocena delovanja metod za odstranjevanje neželenih delov spektra lahko zelo zanesljiva.
Članek opisuje postopke simulacije Augerjevih spektrov in prikazuje osnovne gradnike razvitega programskega orodja.

Ključne besede: Augerjevi spektri, obdelava podatkov, simulacija, nevronski sistemi, VBA

1 INTRODUCTION

The main goal of our work was to design a system which will be able to generate a series of AES (Auger Electron Spectroscopy) spectra with one clear aim – to provide an environment where numerous algorithms for AES spectra analysis can be verified, compared and tested. In order to achieve this goal, we have analyzed the appearance of many measured spectra. The article describes the way the AES spectra were analyzed and finally how the different elements were brought together to produce the artificial AES spectra.

1.1 A brief description of AES

Auger electron spectroscopy is a powerful analytical technique for studying surfaces.[1] AES is a very surface-sensitive technique due to the fact that most of the signal comes from the topmost atomic layers of the surface of the sample.[2] Together with X-ray photo-electron spectroscopy (XPS), it has been extensively used for determining the chemical compositions of thin films of nanometer thicknesses in a large variety of applications.[3] This technique is based on the Auger effect, a phenomenon discovered by both Pierre Auger and Lise Meitner independently in the 1920s, even though Pierre Auger is accredited with the discovery in the scientific community.[4] The Auger effect constitutes the emission of an electron from an atom following the filling of a vacancy in an inner electron shell.[5] Even though the discovery of the phenomenon was made in the early 1920s, it was not until the 1950s that AES became a practical characterization technique for analyzing surface features.[6]

AES involves probing the surface with an electron beam, creating excited states of atoms present in the sample[7] through core-shell ionization, and emitting "Auger electrons" with characteristic energies,[8] which are used to determine the surface chemical composition.[9] Afterwards, these electrons enter the analyzer, where depending on the type of the analyzer used they get deflected to degrees which depend on their kinetic energies, and then electrons with different kinetic energies enter the detector at different locations. With the detector the number of electrons reaching specific locations is measured. At the end of the process we obtain the data plotted on the screen as the number of electrons per second reaching the detector versus their kinetic energy. A simplified diagram of this whole process is represented in **Figure 1**.

After obtaining the spectrum the data needs to be processed in order to derive from it the necessary information. Different tools (programs) are used for processing the AES spectra. During these operations

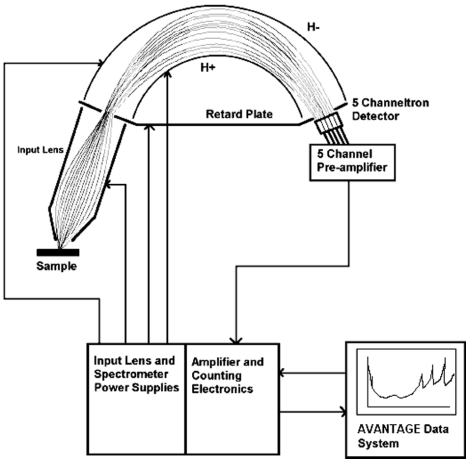

Figure 1: Detection process in Auger Electron Spectroscopy[10]
Slika 1: Proces detekcije pri Augerjevi elektronski spektroskopiji[10]

though, e.g., differentiation of the spectra for quantification, inevitably the raw data is being altered, often at unknown levels to the user. It is important to have information about the influence the program itself has on the data during the processing. In this way the post-processing features observed on the spectra that are not representative of the material, but are due to the influence of the program, will be readily accounted for.

When the spectra are measured, the peaks and noise are superimposed on a slowly varying background.[11] For different purposes, such as the automation of the recognition of AES spectra, data processing like background subtraction and noise reduction is obligatory. Alongside noise, the background is usually regarded as a problem of data processing.[12] In the process of background subtraction and noise reduction through different tools, the spectra are being altered, often at unknown levels to the experimenter.

This work is going to deal with the process of modeling the AES spectra, with the intention of creating simulated spectra to be used later for assessing the performance of the background-removal and noise-reduction algorithms. The advantage of using simulated AES spectra lies in the fact that the levels of background and noise are added by the user, and thus are known prior to the spectra processing. Having prior knowledge about the levels of these two elements of the spectra is a clear advantage, because after processing them through the algorithms for background removal and noise reduction, by comparison the influence the program itself has on the data during the processing can be determined. By taking into account this fact and correcting for it, the uncertainty in the outgoing data will be reduced.

2 EXPERIMENTAL PART

The modeling of the AES spectra involved the careful investigation of numerous real spectra measured from metallic samples. **Figure 2** represents some typical examples of the measured spectra.

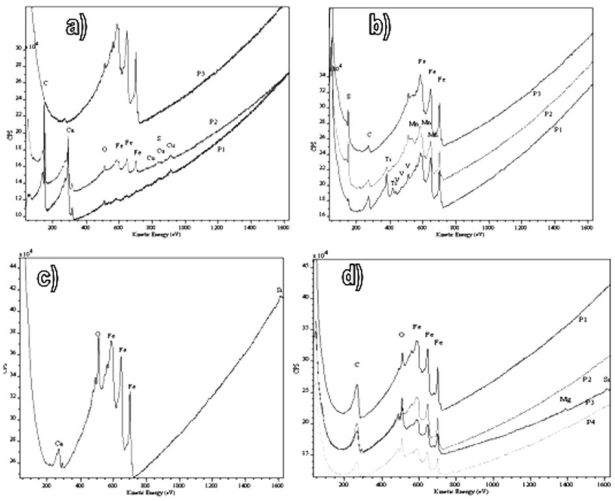

Figure 2: The "Direct" AES spectra used for the determination of the shape of the spectra
Slika 2: Nekaj primerov Augerjevih spektrov, ki so bili uporabljeni za določevanje posameznih sestavnih delov spektra

The spectra were taken using the Microlab 310-F spectrometer at the IMT laboratory for surface analysis.

2.1 Approximation of the background

For the purpose of defining the general shape properties of the background, the data were transferred in a digital form from the standard .vms files of CasaXPS into Excel. **Figure 3** represents the digital data already transferred into an Excel file, with the graph of the spectra being drawn from the imported data.

There the number of points representative of the background were taken, and using the graphing tools in Excel the approximate background for a couple of spectra were drawn. **Figure 4** represents such a case.

Those background shapes for a couple of spectra, in the normalized form, were plotted together in order to investigate and possibly reach some conclusions about their shapes. **Figure 5** represents the manually defined background shapes for a number of spectra.

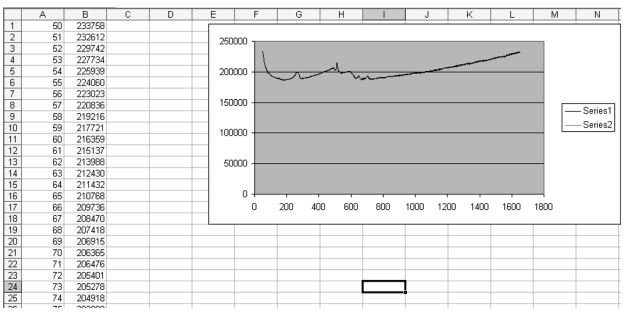

Figure 3: Spectra in digital form transferred from a .vms file and the corresponding graph in Excel
Slika 3: Digitalni zapis spektra, prenesenega z datoteke .vms, ter pripadajoč graf v Excelu

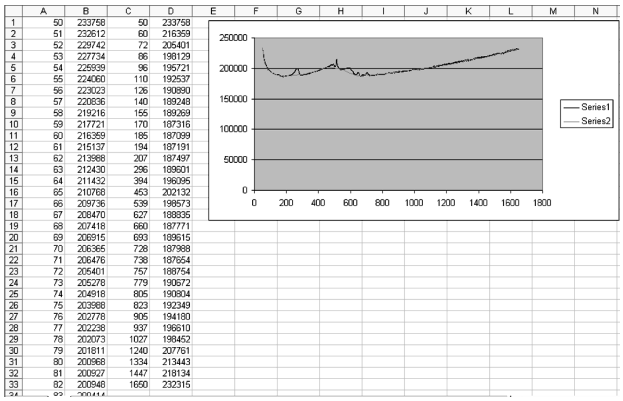

Figure 4: Manually defined background for one spectrum
Slika 4: Ročno določevanje ozadja spektra

From **Figure 5** it is obvious that the AES spectra background is very much variant. Nevertheless, some distinctive features can be observed there, like the "low-energy part" – the descending part where the background shows a rapid decrease in the signal with the kinetic energy increase; the "mid-energy part" – the central part where the increase of the background is observed, which is again followed by the decrease; and the "high-energy part" – the raising part where the background is steadily increasing.

The manual background definition is a very time-consuming process, as much as it is not very reliable.

2.2 Neural network system for background AES approximation

In order to produce a more reliable impression of the background, where a larger amount of AES spectra can be checked with regard to the shape of the background, we have developed a method capable of approximating the background shape. For this purpose, a feedforward neural network was used.

For our purposes, we have used the neural networks for data modeling or function approximation. Neural networks are model-less approximators, meaning they are capable of accomplishing the approximation tasks regardless of any knowledge of the nature of the modeled

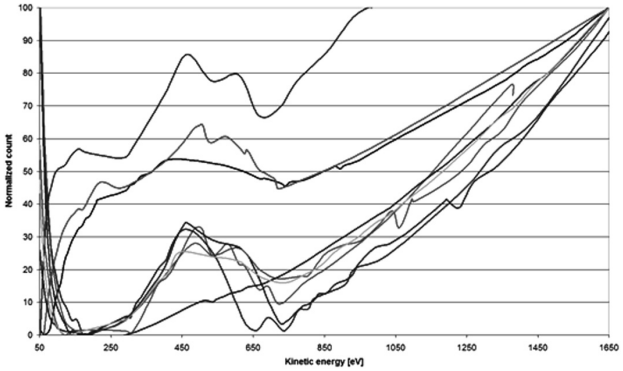

Figure 5: Manually defined background in normalized form
Slika 5: Ročno določeno ozadje v normirani obliki

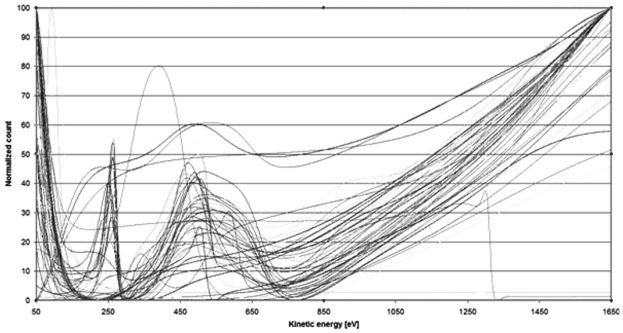

Figure 6: The curves of AES spectra backgrounds for various measured spectra as approximated by the neural network.
Slika 6: Krivulje ocenjenih ozadij za Augerjeve spektre. Ozadje je bilo ocenjeno z nevronskim sistemom.

system. For classical approximation techniques, it is often necessary to know the basic mathematical model of the approximated problem.

The most important property of neural networks is their ability to learn the model from the data presented. This means that the user needs only to be sure that a causal relation between the presented parameters really exists. Almost no further knowledge of the system behavior is needed. When the neural network builds the model, the dependences among the parameters are included in the model.

For implementing the neural networks we used the Neuralyst (Cheshire Ltd.), which is a supplement to Microsoft Excel and VBA (Visual Basic for Accessories), to be able to make the best use of Neuralyst.

The backgrounds for 63 measured AES spectra were approximated using an error backpropagation neural network[13,14]. Since the cumulative AES spectra count values differ in magnitudes significantly, and we have been interested in the comparison of the shape of the spectra, all the samples were normalized prior to the approximation by the neural network. **Figure 6** represents the outcome of the neural network formation of the background for all 63 measured spectra.

From **Figure 6** we can see the same characteristics as was the case with the method where the background was determined manually (**Figure 5**).

2.3 Modeling the background shape

After obtaining a general visual impression for the shape of the backgrounds of the spectra and investigating them, we went to the next level of finding a representative function that would best fit that shape, and the function of which would be used later to simulate the background.

According to the characteristics observed in **Figures 5 and 6** the ideal function for the AES spectra background was proposed to be:

$$f_{\mathrm{B}} = A\left(\frac{1}{px_{\mathrm{e}}} + bx_{\mathrm{e}} + c\right) + B \qquad (1)$$

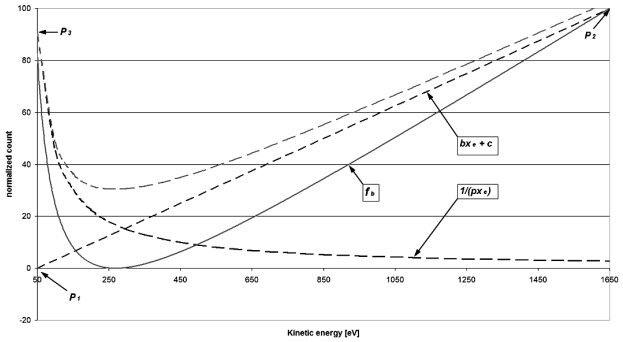

Figure 7: The construction of the background function
Slika 7: Konstrukcija funkcije, ki opisuje ozadje spektra

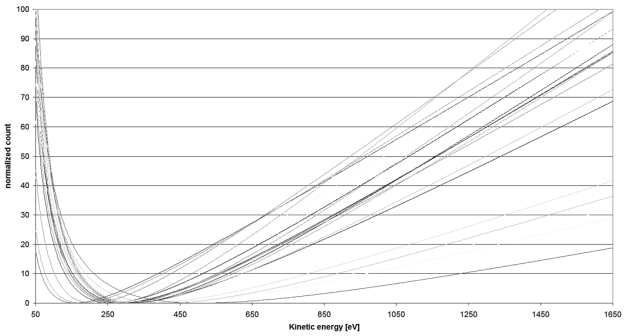

Figure 8: The randomly chosen backgrounds for the simulated AES spectra
Slika 8: Naključno izbrana ozadja za simulirane Augerjeve spektre

Where:
f_B: represents the background function
x_e: the kinetic energy
A, B, p, b, c: parameters which define the shape of the background

The construction of the background function is shown in **Figure 7**.

The construction of the randomly shaped background function starts with the random selection of the parameters of the linear part

$$f_{\text{lin}} = bx_{\text{e}} + c \tag{2}$$

where the points $\mathbf{P_1}$ and $\mathbf{P_2}$ (**Figure 7**) are randomly selected. The point $\mathbf{P_1}$ is the zero crossing of the linear part, and $\mathbf{P_2}$ is the value of the normalized count for the kinetic energy of 1650 eV. The random generator generates the values for $\mathbf{P_1}$ in the range [0, 1000], and $\mathbf{P_2}$ in the range [60, 140]. The limits for both values were defined experimentally, by observing the behavior of real spectra.

From the known points $\mathbf{P_1}$ and $\mathbf{P_2}$ the coefficients $\boldsymbol{b}$ and $\boldsymbol{c}$ of the linear part are defined.

$$\begin{gathered} y = bx_{\text{e}} + c \\ b = \frac{P_{2y}}{P_{2x} - P_{1x}};\ P_{2y} = 1650\ ;\ P_{1y} = 0 \\ c = -bP_{1x} \end{gathered} \tag{3}$$

Then follows the definition of the non-linear part

$$f_{\text{nlin}} = \frac{1}{px_{\text{e}}} \tag{4}$$

For this part the random generator generates the value of the non-linear part for the kinetic energy of 50 eV. In figure 8 this point is denoted by $\mathbf{P_3}$. The random generator selects the values from the interval [20, 500]. Again the border values were taken experimentally. Finally the value for the parameter $\boldsymbol{p}$ is set.

$$P = \frac{1}{P_{3x} \cdot P_{3y}} \tag{5}$$

Parameters A and B are set in the scaling process, where the minimal part of the background function is set close to 0, and the maximal part close to 100.

By using equation 1 as a model function and having the computer randomly generate the necessary parameters within the previously set limiting values, some simulated primary background shapes were obtained. **Figure 8** represents a number of the simulated shapes of the primary background.

2.4 Completing the simulation

To complete the simulation we also had to gather information about the characteristic peaks of elements. For that purpose the characteristic elemental AES spectra of Al, C, Co, Cu, Fe, Au, Ni, O, Si, Ag, Ti, and Va were gathered from Compro10, a database easily accessible on the net.

Generally, we suppose that the measured spectra are constructed according to equation 6.

$$S = f_i(a_i s_i) + P_{\text{B}} + N \tag{6}$$

where S represents the measured AES spectra, f_i is some non-linear function binding the standardized spectra into the composed elements of the spectra, a_i is the amount of i-th element in the spectra, s_i the i-th pure element represented in the AES spectra, P_B is the primary background, and N is the noise.

In the case of synthesis of the artificial AES spectra, the non-linear dependence of the various standardized spectra is assumed to be linear, thus producing equation 7.

$$S = \sum_{i=1}^{M} (a_i s_i) + P_{\text{B}} + N \tag{7}$$

where the symbol M denotes the number of all the spectra in the database.

For the purpose of creating the so-called standard spectra database, the elementary spectra were analyzed. **Figure 9** shows the spectra of pure Fe.

From visually inspecting **Figure 9** we can see that the AES spectra consist of the three distinctive elements:
1. The primary background,
2. The peaks base,
3. The peaks.

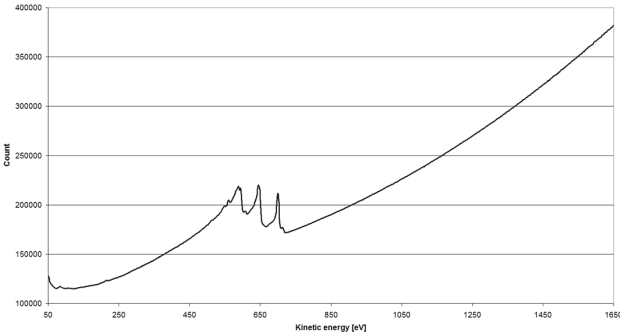

Figure 9: The AES spectrum of Fe
Slika 9: Augerjev spekter Fe

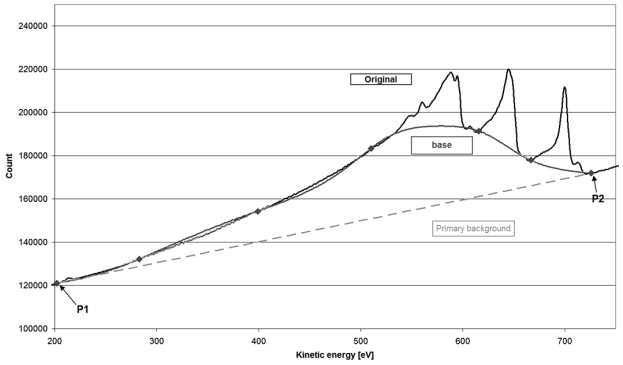

Figure 10: The AES spectra elements
Slika 10: Elementi Augerjevega spektra

Figure 10 illustrates these distinctive parts. For the purpose of extraction of the three spectra elements, several steps were introduced as follows:

1. Two points $\mathbf{P_1}$ and $\mathbf{P_2}$ (**Figure 10**) were selected. They are common to all three curves.
2. The line that represents the primary background through $\mathbf{P_1}$ and $\mathbf{P_2}$ was constructed. We are aware that in the measured spectra the primary background is nowhere linear, but the use of the line is close enough for the intended purpose.
3. On the part of the AES spectra between $\mathbf{P_1}$ and $\mathbf{P_2}$ the set of points describing the base of the peaks was selected (**Figure 10**). Typically, the number of selected points was up to 10.

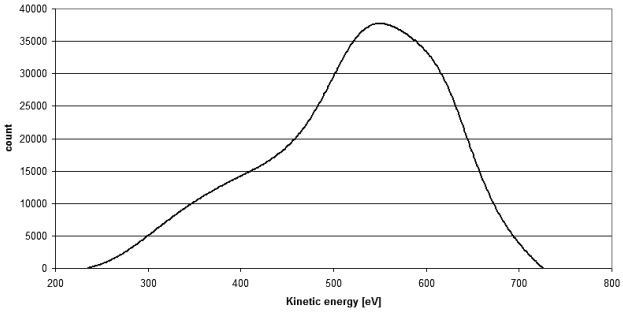

Figure 11: The approximated function of the base of the peaks for the Fe AES spectrum
Slika 11: Aproksimirana funkcija podlage vrhov za Augerjev spekter Fe

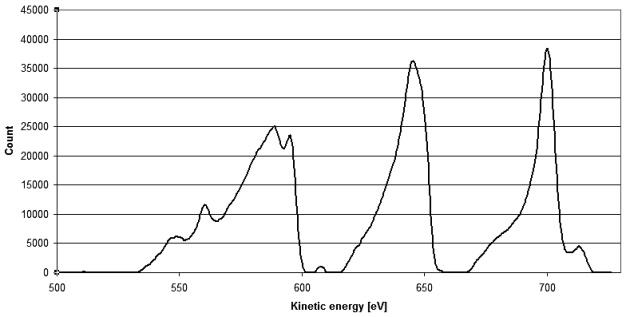

Figure 12: The extracted peaks of Fe AES spectra
Slika 12: Izločeni vrhovi za Augerjev spekter Fe

The shape of the base function was approximated by the four-layer neural network (configuration 1-4-8-1). The approximated function was stored in a table containing the Kinetic energy and count values for the area between $\mathbf{P_1}$ and $\mathbf{P_2}$ (**Figure 11**).

4. Once the base function is known it is subtracted from the original spectra, thus obtaining the shape of the extracted peaks (**Figure 12**).

2.5 The virtual AES spectra generator

The system for the random generation of AES spectra was developed under Microsoft Excel using Visual Basic for Applications and consists of six distinctive elements:

1. The generator Console
2. The Files control center
3. The Primary background generator
4. The Noise generator
5. The standard elements peaks database
6. The standard elements peak base database.

2.5.1 The generator Console

The generator console is the central part of the AES spectra generator. It provides the basic constituent data regarding the generated AES spectra. The following are data provided on the Console datasheet:

- The generator mode of operation. Two modes are currently possible: "ONE AES" producing only one randomly generated AES spectra without the saving to the file; "SAVE TO FILE" option, which generates random AES spectra and stores the data to the files.
- The number of elements provided in the standard spectra database. Currently, the standard spectra database contains 11 spectra of standard elements. Additional spectra are very easily included in the database.
- The number of actual AES spectra constituents. Although the number of standard spectra is provided, the process of random AES spectra generation can be limited to the lower number of actual constituents. The number is specified by the user.
- The graphical representation of the randomly generated spectra. The generated spectra are joined with

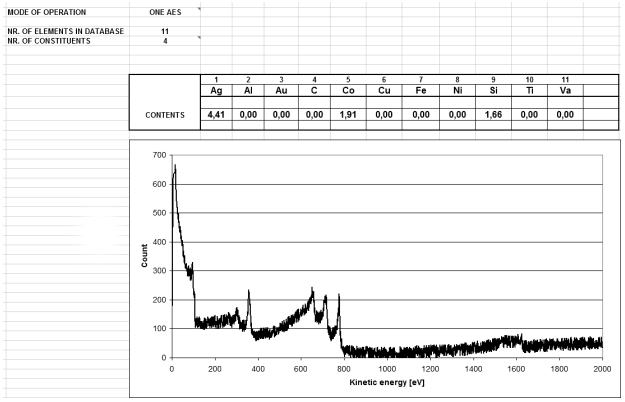

Figure 13: The AES spectra generator main console
Slika 13: Osrednji del generatorja Augerjevih spektrov

the primary background as well as with the noise. The result of the multiple random generation is graphically presented. The additional information is provided on the table where the amounts of the constituents are given (**Figure 13**).

2.5.2 The Files control center

The Files control center defines the way in which the randomly generated AES spectra are stored. The user defines the name of the files where the spectra are to be stored. The provided name is joined by the subsequent number of the generated spectra and stored in the directory, the name of which has already been provided by the user. It is also necessary to specify the number of generated AES spectra that are to be saved in the separate file.

The data contained in each file are:

- The sum of all the peaks contained in the generated AES spectra
- The sum of all the base elements that are part of each standard spectra
- The randomly generated primary background
- The noise
- The AES spectra construction data

2.5.3 The Primary background generator

The primary background generator controls the process of AES spectra primary background generation. The user must define the intervals for the primary background parameters. The AES spectra generator uses the given intervals to randomly re-shape the basic primary background equation. **Figure 14** represents the graphical user interface for the AES spectra primary background generation.

2.5.4 The Noise generator

The noise generator provides the random noise that is to be added to the AES spectra. The user can define the upper limit for the AES spectra noise. The noise

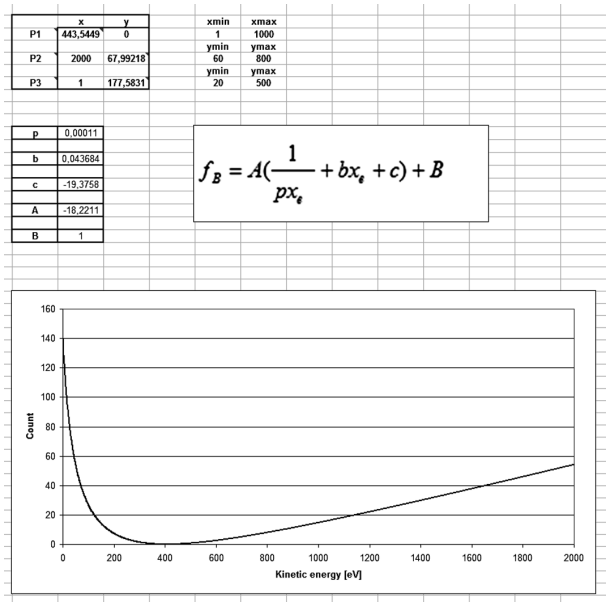

Figure 14: The AES spectra primary background generation
Slika 14: Generiranje osnovnega ozadja Augerjevega spektra

generator then forms the noise according to the given boundary. The generated noise is bipolar, providing that the AES spectra fluctuations affect the spectra both as the addition and subtraction to the signal (**Figure 15**). In the literature, the noise level is understood to be in a non-linear dependence with the kinetic energy. In the first stage of the AES signal modeling we opted to use the linear dependence of the noise amplitude over the kinetic energies used.[15]

2.5.5 The standard-elements peaks database

The standard-elements peaks database contains the data on the pure – standard – elements that are the basis of the AES spectra generation. So far, 11 elements have been added to the database. This database contains only the peaks data (**Figure 16**). Other parts are stored elsewhere.

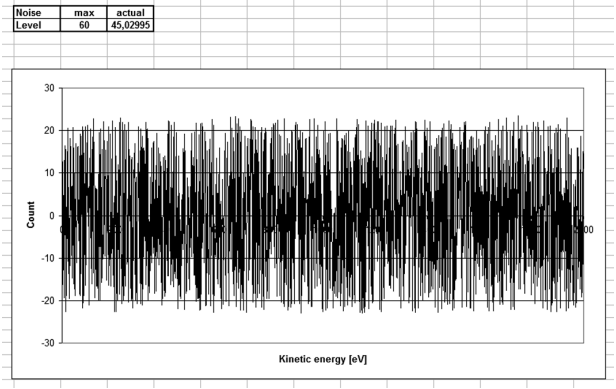

Figure 15: The AES spectra noise
Slika 15: Dodan šum Augerjevemu spektru

1	kinetic energy	1	2	3	4	5	6	7	8	9	10	11
2	eV	Ag	Al	Au	C	Co	Cu	Fe	Ni	Si	Ti	Va
3	1	1,458843405	0	7,235415428	0	0	0	0	0	18,66672	0	0
4	2	13,05296682	0	27,75620573	0	0	0	0	0	36,03436	0	0
5	3	35,48330814	0	41,54103022	0	0	0	0	0	54,8241	0	0
6	4	58,46859806	0	47,53857699	0	0	0	0	0	57,28049	0	0
7	5	76,71293879	0	54,25447137	0	0	0	0	0	57,29505	0	0
8	6	89,29555989	0	59,53721244	0	0	0	0	0	58,0645	0	0
9	7	96,61959806	0	64,71527927	0	0	0	0	0	59,73892	0	0
10	8	99,47087319	0	69,15421532	0	0	0	0	0	60,40827	0	0
11	9	98,74896727	0	71,94161693	0	0	0	0	0	59,88531	0	0
12	10	95,70511617	0	74,92995569	0	0	0	0	0	58,55592	0	0
13	11	91,79740617	0	79,02207872	0	0	0	0	0	56,70751	0	0
14	12	88,2460202	0	81,66399413	0	0	0	0	0	53,71709	0	0
15	13	85,36093567	0	83,16791941	0	0	0	0	0	49,76669	0	0
16	14	83,46246275	0	85,68449827	0	0	0	0	0	45,53661	0	0
17	15	82,46752056	0	89,17851854	0	0	0	0	0	41,25068	0	0
18	16	81,69311916	0	91,44918029	0	0	0	0	0	37,18716	0	0
19	17	80,43557563	0	92,35993849	0	0	0	0	0	33,58462	0	0
20	18	78,70487734	0	92,83098686	0	0	0	0	0	30,51096	0	0
21	19	77,12126287	0	93,42641841	0	0	0	0	0	27,83945	0	0
22	20	75,74640215	27,8054921	93,86783997	0	0	0	0	0	25,42721	44,80378	66,75417
23	21	74,6213415	26,12997675	93,83923199	0	0	0	0	0	23,29018	49,32057	66,32416
24	22	73,71469132	25,34905323	93,93946216	0	0	0	0	0	21,33561	51,65256	65,56686
25	23	72,9640523	24,73814092	94,02046234	0	0	0	0	0	19,61832	54,48296	64,44257
26	24	72,43115629	24,41516886	93,73441915	0	0	0	0	0	18,28778	58,49928	62,61042
27	25	71,92951852	24,49805434	92,81171391	0	0	0	0	0	17,14695	60,5726	58,75256
28	26	71,18993246	24,73523148	91,81367054	0	0	0	0	0	16,24494	55,50723	54,08659
29	27	70,2328273	25,26689923	90,90211325	0	0	0	0	0	15,53258	37,43392	49,57564
30	28	68,95454874	25,94502211	89,95807279	0	0	0	0	0	14,98766	15,73928	46,69808
31	29	67,59280517	26,88024767	88,97263855	0	0	0	0	0	14,74438	6,549249	44,74163
32	30	66,04402769	27,55508533	88,0614388	0	0	0	0	0	14,63863	2,698981	40,66067
33	31	64,46327704	28,28727126	87,16354756	0	0	0	0	0	14,68496	0,715552	31,56831
34	32	62,98498525	29,2024048	86,28757821	0	0	0	0	0	14,97334	0,081542	17,77097
35	33	61,61953012	29,90135524	85,65934112	0	0	0	0	0	15,31742	0,015882	7,780719
36	34	60,35667178	30,70203676	85,28467722	0	0	0	0	0	15,74066	0	3,201487
37	35	59,26898855	31,36806067	85,19555086	0	0	0	0	0	16,20544	0	0,840073
38	36	58,2326169	32,83084564	85,16632658	0	0	0	0	0	16,55251	0	0
39	37	57,18583253	34,01159817	85,19147464	0	0	0	0	0	17,03891	0	0
40	38	56,02562137	35,339304	85,03103188	0	0	0	0	0	17,6038	0	0,41539
41	39	54,71111167	36,6812686	84,60145118	0	0	0	0	0	18,23121	0	0,857178
42	40	53,24288739	37,72011431	83,61949681	0	0	0	0	0	18,98108	0	1,427221
43	41	51,77676068	37,48977417	82,07706238	0	0	0	0	0	19,83697	0	1,622147

Figure 16: The standard-elements peaks database
Slika 16: Podatkovna baza standardnih spektrov

2.5.6 The standard-elements peaks base database.

The standard-elements peaks base database is formatted in exactly the same way as in the case of the standard-elements peaks database.

3 RESULTS AND DISCUSSION

Comparing **Figure 17** with **Figure 2** it is obvious that the randomly simulated AES spectra adequately resemble the measured AES spectra. The variations of the backgrounds are sufficient to produce a set of quite different spectra that will allow a thorough analysis of the background- and noise-removal algorithms.

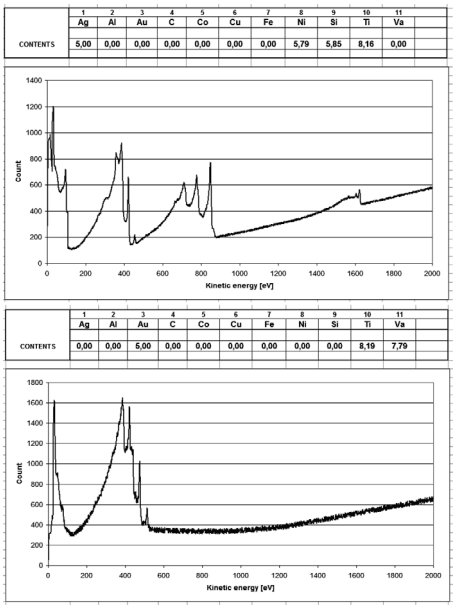

Figure 17: Two cases of simulated AES spectra with their corresponding data
Slika 17: Primera simuliranega Augerjevega spektra

The process of construction of the complete AES spectra starts with the selection of the parameters that control the process. The steps are the following:

1.) The number of constituent elements that are to be joined in the spectra is selected by the user. In our case the user can select 12 different elements. This number can be easily changed by adding the new spectra for additional elements.
2.) The random generator selects the constituent elements (from the number provided by the user in the previous step) and sets the relative amplitude for each selected element (parameter a_i from equation 6).
3.) The primary background is created.
4.) One by one the spectra of the selected elements are added to the primary background.
5.) The randomly generated noise is added.
6.) The normalized form of the simulated spectra is scaled to receive the "realistic" count values.
7.) The created spectrum is stored in a separate file, which will later represent the testing and validation ground for different background- and noise-removal techniques and algorithms. Each file contains detailed data on how the concrete spectra were constructed, so the background and the noise are known in detail. Therefore, a very exact basis for the further analysis is set.

Figure 17 represents two cases of simulated AES spectra, with the corresponding data given alongside in the table.

It is very important to note that the simulated AES spectra do not necessarily have to represent the spectra of real materials. The only condition that has to be fulfilled is for them to resemble the real AES spectra, i.e., to consist of the same constituent parts.

4 CONCLUSIONS

AES is a technique capable of deriving information from the topmost atomic layers of the surface. It is able to identify a very wide range of elements present at solid surfaces, and sometimes it can be used to obtain information about the chemical environment and bonding of surface species.[16] As knowledge about the properties of surfaces and their composition is increasing in importance, so is the need to get accurate information about them through techniques such as AES. An inevitable step after performing a measurement with this technique is the data processing that follows in order to harvest the desired information out of the spectra already taken. Background and noise are two undesired elements that are present alongside the characteristic peaks of elements in measured AES spectra. The background must be removed and the noise reduced to continue with the proper treatment of the data, but being at unknown levels in the raw data and knowing that any data treatment inevitably alters them to some extent, there is uncertainty as to the quality of the outgoing information.

The highlight of this work is the ability to have prior knowledge about the levels of background and noise before the processing of the spectra by various means takes place. Having this in mind, after the processing is done the pre-processed and the post-processed data can be compared to learn how much error the background-subtraction and noise-reduction techniques are introducing into the results that we read. By correcting for this factor the accuracy of the obtained information from the background-removal and noise-reduction tools is greatly improved.

It is of utmost importance to know that the presented work serves only one purpose, i.e., to provide the environment where various algorithms for noise reduction and background removal can be tested and evaluated. Such algorithms can afterwards be used on measured spectra, but with a thorough understanding of the consequences they have for the phase of data processing.

5 REFERENCES

[1] F. A. Settle, (editor) Handbook of instrumental techniques for analytical chemistry, Prentice Hall, New Jersey, 1997

[2] C. R. Brundle, C. A. Evans, Jr., S. Wilson, Encyclopedia of Materials Characterization. Manning Publications & Reed Publishing, 1992

[3] C. J. Powella, A. Jablonski, W. S. M. Werner, W. Smekal, Characterization of thin films on the nanometer scale by Auger electron spectroscopy and X-ray photoelectron spectroscopy, Applied Surface Science, 239 (**2005**), 470–480

[4] J. T. Grant, D. Briggs, Surface analysis by Auger and X-ray Photoelectron Spectroscopy, Chichester, IM Publications 2003

[5] IUPAC. Compendium of chemical terminology, 2nd ed. (the "Gold Book"). Compiled by A. D. McNaught and A. Wilkinson. Blackwell Scientific Publications, Oxford 1997

[6] M. Thompson, M. D. Baker, A. Christie, J. F. Tyson, *Auger Electron Spectroscopy,* Chichester: John Wiley & Sons, 1985

[7] G. Gauglitz, T. Vo-Dinh (editors), Handbook of Spectroscopy. WILEY-VCH Verlag GmbH & Co. KGaA, Weinheim 2003

[8] D. Briggs and M. P. Seah (editors), Practical surface analysis, John Willey & Sons, West Sussex 1990

[9] J. A. Venables, Introduction to surface and thin film processes, Cambridge University Press, 2000

[10] Microlab 310-F, Operators Manual, V.G. Scientific, 1997

[11] V. Mazet, C. Carteret, D. Brie, J. Idier, B. Humbert, Background removal from spectra by designing and minimising a non-quadratic cost function, Chemometrics and Intelligent Laboratory Systems, 76 (**2005**) 2, 121–133

[12] J. T. Grant, Background subtraction techniques in surface analysis, J. Vac. Sci. Technol. A, 2 (**1984**), 2

[13] R. M. Golden, Mathematical Methods for Neural Network Analysis. MIT Press, Cambridge MA 1996

[14] I. Belič, Neural networks and modelling in vacuum science, Vacuum. 80 (**2006**), 1107–1122

[15] M. F. Koenig, J. T. Grant, Signal-to-noise measurements in X-ray photoelectron spectroscopy, Surface and Interface Analysis, 7 (**1985**) 5, 217

[16] J. T. Grant, Surface analysis with Auger electron spectroscopy, Applications of Surface Science, 13 (**1982**), 35–62

UDK 621.74:519.68
Original scientific article/Izvirni znanstveni članek

ISSN 1580-2949
MTAEC9, 45(1)47(2011)

MODELLING OF THE DIRECTIONAL SOLIDIFICATION OF A LEADED RED BRASS FLANGE

MODELIRANJE USMERJENEGA STRJEVANJA PRIROBNICE IZ RDEČE SVINČEVE MEDENINE

Vladimir Grozdanić

University of Zagreb, Metallurgical Faculty, Aleja narodnih heroja 3, 44103 Sisak, Croatia

Prejem rokopisa – received: 2010-04-21; sprejem za objavo – accepted for publication: 2010-11-02

A mathematical model and a numerical simulation of the directional solidification of a leaded red brass flange are presented. The mathematical model is based on physically realistic assumptions and it is solved by the finite-difference method, implicit alternating directions method. This method has great accuracy and is of second order with regard to the approximation of time and space. The initial conditions are an analytical solution of the heat conduction equation in the case of the contact of two semi-infinite media. The latent heat of fusion incorporated into the equation for the specific heat capacity of metal, and temperature dependent thermophysical properties of all materials in the system mould–casting–core–chill, enables us to accurately numerically represent the flange solidification, which is casting and a common example in foundry practice. The simulation of the directional solidification is a modern and scientific way of pointing to casting points in which the defect occurrence is possible, and how to prevent them using the chill.

Keywords: mathematical model, directional solidification, leaded red brass flange, graphite chill

Predstavljena sta matematični model in numerična simulacija usmerjenega strjevanja prirobnice iz rdeče svinčeve medenine. Podlaga matematičnega modela so realne fizikalne predpostavke, model pa je razvit z metodo končnih razlik, implicitno metodo z alternativno smerjo. Ta metoda je zelo natančna in je drugega reda glede na približek časa in prostora. Začetni pogoji so analitične rešitve enačbe za toplotno prevodnost za primer kontakta dveh semineskončnih medijev. Latentna talilna toplota, ki je uporabljena za specifično toplotno kapaciteto kovine in termofizikalne lastnosti vseh materialov v sistemu forma – litje – jedro – kokila omogočajo, da se numerično modelira strjevanje prirobnice, torej litje, kar je splošen primer dela v livarni. Simulacija usmerjenega strjevanja je moderna metoda, da se znanstveno opredeli mesta ulitka, kjer lahko nastajajo napake in kako te napake s kokilo preprečiti.

Ključne besede: matematični model, usmerjeno strjevanje, prirobnica, svinčeva rdeča medenina, grafitna kokila

1 INTRODUCTION

The directional solidification of castings of a given geometry may be obtained using risers or chills. Risers are reservoirs of molten metal and feed the casting in the liquid state. In the case of classical risers, only 17 pct. of the initial volume of the riser is available for the feeding of the casting 1. In contrast to risers, chills better lead away the heat and in this way speed up the solidification. Usually, they are used when the placement of risers is impossible. However, in the case of nonferrous metals this is not a rule. In this way, for example, in the investigated system of a leaded red brass flange, directional solidification is obtained using a graphite chill. With the placement of an appropriate chill, the hot spot is shifted in areas of the casting which are later machined. This is desirable because the hot spot solidifies last, and in their place the occurrence of casting defects (e.g., shrinkage cavity, porosity etc.) is possible. The investigated system is complex because it consists of a flange, a mould core and a chill, and it is shown in **Figure 1**. For a given system the mathematical model of the solidification is formulated and investigated.

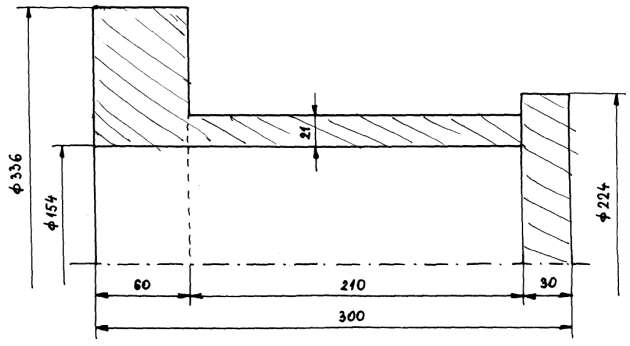

Figure 1: Flange and graphite chill with the corresponding dimensions
Slika 1: Prirobnica in grafitna kokila z dimenzijami

2 MATHEMATICAL MODEL

In the development of the mathematical model, the following partial differential equation of heat flow corresponding to the flange (**Figure 1**) [2] should be solved:

$$\frac{\partial T}{\partial t} = a\left(\frac{\partial^2 T}{\partial r^2} + \frac{1}{r}\frac{\partial T}{\partial r} + \frac{\partial^2 T}{\partial z^2}\right) \quad (1)$$

Since for the horizontal axis of the flange symmetry $r = 0$, equation (1) should be modified according to L' Hospital's rule considering the equation:

$$\frac{\partial T}{\partial t} = a\left(2\frac{\partial^2 T}{\partial r^2} + \frac{\partial^2 T}{\partial z^2}\right) \quad (2)$$

Initial conditions

The mould temperature and the temperature of its outer side are equal to T_s, whereas the temperature of the metal is equal to the casting temperature T_L. The initial temperature at the mould/casting boundary interface can be obtained by solving Fourier's differential equation for heat flow through the contact area of two semi-infinite media:

$$T_i = T_s + \frac{T_L - T_s}{1 + \frac{K_K}{K_m}\sqrt{\frac{a_m}{a_k}}} \quad (3)$$

The derivation of eq. (3) is given in Appendix 2.

Boundary conditions

The outer mould surface maintains a constant temperature T_s. For the contacts mould/metal, metal/core, mould/core, metal/chill, mould/chill and chill/core area there are continuous heat flows for which the boundary condition of the fourth type holds [3]:

$$K_m \frac{\partial T_m}{\partial n} = K_K \frac{\partial T_K}{\partial n} \quad (4)$$

$$K_m \frac{\partial T_m}{\partial n} = K_j \frac{\partial T_j}{\partial n} \quad (5)$$

$$K_m \frac{\partial T_m}{\partial n} = K_h \frac{\partial T_h}{\partial n} \quad (6)$$

$$K_k \frac{\partial T_K}{\partial n} = K_j \frac{\partial T_j}{\partial n} \quad (7)$$

$$K_h \frac{\partial T_h}{\partial n} = K_k \frac{\partial T_k}{\partial n} \quad (8)$$

$$K_h \frac{\partial T_h}{\partial n} = K_j \frac{\partial T_j}{\partial n} \quad (9)$$

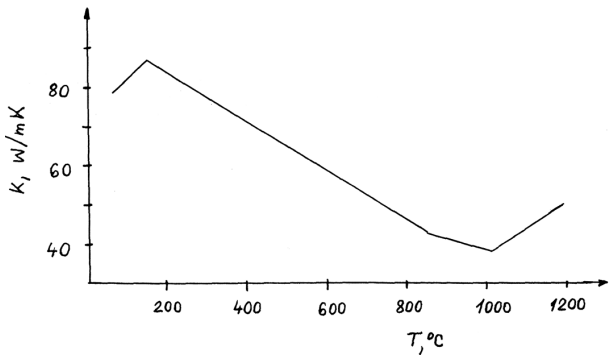

Figure 2: Temperature-dependent thermal conductivity of the leaded red brass flange

Slika 2: Odvisnost toplotne prevodnosti od temperature za prirobnico iz svinčeve rdeče medenine

Thermophysical properties of the material

It has been assumed that the thermal properties of the mould, metal, core and chill are temperature dependent [4], which is as shown in **Figures 2 to 9**.

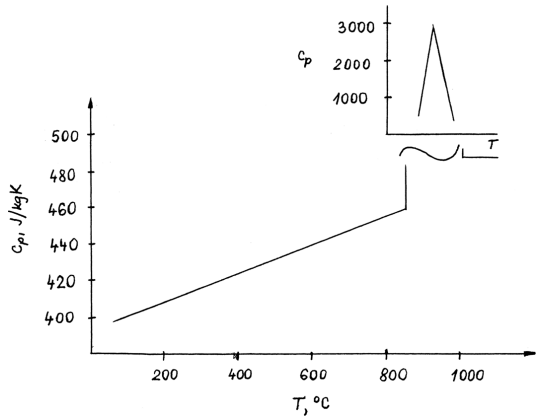

Figure 3: Temperature-dependent specific heat capacity of the leaded red brass flange

Slika 3: Odvisnost specifične toplotne kapacitete od temperature za prirobnico iz svinčeve rdeče medenine

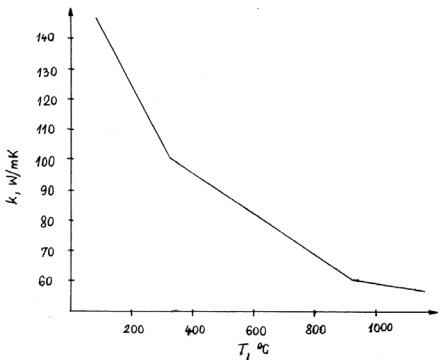

Figure 4: Temperature-dependent thermal conductivity of the graphite chill

Slika 4: Odvisnost toplotne prevodnosti od temperature za grafitno kokilo

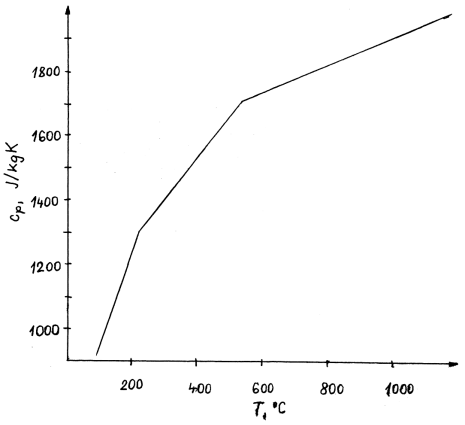

Figure 5: Temperature-dependent specific heat capacity of the graphite chill

Slika 5: Odvisnost specifične toplotne kapacitete od temperature za grafitno kokilo

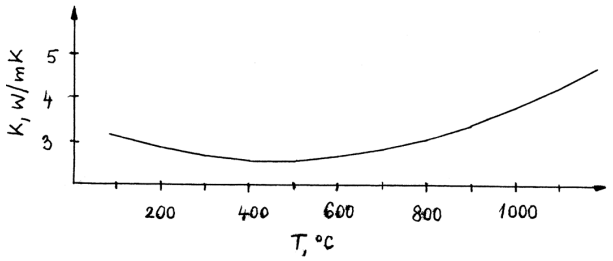

Figure 6: Temperature-dependent thermal conductivity of the mould
Slika 6: Odvisnost toplotne prevodnosti od temperature za formo

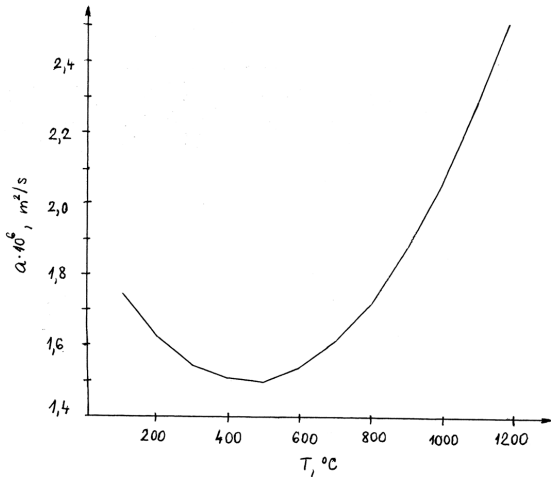

Figure 7: Temperature-dependent temperature diffusivity of the mould
Slika 7: Odvisnost toplotne difuzivnosti od temperature za formo

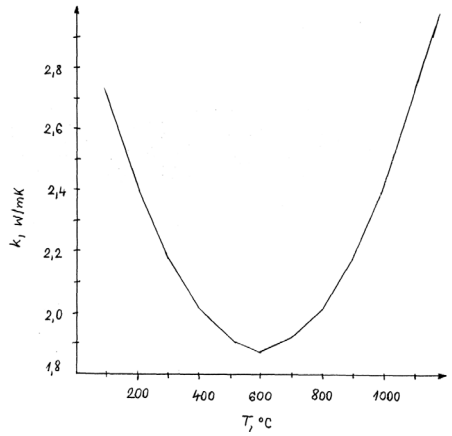

Figure 8: Temperature-dependent thermal conductivity of the core
Slika 8: Odvisnost toplotne prevodnosti od temperature za jedro

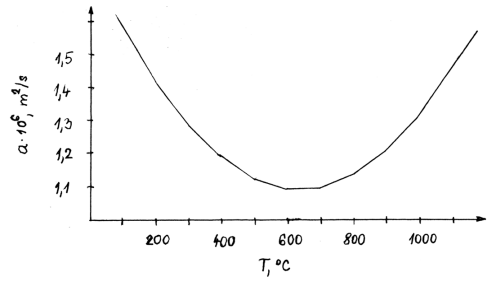

Figure 9: Temperature-dependent temperature diffusivity of the core.
Slika 9: Odvisnost toplotne difuzivnosti od temperature za jedro

3 IMPLICIT ALTERNATING DIRECTION METHOD

Differential heat-flow equations (1) and (2) with the corresponding initial and boundary conditions have been numerically solved using the implicit alternating direction method [5,6]. The method utilises the division of the time interval into two steps.

In the first half of the time interval the equation is solved implicitly for z and explicitly for the *r* direction. The procedure is reversed in the second half of the time interval.

Consequently, for the differential equation (1) and the first half of the time interval $\Delta t/2$ we have:

$$\frac{T^{n}_{i,j-1} - 2T^{n}_{i,j} + T^{n}_{i,j+1}}{(\Delta r)^2} + \frac{T^{n}_{i,j+1} - T^{n}_{i,j-1}}{2r_j \cdot \Delta r} + \frac{T^{n}_{i-1,j} - 2T^{n}_{i,j} + T^{n}_{i+1,j}}{(\Delta z)^2} = \frac{1}{a_{i,j,n}} \frac{T^{*}_{i,j} - T^{n}_{i,j}}{\Delta t/2} \tag{10}$$

Whereas for the second $\Delta t/2$ we obtain:

$$\frac{T^{n+1}_{i,j-1} - 2T^{n+1}_{i,j} + T^{n+1}_{i,j+1}}{(\Delta r)^2} + \frac{T^{n+1}_{i,j+1} - T^{n+1}_{i,j-1}}{2r_j \cdot \Delta r} + \frac{T^{*}_{i-1,j} - 2T^{*}_{i,j} + T^{*}_{i+1,j}}{(\Delta z)^2} = \frac{1}{a_{i,j,n}} \frac{T^{n+1}_{i,j} - T^{*}_{i,j}}{\Delta t/2} \tag{11}$$

The numerical solution for the differential equation (2) of the heat flow for the first $\Delta t/2$ is:

$$4\frac{T^{n}_{i,2} - T^{n}_{i,1}}{(\Delta r)^2} + \frac{T^{*}_{i-1,1} - 2T^{*}_{i,1} + T^{*}_{i+1,1}}{(\Delta z)^2} = \frac{1}{a_{i,1,n}} \frac{T^{*}_{i,1} - T^{n}_{i,1}}{\Delta t/2} \tag{12}$$

and for the second $\Delta t/2$:

$$4\frac{T^{n+1}_{i,2} - T^{n+1}_{i,1}}{(\Delta r)^2} + \frac{T^{*}_{i-1,1} - 2T^{*}_{i,1} + T^{*}_{i+1,1}}{(\Delta z)^2} = \frac{1}{a_{i,1,n}} \frac{T^{n+1}_{i,1} - T^{*}_{i,1}}{\Delta t/2} \tag{13}$$

The use of the implicit alternating direction method results in a system of simultaneous linear algebraic equations with the variables v_1, v_2,…, v_n of tri-diagonal form:

$$\begin{aligned}
&b_1 v_1 + c_1 v_2 = d_1 \\
&a_2 v_1 + b_2 v_2 + c_2 v_3 = d_2 \\
&a_3 v_2 + b_3 v_3 + c_4 v_4 = d_3 \\
&\ldots\ldots\ldots\ldots\ldots\ldots \\
&a_i v_{i-1} + b_i v_i + c_i v_{i+1} = d_i \\
&\ldots\ldots\ldots\ldots\ldots\ldots \\
&a_{N-1} v_{N-2}\, b_{N-1} v_{N-1} + c_{N-1} v_N = d_{N-1} \\
&a_N v_{N-1} + b_N v_N = d_N
\end{aligned} \tag{14}$$

The special efficient algorithm for solving the tri-diagonal system of equations is [7]:

$$v_N = \gamma_N \tag{15}$$

$$v_i = \gamma_i - \frac{c_i v_{i+1}}{\beta_i}, \quad i = n-1, n-2, ..., 1 \tag{16}$$

where β and γ are calculated from recursive formulas

$$\beta_1 = b_1 \tag{17}$$

$$\gamma_1 = d_1/\beta_1 \tag{18}$$

$$\beta_i = b_i - \frac{a_i c_{i-1}}{\beta_{i-1}}, \quad i = 2,3,...,n \tag{19}$$

$$\gamma_i = -\frac{d_i - a_i \gamma_{i-1}}{\beta_i}, \quad i = 2,3,...,n \tag{20}$$

The tri-diagonal coefficients that give the algorithm of the flange solidification in a sand mould are presented in Appendix 3. Based on the presented algorithm a computer program was written in FORTRAN 77 and solved on an Athlon AMD 64 computer.

4 FLOW DIAGRAM

A detailed flow diagram is shown in **Figure 10a** and **10b**.

The main feature of the program is the use of two temperature matrixes, namely T and T^*. The first matrix contains the temperatures at the start and the end of the time step, and the second contains the temperature at the end of first $\Delta t/2$. Initial values are assigned to the program variables and constants. The program module TYP provides for the initial values of the temperatures, of particular net points as well as for the standardization of all the points in the mould, the casting, the chill core and their boundary interfaces. The module PRINT 1 prints out the initial temperature distribution. The system of tri-diagonal equations is then solved firstly, row by row (module ROWS), and then column by column (module COLS). The results are periodically printed over the whole geometry of the casting, the mould, the chill and the core (module PRINT 1) or over the casting geometry only (module PRINT 2) until the prescribed time t_{max}.

5 DISCUSSION

Leaded red brass (alloy C83600) has the following composition: 85 % Cu, 5 % Sn, 5 % Pb and 5 % Zn [8]. The alloy C83600 is used not only for flanges, but also for valves, pipe fittings, water pumps' meter housings and impellers, small gears, high-quality plumbing goods, statuary and plaques. These applications are possible because of its corrosion resistance, machinability, strength, bearing properties, colour and the excellent castability of the alloy.

The simulation of the solidification of the leaded red brass flange in a sand mould is carried out by the space steps Δz = 15 mm and Δr = 7 mm and the time step Δt = 5 s to t_{max} = 600 s.

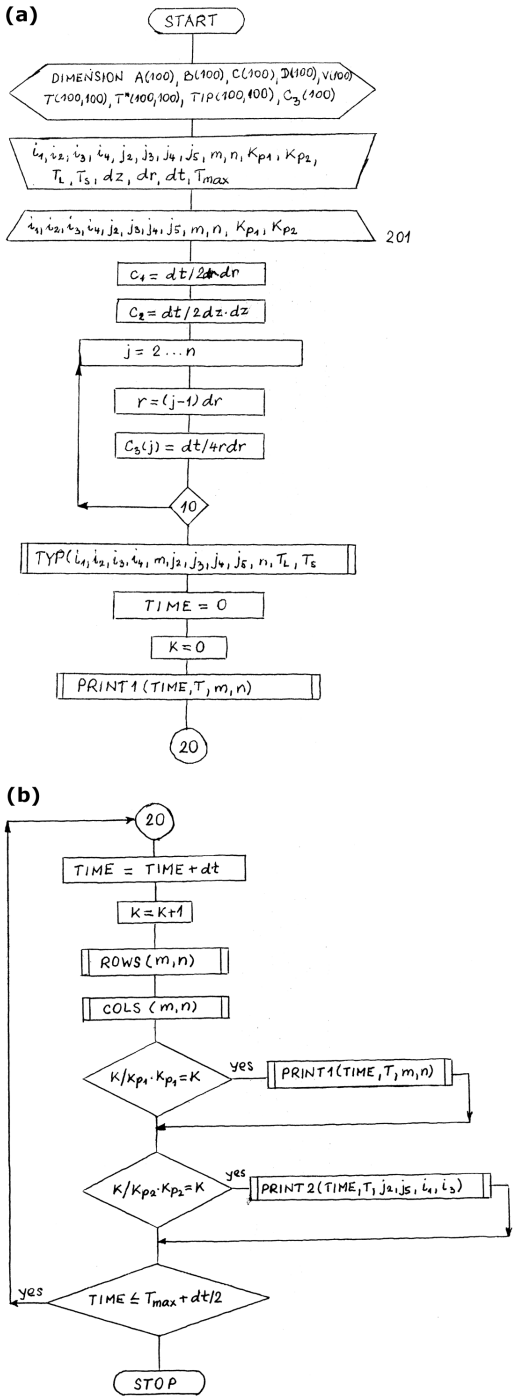

Figure 10: Flow diagram
Slika 10: Flow diagram

The casting temperature was 1180 °C and the initial temperature of the mould, the core and the chill was 25 °C. The initial temperature at the sand/casting interface was 1057 °C, on the casting/core interface it was 1013 °C, and at the casting/chill interface it was 577 °C. On the basis of successive temperature print outs for particular net points, a solidification time of 367 s was obtained.

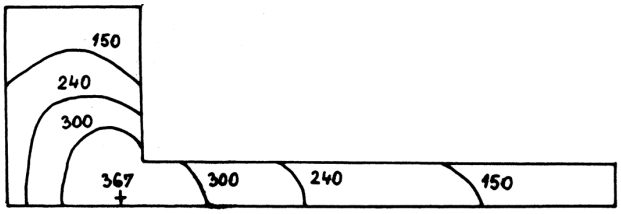

Figure 11: Progress of the isosolidus (854 °C) after (150, 240 and 300) s
Slika 11: Napredovanje izotr. (854 °C) po (150, 240 in 300) s

Using the isosolidus (854 °C) shift, as seen in **Figure 11**, it can be concluded that the potential defect site is obviously the point of the final solidification of the heat centre, i.e. in the vicinity of the core.

The accuracy of the simulation is limited, depending on the assumptions used in the mathematical model, the method of the numerical analysis and the values of thermophysical material properties used. Several assumptions were used in the elaboration of the mathematical model. The most important are as follows: the complete heat-transfer rate, a casting temperature equal to the initial temperature of the metal in the mould, and a mould/casting interface with perfect thermal contact. The first assumption restrains the analysis to the mould-casting-core-chill system with heat conduction only, i.e., partial heat flows associated with the mould and core moisture are not considered. The second assumption is the simplification introduced to avoid a complex consideration of the metal flow through the gate system and the mould cavity and the matching heat transfer. The assumption of a perfect thermal contact on the interface is acceptable because there is only a partial appearance of a gaseous clearance, and therefore in the mathematical formulation the boundary condition of the fourth kind is usually taken as valid. The partial differential equation for the heat flow is solved using a numerical method of finite difference – the implicit alternating direction method, which was chosen because of its high accuracy during the approximation of both time and space. Insufficient knowledge about the thermophysical properties of the material, especially at high temperatures, has a strong influence on the simulation of the solidification. It holds especially with respect to the thermal properties of the mould and the core material, which can be determined only experimentally. Moreover, the values for the thermal properties at higher temperatures show a considerable a dissipation.

6 CONCLUSIONS

A numerical simulation of the directional solidification of a leaded red brass flange was carried out on the basis of a suitable mathematical model. The complex model system is composed of four materials: the mould, the core, the chill and the casting of comparatively complicated geometry. The mathematical model of solidification was developed assuming thermal conduction as only heat flow in the system, which is considered as a physically real assumption. A differential equation for the heat flow suited to the flange's geometry was modified and numerically solved by the use of implicit alternating direction method. The temperature dependence of the thermophysical material's properties was taken into account. Based on the obtained algorithm a computer program written in FORTRAN 77 for an Athlon AMD 64 computer was used for the simulation of the solidification. It was determined that the complete solidification takes 367 seconds. The progress of the solidification as well as the hot spot, i.e., the site of any potential shrinkage cavity, can be determined by a shift of isosolidus.

7 REFERENCES

[1] V. Grozdanić, Metalurgija 25 (**1986**) 2, 51
[2] J. H. Leinhard IV, J. H. Leinhard V, A heat transfer textbook, 3rd ed., Phlogiston Press, Cambridge, 2006
[3] V. P. Isachenko, V. A. Osipova, A. S. Sukomel, Heat transfer, 3 rd ed., Mir Publishers, Moscow 1980
[4] R. D. Pehlke, A. Jeyarajan, H. Wada, Summary of thermal properties for casting alloys and mold materials, University of Michigan, Ann Arbor, 1982
[5] J. Douglas, H. H. Rachford, Trans. Amer. Math. Soc., 82 (**1956**), 421
[6] V. Grozdanić, Materiali in tehnologije 43 (**2009**) 5, 233
[7] B. Carnahan, H. A. Luther, J. O. Wilkes, Applied numerical methods, John Wiley, New York, 1969
[8] AFS, Casting coppar-base alloys, American Foundrymen's Society, Des Plaines, 1984
[9] M. R. Spiegel, Laplace transforms, McGraw-Hill, New York, 1965
[10] M. Abramowitz, I. A. Stegun (eds.), Handbook of mathematical functions with formulas, graphs and mathematical tables, National Bureau of Standards, Washington, 1964

Appendix 1

Abbreviations used:

a –- temperature conductivity
a_i, b_i, c_i, d_i – coefficients adjoining unknowns in a tri-diagonal system of algebraic equations
c_p – specific heat capacity at constant pressure
k – thermal conductivity
n – vertical direction
r – space coordinate
t – time
T – temperature
v_i – unknown in system of simultaneous equations
z – space coordinate

Appendix 2

The following partial differential equation of heat flow with the appropriate initial and boundary conditions must be solved to derive the equation for the temperature distribution at the mould/metal interface:

$$\frac{\partial T}{\partial t} = a\frac{\partial^2 T}{\partial x^2} \tag{21}$$

$$\begin{matrix} T(x,0) = T_s \\ T(0,t) = T_i \\ |T(x,t)| < M \end{matrix} \tag{22}$$

where M is a positive real constant.

The equation of heat flow should be solved for the case of the contact of two semi-infinite media. The partial differential equation (21) must be transformed into a common differential equation by the Laplace transform defined as [9]:

$$L\{T(x,t)\} = \Theta(x,s) = \int_0^\infty \mathrm{e}^{-st} T(x,t)\mathrm{d}t \tag{23}$$

Equation (21) in the Laplace region has the from:

$$\frac{d^2\Theta}{dx^2} - \frac{1}{a}s\Theta = -\frac{1}{a}T_s \tag{24}$$

The solution of (24) has the form:

$$\Theta(x,s) = c_1(s)\exp(x\sqrt{s/a}) + c_2(s)\exp(-x\sqrt{s/a}) + \frac{T_s}{s} \tag{25}$$

Because of temperature limitations, $|T(x,t)| < M$, $c_1 = 0$ for $x \to \infty$, i.e.

$$\Theta(x,s) = c_2\ \exp(-x\sqrt{s/a}) + \frac{T_s}{s} \tag{26}$$

For the boundary condition $T(0,t) = T_i$, i.e.

$$\Theta(0,s) = c_2 + \frac{T_s}{s} = \frac{T_i}{s}, \quad c_2 = \frac{1}{s}(T_1 - T_s)$$

The final result in the Laplace region is:

$$\Theta(x,s) = \frac{T_i - T_s}{s}\exp(-x\sqrt{s/a}) + \frac{T_s}{s} \tag{27}$$

By passing from the Laplace region into real space, we have:

$$T(x,t) = (T_1 - T_s)\mathrm{erfc}\left(\frac{x}{2\sqrt{at}}\right) + T_s \tag{28}$$

respectively

$$\frac{(T - T_i)}{(T_s - T_i)} = \mathrm{erf}\left(\frac{x}{2\sqrt{at}}\right) \tag{29}$$

where the error function is defined as [10]:

$$\mathrm{erf}\,(t) = \frac{2}{\sqrt{\pi}}\int_0^t \mathrm{e}^{-u^2}\,\mathrm{d}u \tag{30}$$

The temperature gradient along the x-axis is:

$$\frac{\partial T}{\partial x} = \frac{T_s - T_i}{\sqrt{\pi at}}\exp(-x^2/4at) \tag{31}$$

respectively

$$\left(\frac{\partial T}{\partial x}\right)_{x=0} = \frac{T_s - T_i}{\sqrt{\pi at}} \tag{32}$$

Two semi-infinite media (mould and metal) are in interfacial contact and the boundary condition of the fourth kind is valid:

$$-k_k\left(\frac{\partial T_k}{\partial x}\right)_{x=0} = -k_m\left(\frac{\partial T_m}{\partial x}\right)_{x=0} \tag{33}$$

By including the proper temperature gradients:

$$k_k\frac{T_i - T_s}{\sqrt{\pi a_k t}} = k_m\frac{T_L - T_i}{\sqrt{\pi a_m t}} \tag{34}$$

Finally, the initial temperature distribution on the boundary mould/metal surface is obtained:

$$T_i = T_s + \frac{T_L - T_s}{1 + \frac{K_K}{K_m}\sqrt{\frac{a_m}{a_k}}} \tag{35}$$

Appendix 3

The constants, which in tri-diagonal coefficients, are:

$$p_1 = \frac{a\Delta t}{2(\Delta r)^2}$$

$$p_2 = \frac{a\Delta t}{4r_j \cdot \Delta r}$$

$$p_3 = p_1 - p_2$$

$$p_4 = p_1 + p_2$$

$$p_5 = \frac{\Delta t(k_\mathrm{A} + k_\mathrm{B})}{2c(\Delta r)^2}$$

$$p_6 = \frac{\Delta t(k_\mathrm{A} + k_\mathrm{B})}{4cr_j \cdot \Delta r}$$

$$c = \frac{k_\mathrm{A}}{a_\mathrm{A}} + \frac{k_\mathrm{B}}{a_\mathrm{B}}$$

$$q_1 = \frac{a\Delta t}{2(\Delta z)^2}$$

$$q_2 = \frac{k_\mathrm{A}\Delta t}{c(\Delta z)^2}$$

$$q_3 = \frac{k_\mathrm{B}\Delta t}{c(\Delta z)^2}$$

$$q_4 = \frac{\Delta t(k_\mathrm{A} + k_\mathrm{B})}{2c(\Delta z)^2}$$

$$q_5 = \frac{k_\mathrm{A}\Delta t}{c(\Delta r)^2}$$

$$q_6 = \frac{k_\mathrm{B}\Delta t}{c(\Delta r)^2}$$

Tri-diagonal coefficients

1. Point (i,j) in the mould, metal core or chill – first $\Delta t/2$:

$$\begin{gathered} a_i = c_i = -q_1 \\ b_i = 1 + 2q_1 \\ d_i = p_3 T^n_{i,j-1} + (1-2p_1) T^n_{i,j} + p_4 T^n_{i,j+1} \end{gathered} \tag{36}$$

– second $\Delta t/2$:

$$\begin{gathered} a_j = -p_3 \\ b_j = 1 + 2p_1 \\ c_j = -p_4 \\ d_j = q_1 T^*_{i-1,j} + (1-2q_1) T^*_{i,j} + q_1 T^*_{i+1,j} \end{gathered} \tag{37}$$

2. Point (*i*,*j*) on the boundary surface parallel to the *r* axis separating the material A (left) and B (right)

– first $\Delta t/2$:

$$\begin{gathered} a_i = -q_2 \\ b_i = 1 + q_2 + q_3 \\ c_i = -q_3 \\ d_i = (p_5 - p_6) T^n_{i,j-1} + (1-2p_5) T^n_{i,j} + (p_5 + p_6) T^n_{i,j+1} \end{gathered} \tag{38}$$

– second $\Delta t/2$:

$$\begin{gathered} a_j = -(p_5 - p_6) \\ b_j = 1 + 2p_5 \\ c_j = -(p_5 - p_6) \\ d_j = q_2 T^*_{i-1,j} + (1-q_2-q_3) T^*_{i,j} + q_3 T^*_{i+1,j} \end{gathered} \tag{39}$$

3. Point (*i*,*j*) on the boundary surface parallel to the *z* axis separating the material A (down) and B (up).

– first $\Delta t/2$:

$$\begin{gathered} a_i = c_i = -q_4 \\ b_i = 1 + 2q_4 \\ d_i = (q_5 - q_6) T^n_{i,j-1} + (1-2p_5) T^n_{i,j} + (q_5 + q_6) T^n_{i,j+1} \end{gathered} \tag{40}$$

– second $\Delta t/2$:

$$\begin{gathered} a_j = p_6 - q_5 \\ b_j = 1 + p_5 \\ c_j = -(q_5 - p_6) \\ d_j = q_4 T^*_{i-1,j} + (1-2q_4) T^*_{i,j} + q_4 T^*_{i+1,j} \end{gathered} \tag{41}$$

4. Point (*i*,1) out of the boundary surface

– first $\Delta t/2$:

$$\begin{gathered} a_i = c_i = -q_1 \\ b_i = 1 + 2q_1 \\ d_i = (1-4p_1) T^n_{i,1} + 4p_1 T^n_{i,2} \end{gathered} \tag{42}$$

– second $\Delta t/2$:

$$\begin{gathered} b_j = 1 + 4p_1 \\ c_j = 4p_1 \\ d_j = q_1 T^*_{i-1,1} + (1-2q_1) T^*_{i,1} + q_1 T^*_{i+1,1} \end{gathered} \tag{43}$$

5. Point (*i*,1) on the boundary surface, which separates the material A (left) and B (right)

– first $\Delta t/2$:

$$\begin{gathered} a_i = -q_2 \\ b_i = 2q_4 + 1 \\ c_i = -q_3 \\ d_i = (1-4p_5) T^n_{i,1} + 4p_5 T^n_{i,2} \end{gathered} \tag{44}$$

– second $\Delta t/2$:

$$\begin{gathered} b_j = 4p_5 + 1 \\ c_j = -4p_5 \\ d_j = q_2 T^*_{i-1,1} + (1-2q_4) T^*_{i,1} + q_3 T^*_{i+1,1} \end{gathered} \tag{45}$$

UDK 669.14.018.252:620.18:543.428.2
Original scientific article/Izvirni znanstveni članek

ISSN 1580-2949
MTAEC9, 45(1)55(2011)

CHARACTERIZATION OF THE INCLUSIONS IN SPRING STEEL USING LIGHT MICROSCOPY AND SCANNING ELECTRON MICROSCOPY

KARAKTERIZACIJA VKLJUČKOV V VZMETNIH JEKLIH S SVETLOBNO IN VRSTIČNO ELEKTRONSKO MIKROSKOPIJO

Arsim Bytyqi, Nuša Pukšič, Monika Jenko, Matjaž Godec

Institute of Metals and Technology, Lepi pot 11, 1000 Ljubljana, Slovenia
Štore Steel Company, d. o. o., Železarska cesta 3, 3220 Štore, Slovenia
arsim.bytyqi@imt.si

Prejem rokopisa – received: 2010-04-08; sprejem za objavo – accepted for publication: 2011-01-11

The quality of high-grade steel depends mainly on the size, distribution and composition of the inclusions in the steel. A good-quality product can be obtained by controlling the size, distribution and chemical composition of the inclusions. This study was limited to non-metallic inclusions, mainly compounds of metallic elements and carbon, nitrogen, oxygen or sulfur. The inclusions in spring steel were investigated with light microscopy and scanning electron microscopy. Generalized extreme value theory was applied to the size distribution of the inclusions. The types of inclusions were evaluated and classified in the majority as having a complex non-metallic composition. The experimental results show the possibility to define permissible limits for non-metallic inclusions with a minimal negative influence on the steel's properties.

Keywords: non-metallic inclusions, SEM, EDS, spring steel, GEV

Glavni dejavnik, od katerega je odvisna visoka kakovost jekla, je velikost, razporeditev in sestava nekovinskih vključkov. Z nadzorom velikosti, porazdelitve in kemijske sestave vključkov lahko dobimo kakovosten proizvod. Preiskava je bila omejena na nekovinske vključke, ki so v glavnem spojine kovinskih elementov z ogljikom, dušikom, kisikom ali žveplom. V prispevku sta karakterizacija nekovinskih vključkov in čistost vzmetnega jekla opredeljeni s preiskavami v svetlobnem mikroskopu in v vrstičnem elektronskem mikroskopu. Porazdelitev velikosti vključkov je bila opredeljena s posplošeno teorijo ekstremnih vrednosti. Iz rezultatov je bilo mogoče oceniti naravo vključkov, in sicer je bila večina vključkov kompleksnih, zraščenih z enofaznimi vključki. Rezultati eksperimentalnih postopkov kažejo na možnost določitve dopustne meje nekovinskih vključkov z minimalnim negativnim vplivom na lastnosti jekla.

Ključne besede: nekovinski vključki, SEM, EDS, vzmetno jeklo, posplošena teorija ekstremnih vrednosti

1 INTRODUCTION

Non-metallic inclusions are formed during the steel's production process and have a great impact on the strength, plasticity, fracture toughness, fatigue strength and other properties[1]. Producers can achieve better control of the processing and improve the quality of products by a characterization of the individual inclusions. The size and distribution of inclusions are particularly important, because large macro-inclusions are the most harmful for the mechanical properties of steels[2]. However, large inclusions are difficult to inspect because of their low occurrence rate. Many experimental results show that the largest inclusions are the most probable fracture origins in a given volume of material[3]. Therefore, it is important that steelmakers learn to better control the inclusions' characteristics. The characterization of non-metallic inclusions in steel in terms of number, size, shape and chemical composition is thus an essential requirement for metallurgical process technology. It is necessary to measure the size and spatial distributions of the inclusions for a correlation with the mechanical properties[4]. Different statistical models can be used to characterize the size distribution of inclusions and a lot of effort was expended in recent years to predict the limits for inclusion size or mechanical properties by extrapolating the data[5].

However, despite the major advances in inclusion control, there is still no rapid and accurate method for determining the type, size and number of inclusions present in a steel sample. The scope of possible changes in the production and characterization processes requires scientific studies.

2 EXPERIMENTAL

High-purity steel was produced in Štore Steel, d. o. o., in compliance with the EN 51CrV4 standard. The chemical composition is given in **Table 1**. Five samples with dimensions of 20 mm × 28 mm × 10 mm were cut from the slab according to the ISO 4967 standard. Samples were prepared with standard metallographic techniques, then examined by light microscopy and by scanning electron microscopy (SEM). The advantage of optical microscopy is the ability to examine a large area in a short time, but the information we are able to gather about inclusions is limited. Imaging at higher magnification and microchemical analyses were made using

SEM with an energy-dispersive x-ray spectroscopy (EDS) capability.

The samples were examined with optical microscopy in order to determine the quantity and size of the inclusions. A total of 554 images of polished samples at 100x magnification with a total area of 150 mm^2 were acquired. Image processing and measurements of the inclusion cross-section areas were made with the analySIS software.

The SEM was used in the secondary-electrons imaging and backscattered-electrons imaging modes to analyze the inclusions; details of the composition of the inclusions were investigated by EDS mapping and point analyses.

The light microscopy and SEM analyses (JEOL JSM-6500F) were performed at the Institute of Metals and Technology in Ljubljana.

Table 1: Chemical composition of the spring steel sample No. 49115 in *w*/%

Tabela 1: Kemijska sestava vzorca vzmetnega jekla št. 49115 v masnih deležih, *w*/%

Element	C	Si	Mn	Cr	V	S	Al
Composition *w*/%	0.52	0.35	0.96	0.93	0.12	0.007	0.010

3 RESULTS AND DISCUSSION

3.1 Light microscopy

Since thorough inspection is difficult and time-consuming, statistical methods have been developed for predicting the characteristic maximum inclusion size in a large volume of steel by extrapolating from data gathered on small samples. In this study, Generalized Extreme Value (GEV) theory was applied to the results and a prediction for the characteristic inclusion size was calculated.

The basic concept of extreme value theory is that when a number of data points following a basic distribution are collected on multiple samples, the maxima and minima of each of these sets also follow a certain distribution. The distribution function was given by Gumbel [6,7]:

$$G(z) = \exp\left(-\exp\frac{-(z-\lambda)}{a}\right) \quad (1)$$

where is the probability that the maximum inclusion is no larger than the size z, and a and λ are the scale and location parameters. It was first applied to the inclusion sizes in steels by Murakami and coworkers. The distribution was later generalized with the addition of another parameter ξ:

$$G(z) = \exp\left(-\left[1+\xi\left(\frac{(z-\lambda)}{a}\right)\right]^{-1/\xi}\right) \quad (2)$$

which reduces to the Gumbel distribution (Eq. 1) for ξ = 0.

A standard inspection area S_0 = 0.27 mm^2 was defined and 554 such areas were examined. The cross-section area of the largest inclusion in each inspection area was measured and a square root of the area z =# was calculated. Values of the distribution parameters were then calculated using the maximum-likelihood method. The hypothesis ξ = 0 was not statistically supported and thus abandoned. The parameter values of the generalized extreme-value distribution are listed in **Table 2**.

Table 2: Estimated parameters with standard errors from the GEV method for the experimental steel

Tabela 2: Ocene parametrov s standardnimi napakami za generalizirano metodo ekstremnih vrednosti

Parameter	Value	Std. error
α	1.96	0.06
λ	6.37	0.09
ξ	–0.0089	0.0018

To estimate the size of the maximum inclusion in the volume of spring steel V, the return level T *is* defined as follows:

$$T = V/V_0 \quad (3)$$

where $V_0 = h \cdot S_0$ is the standard inspection volume, as defined by Murakami et al., where $h = \sum\sqrt{area_{\max,i}}/N$. The estimate for the characteristic size of the maximum inclusion is then calculated from [refs]:

$$z_{\max} = \lambda - \frac{a}{\xi}\left(1-\left[-\ln\left(1-\frac{1}{T}\right)\right]^{-\xi}\right) \quad (4)$$

There exists an estimation upper limit of the inclusion size when ξ < 0. The characteristic sizes of the maximum inclusion in different volumes of spring steel are shown in **Figure 1**. The estimation's upper limit is 224 μm. The predicted result of the inclusion size can be used in a database for a reference in the steel-making process.

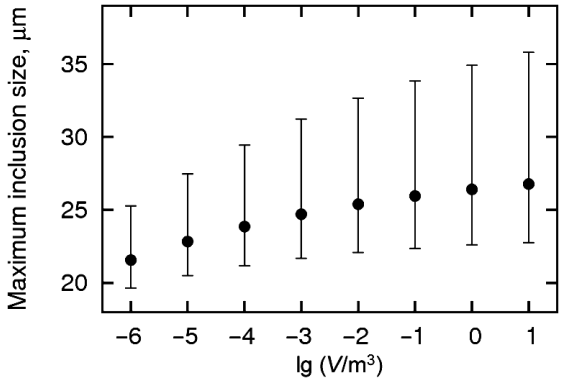

Figure 1: Estimated characteristic sizes of the maximum inclusions in different volumes. Confidence intervals were calculated using the maximum-likelihood method for a 95% confidence level.

Slika 1: Ocenjene karakteristične velikosti največjih vključkov za različne volumne jekla. Intervali zaupanja so bili izračunani po metodi največje verjetnosti za 95-odstotno stopnjo zaupanja.

3.2 SEM analysis

Scanning electron microscopy of the investigated spring-steel samples revealed different types of inclusions. **Figure 2** shows a typical complex inclusion. Three analyses were performed on this inclusion to reveal the detailed composition, mainly of calcium sulfide and aluminum oxide, **Table 2**.

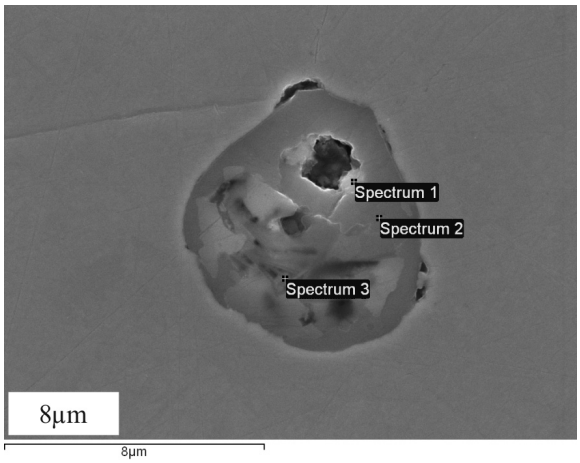

Figure 2: SEM image of a complex, non-metallic inclusion taken by secondary electrons
Slika 2: Kompleksen nekovinski vključkek, posnet s sekundarnimi elektroni v vrstičnem elektronskem mikroskopu

Aluminum oxide inclusions are the result of aluminum de-oxidation. The great advantage of steel de-oxidation with aluminum and the use of calcium to modify the form of alumina inclusions is that they reduce the dissolved oxygen activity in liquid steel, resulting in a final product with a large index of cleanliness and a smaller tendency for porosity formation[8].

Different inclusions were observed with scanning electron microscopy in sample 2. This chemical composition was similar, but the size was different. According to the EDS analysis the content of calcium sulfide (CaS) was greater than the content of aluminum oxide (Al_2O_3). As can be seen in **Figure 3**, aluminum oxide (Al_2O_3) in the inclusion center is surrounded by calcium sulfide (CaS). The distribution of the elements (**Table 3**) indicates that sulphur is bound in the manganese sulphide (MnS).

The analysis of the non-metallic inclusions in the steel 100 Cr6 indicated the presence of complex, oxide-sulfide and sulphide inclusions with different shape characteristics, while, a higher content of the sulphide inclusions is related to the high content of sulphur[9].

A complex inclusion can be seen in **Figure 4**. The detailed analysis of the inclusion supported the finding and showed that the inclusion consisted of calcium sulfide and aluminum oxide. The acquired SEM

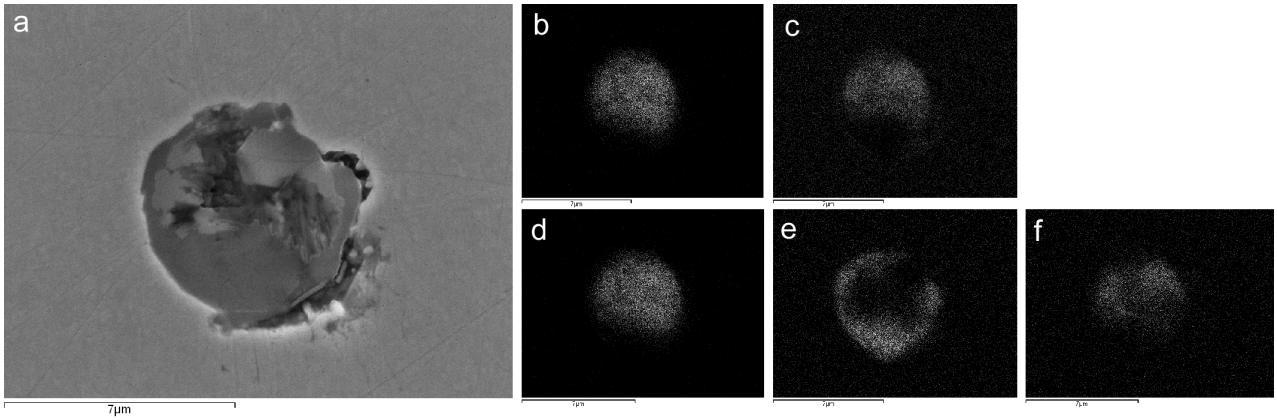

Figure 3: (a) SEM image of a complex, non-metallic inclusion and the corresponding elemental distribution for (b) O Kα1, (c) Mn Kα1, (d) Al Kα1, (e) S Kα1, (f) Ca Kα1.
Slika 3: (a) Nekovinski vključek, posnet s sekundarnimi elektroni v vrstičnem elektronskem mikroskopu in ploskovni posnetki elementov (b) O Kα1, (c) Mn Kα1, (d) Al Kα1, (e) S Kα1, (f) Ca Kα1

Table 2: Semi-quantitative chemical analysis of the inclusion in the studied spring steel in *w*/%
Tabela 2: Semikvantitativna kemijska analiza nekovinskega vključka preiskovanega vzmetnega jekla v masnih deležih, *w*/%

Elements	O	Mg	Al	Si	S	K	Ca	Mn	Fe
Spectrum 1	4.89	—	1.53	—	28.1	—	39.6	3.33	7.80
Spectrum 2	5.48	—	1.53	—	36.1	—	41.1	3.95	6.33
Spectrum 3	48.7	2.42	34.8	2.19	1.29	1.92	4.35	—	4.21

Table 3: Semi-quantitative chemical analysis of the inclusion in *w*/%
Tabela 3: Semikvantitativna kemijska analiza nekovinskega vključka v masnih deležih, *w*/%

Elements	O	Mg	Al	S	Ca	Mn	Fe
Spectrum	4.20	2.06	2.14	33.8	5.52	47.1	5.07

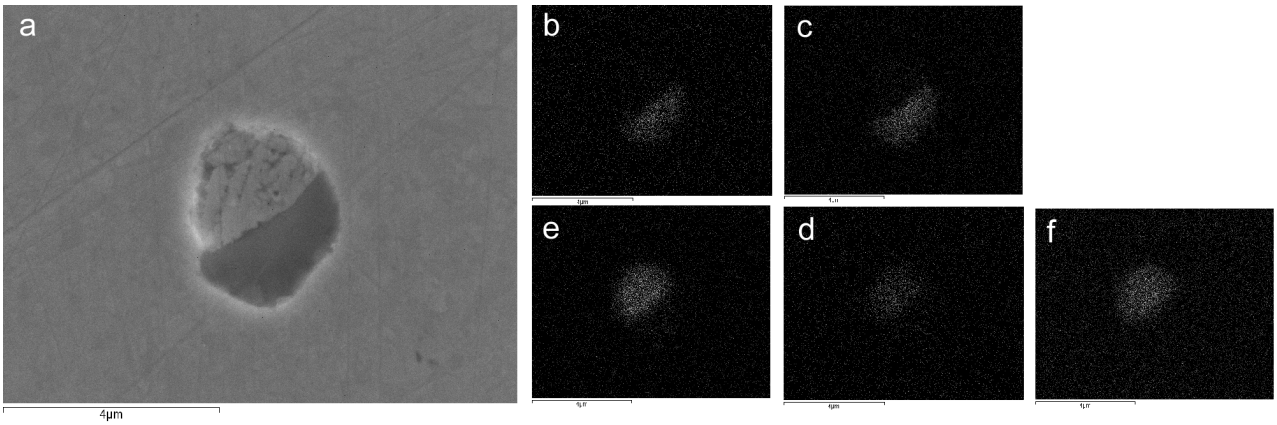

Figure 4: (a) SEM image of a complex, non-metallic inclusion and the corresponding elemental distribution for (b) S Kα_1, (c) Ca Kα_1, (d) Mg Kα_1, (e) Al Kα_1, (f) O Kα_1
Slika 4: (a) Nekovinskih vključki posneti v vrstičnem mikroskopu in ploskovni posnetki elementov (b) S Kα_1, (c) Ca Kα_1, (d) Mg Kα_1, (e) Al Kα_1, (f) O Kα_1

Table 4: Semi-quantitative chemical analysis of the inclusion in the studied spring steel in *w*/%
Tabela 4: Semi-kvantitativna kemična analiza nekovinskega vključka v masnih deležih, *w*/%

Elements	Al	S	Ca	Mn	Fe	Cr	Cu
Spectrum	0.81	26.4	0.37	48.2	22.4	0.64	—-

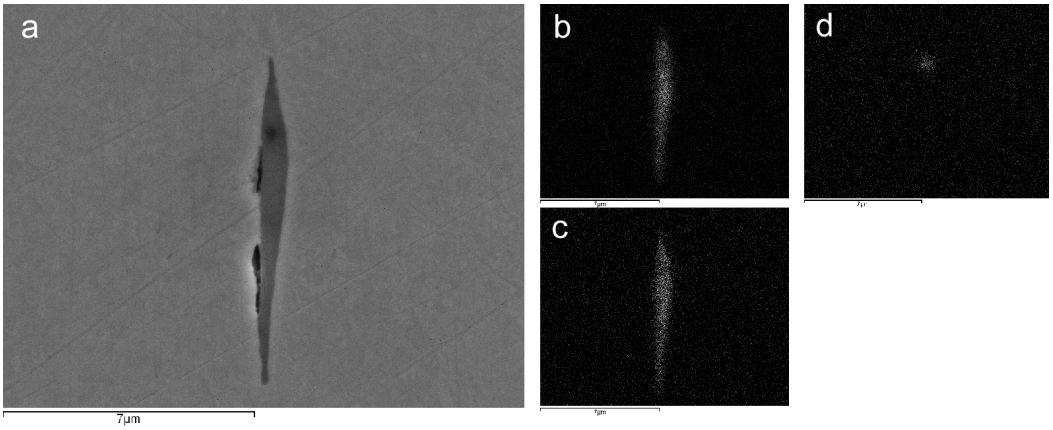

Figure 5: (a) SEM image of a complex, non-metallic inclusion and the corresponding elemental distribution for (b) S Kα_1, (c) Mn Kα_1, (d) Al Kα_1
Slika 5: (a) Nekovinski vključek, posnet s sekundarnimi elektroni v vrstičnem elektronskem mikroskopu in ploskovni posnetki elementov (b) S Kα_1, (c) Mn Kα_1, (d) Al Kα_1

Table 5: Semi-quantitative chemical analysis of the inclusion in **Figure 4** in *w*/%
Tabela 5: Semikvantitativna kemijska analiza nekovinskega vključka s **slike 4** (*w*/%)

Elements	V	S	Cr	Mn	Fe	Total
Spectrum 3	0.48	26.4	1.51	48.2	22.5	100.0

examination revealed that the sulfur and calcium content are lower in the light area of the inclusion than in the dark area. Correspondingly, the oxygen and aluminum contents are higher in the dark area compared with the light area. This indicates that the inclusion is composed of two different parts: the light part mainly consists of aluminum oxide (Al_2O_3), while the dark areas mainly consist of calcium sulfide (CaS) **Table 4**. The characteristic shape of the inclusion is globular and the size is 4 µm. It is quoted in references that inclusions with an irregular shape and sharp edges cause larger stress concentrations around the inclusions than inclusions with a smooth shape, even if there is not a significant difference in the size[10].

Manganese sulfide was found either as a singular inclusion or as an outer shell on an oxide. **Figure 5** shows an SEM image of a sulfide type of inclusion consisting of mass fractions 48.2 % of manganese and 26.4 % of sulfur **Table 5**. These inclusions are narrow and long because of their high ductility at the steel

rolling temperature, and then deform and are elongated as the steel is rolled[11]. Because of their elongated shape, MnS inclusions may affect the transverse toughness of the steel[12]. Apart from the chemical composition, the size of the inclusions is crucial for the steel's properties. The results show that the critical inclusion size in the spring steel 51CrV4 was 0.14mm[13].

4 CONCLUSION

The nonmetallic inclusions in spring steel were investigated in the laboratory, and the inclusion size distribution and compositions were determined using optical microscopy according the international standard ISO 4967 and with SEM combined with EDS, respectively.

The more specific conclusions from this work are as follows. The majority of inclusions found in steel contain manganese sulfide (MnS), calcium sulfide (CaS) and aluminum oxide (Al_2O_3) or a mixture of these. A comparison between the inclusion compositions in the spring steel showed that they are very similar in terms of chemical composition. The SEV method can be effectively used to estimate the size of the maximum inclusion in different volumes of the spring steel. However, a reasonable estimation can be derived from the combined analysis of two methods, i.e., the metallographic and statistically methods. The inclusion characteristics are not sufficiently investigated for many of the commercially available spring steels and should be amended.

5 REFERENCES

[1] Gao Hong-bin., Jia Yun-hai., Li Mei-ling., Yuan Liang-jing, WANG Hai-zhou. Research on original position statistic distribution analysis model of aluminum inclusion grain size in steel. Central Iron&Steel Research, 2009

[2] Lifeng Zhang., Brian G. Thomas. Inclusions in continuous casting of steel. Mech. Engr. Buldg. (**2003**), 138–183

[3] A. Ahmad, J. Purbolaksono, Z. Yahya., Estimating inclusion size in WE43-T6 magnesium alloys based on Gumble extreme values. Materials Science and Engineering. A 513–514 (**2009**), 319–324

[4] Shehata M. T. Boyd J. D. Measurement of Spatial Distribution of Inclusions. Inclusions and their Influence in Material Behavior, 4 (**1998**), 123–131

[5] Atkinson H. V., Sh. G. Characterization of Inclusions in clean steels; A review including the statistics of extremes methods. Progress in Materials Science, 48 (**2003**) 5, 457–520

[6] J. M. Zhang, J. F. Zhang, Z. G Yang, G. Y. Li, G. Yao, S. X. Li, W. J. Hui, Y. Q. Wenig, Estimation of maximum inclusion size and fatigue strength in high strength ADF1steel. 394 (**2005**), 126–131

[7] C. W. Anderson, G. Shi, H. V. Atkinson, C. M. Sellars, J. R. Yates, Interrelationship between statistical methods for estimating the size of maximum inclusion in clean steels. Acta Materiala. 51 (**2003**), 2331–2343

[8] Jose Carlos, S. Pires, Amauri Garcia. Modification of oxide inclusions present in aluminum-killed low carbon steel by addition of calcium. Metalurgia & Materialis., 57 (**2004**), 1–5

[9] A. Gigovič, M. Oruč, I. Vitez, B. Vujičič. Analyse and research of nonmetallic inclusions for steel 100Cr6. Metalurgija, 48 (**2009**), 29–32

[10] Pekko Juvonen. Effectc of non-metallic inclusions on Fatigue properties of Calcium Treated Steels. Helsinki University of Technology, PhD Thesis, (**2004**), 14

[11] L. M. Cabalin, M. P. Mateo, J. J. Laserna. Large area mapping of non-metallic inclusions in stainless steel by an automated system based on laser ablation. Elsevier. Spectrochimica Acta Part B, 4 (**2004**), 567–575

[12] Claude Lincourt, Madhavarao Krishnadev. Effect of inclusion morphology on the fracture toughness of high strength steels. Mater. Technol. 27 (**2009**), 1687–1698

[13] Miha Kovačič, Sandra Senčič. Critical Inclusion Size in Spring Steel and genetic programming. Materials and Geoenvironment, 57 (**2010**), 17–23

UDK 669.24'29:543.428.2
Original scientific article/Izvirni znanstveni članek

ISSN 1580-2949
MTAEC9, 45(1)61(2011)

CHARACTERIZATION OF THE CARBIDES IN A Ni-Ti SHAPE-MEMORY ALLOY WIRE

KARAKTERIZACIJA KARBIDOV V ŽICI ZLITINE S SPOMINOM Ni-Ti

Matjaž Godec, Aleksandra Kocijan, Monika Jenko

[1]Institute of Metals and Technology, Lepi pot 11, 1000 Ljubljana, Slovenia
matjaz.godec@imt.si

Prejem rokopisa – received: 2010-09-27; sprejem za objavo – accepted for publication: 2010-10-19

The microstructure of a commercially available Ni-Ti shape-memory alloy was investigated with Scanning Electron Microscopy (SEM), Energy-Dispersive X-ray Spectroscopy (EDS) and Electron Backscatter Diffraction (EBSD) patterns. The material investigated was a Ni-Ti shape-memory alloy with the chemical composition in the mass fraction: C 0.1 %, Ni 45 % and Ti 54.9 %. The microstructure of the alloy consisted of nanosized crystal grains of the Ni-Ti phase and particles of titanium carbides. The majority of the particles were aligned in the longitudinal direction parallel to the wire's axis. The problems occurring during the EBSD analysis of the Ni-Ti phase are discussed and some orientational relationships between the carbides and the matrix are suggested.

Key words: shape memory alloy, Ni-Ti, TiC, EBSD, EDS

Raziskali smo mikrostrukturo komercialne zlitine s spominom Ni-Ti z uporabo vrstične elektronske mikroskopije (SEM), energijsko disperzijske spektroskopije (EDS) in uklona sipanih elektronov (EBSD). Preiskovani material je bila zlitina s spominom Ni-Ti s kemijsko sestavo v masnih deležih: C 0.1 %, Ni 45 % in Ti 54.9 %. Mikrostruktura zlitine je bila sestavljena iz nanokristalnih zrn faze Ni-Ti in titanovih karbidov. Večina karbidov je bila usmerjena vzdolžno z osjo žice. Opisani so problemi EBSD-analize faze Ni-Ti in predlagane orientacijske odvisnosti med karbidi in matrico.

Ključne besede: zlitina s spominom, Ni-Ti, TiC, EBSD, EDS

1 INTRODUCTION

Porous Ni-Ti shape-memory alloys are widely used in numerous biomedical applications (orthodontics, cardiovascular, orthopedics, urology, etc.) because of their good biocompatibility, unique shape-memory properties, mechanical properties, superior damping capability, excellent corrosion resistance and wear resistance [1–6]. They combine their special functional properties with a high mechanical strength [7]. These characteristics are due to the martensitic transformation and its reversion, which can be activated by thermal or mechanical loads [7]. The Ni-Ti alloy has similar mechanical characteristics to natural biomaterials, e.g., a high recoverable strain and a low elastic modulus [8,9], both of which are very similar to bone. This makes the alloy an ideal biological engineering material for orthopedic surgery and orthodontics [10]. Despite these advantages, the high Ni content (50 %) in the Ni-Ti shape-memory alloy is a major health concern [11]: the toxicity, carcinogenicity and allergic hazards associated with Ni have been the subject of a number of studies [12,13]. One of the most effective and obvious solutions is to improve the surface microstructure and modify the properties. Of course, one of the basic requirements for any metallic implant is that it should not exhibit any toxicity and that it should be biocompatible.

The properties of a Ni-Ti shape-memory alloy depend strongly on the exact chemical composition, the processing history, and the level of impurities [7]. For example, contaminants such as oxygen and carbon can dramatically affect the properties of the alloy; their penetration tends to occur during the production and processing of the alloy [7].

To obtain a good shape-memory effect it is crucial to have a good chemical homogeneity of the material, which then leads to single-phase Ni-Ti formation. The usual process to produce Ni-Ti shape-memory alloys is called Vacuum Induction Melting (VIM), using high-density graphite crucibles to minimize the carbon contamination of the melt. The carbon combines with the titanium, which results in the precipitation of TiC particles. The consequence is an alloy matrix that is richer in nickel than the nominal composition, which means a lowering the martensitic transformation temperatures [3,14–16]. The higher concentration of Ni in the Ni-Ti matrix increases the risk of allergic and toxic reactions [1] as well as reducing the shape-memory effect. The precipitated titanium carbides have been reported to have a certain orientational relationship with the matrix [16].

In the present study the microstructure of a commercial Ni-Ti orthodontic wire produced by vacuum induction melting was examined with Scanning Electron Microscopy and Electron Backscatter Diffraction (EBSD) patterns. The problems occurring during the indexing of the EBSD patterns of the Ni-Ti phase are described and some of the orientational relationships

between the carbide particles and the matrix are suggested.

2 EXPERIMENTAL

The material used was a Ni-Ti shape-memory alloy with the following chemical composition in mass fractions: C 0.1 %, Ni 45 %, Ti 54.9 %. An orthodontic archwire specimen (ϕ 0.2 mm × 100 mm) was hot mounted in conductive Bakelite, ground and polished. The usual diamond polishings with 3 μm and 1 μm particles were prolonged to 10 min each; these were followed by colloidal silica oxide polishing for 5 min and then cleaning in an ultrasonic bath. The specimen was analyzed in a FE-SEM JEOL JSM 6500F field-emission scanning electron microscope using energy-dispersive X-ray spectroscopy (EDS), an INCA X-SGHT LN2-type detector, INCA ENERGY 450 software, and an HKL Nordlys II EBSD camera using Channel 5 software. The microstructure was revealed with etching in 85 % H_20, 5 % HF and 10 % HNO_3. For the EDS analyses a 15-kV accelerating voltage and a probe current of 0.7 nA were used. The parameters chosen represent a good compromise between the size of the analyzing volume and the overvoltage needed to detect the elements present. The EBSD was performed at a 15-kV accelerating voltage and a 2.6 nA probe current. The analysis was made using 40 reflectors and 4 × 4 binning. For the noise reduction, 10 frames were used, and each frame was obtained at 20 ms. The obtained crystallographic data were analyzed using the Channel 5 software and the ICSD 2003 database.

3 RESULTS AND DISCUSSION

The thermomechanical behavior of shape-memory alloys is obtained with the martensitic-austenitic phase transition, which depends on the temperature and the stress, and occurs as a result of the martensitic twinning at low temperatures. The hysteresis loop of the analyzed shape-memory alloy has a martensite start at 2 °C and a martensite finish at –15 °C, and an austenite start at 18 °C and an austenite finish at 36 °C, in order to achieve the phase transformation from martensite to austenite, which is typical for applications at human-body temperature [17]. The microstructure of the investigated alloy consists of the Ni-Ti phase with a number of titanium carbide particles (**Figure 1**). The high carbon content of 0.1 % is due to the dissolution of carbon from the crucible graphite in the melt during the vacuum induction melting [16]. The titanium carbides might lower the concentration of nickel in the matrix; however, a beneficial effect of increased hardness may occur, particularly if the interface between the titanium carbide and the Ni-Ti phase is semi-coherent [16].

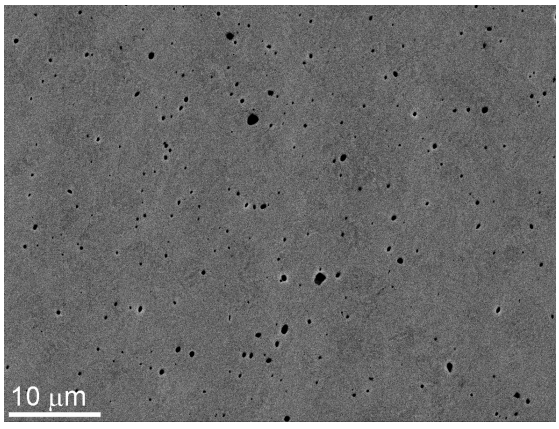

Figure 1: Polished transversal cross-section of NiTi wire. Black spots represent titanium carbides in the NiTi matrix. Micrograph obtained in scanning electron microscope using backscattered electrons.

Slika 1: Prikaz poliranega prečnega prereza NiTi žice. Temna področja so titanovi karbidi v NiTi matrici. Slika je bila posneta v vrstičnem elektronskem mikroskopu z odbitimi elektroni.

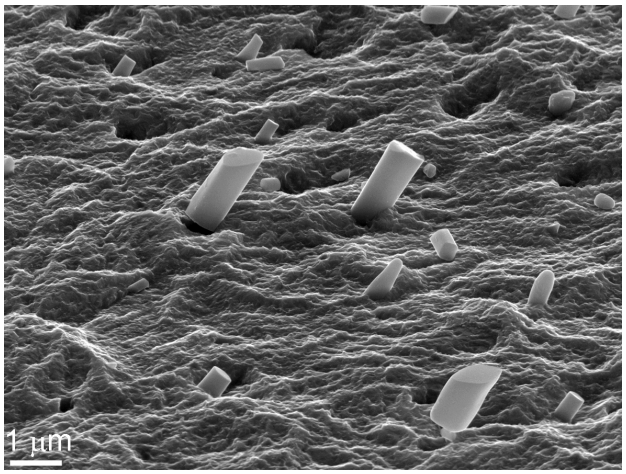

Figure 2: Etched transversal cross-section of NiTi wire with visible carbides in longitudinal direction. Micrograph obtained from secondary electrons in 60° tilted mode.

Slika 2: Prikaz jedkanega prečnega prereza NiTi-žice z vidnimi karbidi v vzdolžni smeri. Slika je bila posneta s sekundarnimi elektroni, vzorec nagnjen za 60°.

Chemical etching of the Ni-Ti surface prior to the surface characterization causes a rapid attack on the NiTi matrix, while the titanium carbides were not affected. Therefore, in the highly tilted mode in the Scanning Electron Microscope the carbide particles, and especially their shape, become clearly observable (**Figure 2**). The longitudinal direction of the carbide is parallel to the wire's longitudinal direction. This specific situation may result from two possible factors concerning the precipitation of carbide particles. The first one is related to the manufacturing of the shape-memory Ni-Ti alloy, which is associated with the casting and the plastic deformation of the wire at elevated temperatures. The carbides might precipitate during the casting solidification [16] and later during the plastic working with hot rolling and drawing when the non-deformable particles are aligned in the longitudinal direction of the wire. In this case, the carbide particles have no orientational relationship with the matrix because of the re-crystallization during or after the wire drawing. On the other hand, the particles

may have precipitated during the wire drawing, which would impact on the specific growth direction of the particles. The titanium carbides have a rod-like shape; however, the transversal cross-section is not completely circular; in some cases it is closer to a square with rounded edges. It is most likely that the wire was manufactured by continuous casting and drawing, so that the carbides precipitate during the casting and have a specific orientation due to the tension gradient in the drawing direction. This can explain why the carbides are not broken into small pieces, which is what usually occurs with aluminum or silicon non-metallic inclusions in steels during plastic deformation. Some of the carbide particles are slightly thinner at their ends, which is typical evidence that the precipitation and the drawing took place at a high enough temperature to allow plastic deformation also of the carbides.

The EBSD analysis was performed on highly polished surfaces where the carbide particles formed just a slight topography. Based on the available ICSD 2003 database [18,19], the EBSD patterns were solved almost equally as TiC or Ti_8C_5. However, a slightly better MAD (mean angular deviation) number was obtained for the TiC phase. Zhang et al. reported the lattice of titanium carbide particles as being cubic TiC [16]. TiC is in a wider region according to the phase diagram calculated using the Thermo Calc program [20]. TiC can have the B1 (or NaCl-type) lattice with the titanium atoms situated in a face-centered-cubic, closed-packed arrangement with the octahedral interstitial sites occupied by carbon atoms [21]. The equilibrium phase diagram exhibits only one carbide phase, TiC, which is characterized by a wide region of composition (from $TiC_{0.48}$ to $TiC_{1.00}$) and melts congruently at 3068 °C [22]. The reason why both carbides create almost identical patterns from the interaction of electrons with the crystal structure is that in both lattices the atoms are in a close-packed formation and the similar ordering creates similar electron refraction. Because of the very similar EBSD patterns of both the equilibrium and non-equilibrium carbides, it is not possible to exclude the existence of the Ti_8C_5 carbide. Nevertheless, the shape of the carbide rods, with their slightly square transversal shape, might be more indicative of the equilibrium cubic TiC. The internal stress can have an influence on the carbide growth at high temperature and might change the bulky crystal shape. Some hexagonal form, for instance an angle of 120°, is to be expected also. **Figure 3** shows the EBSD pattern of a typical TiC particle. The orientation of the crystal is such that the longitudinal direction of the carbide is parallel to the wire.

EDS microchemical analyses were performed on some carbide particles. However, an accurate EDS carbon analysis is always a challenge. The system used has no liquid-nitrogen trap and therefore some excess carbon due to contamination is always observed. Depending on the material analyzed, some carbon build up under the electron beam is usually observed during the EDS measurement in the range of mole fractions 10 % or 15 % in steels and Ni-Ti alloys, respectively. The carbon in the vacuum analyzing chamber originates mostly from the oil vapor in the diffusion pumps. Taking into account this particular fact and from the EDS measurements on titanium carbides, it is possible to conclude that the carbides are closer to TiC than Ti_5C_8. Unfortunately, using the WDS technique gives no improvement in such conditions; on the contrary, it makes the measurements even less reliable. The phenomenon of carbon build up is even more intense due to the higher current. **Figure 4** shows EDS spectra from typical carbides in the Ni-Ti shape-memory alloy and the calculated chemical composition of the carbide. From the EDS spectra the calculated atomic ratio of Ti to C is approximately 1:1. There is, however, some excess amount of carbon due to the vacuum problem mentioned above. A certain amount of oxygen was also observed in

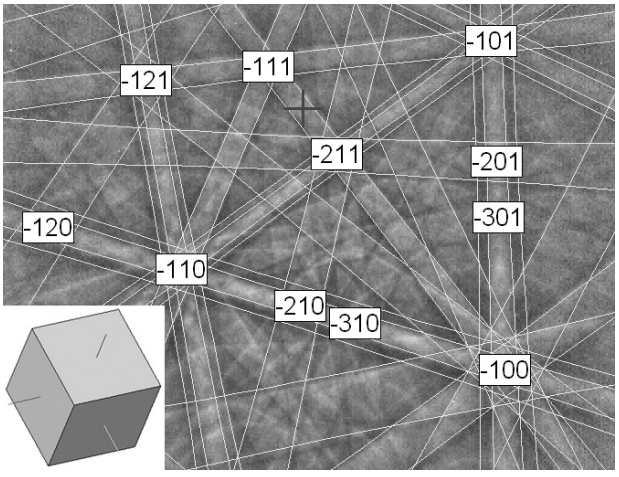

Figure 3: EBSD pattern of typical TiC carbide in longitudinal direction of the wire. The pattern was solved as TiC with the orientation of the crystal shown in the figure.

Slika 3: EBSD-slika tipičnega TiC-karbida v vzdolžni smeri žice. Elektronska uklonska slika prikazuje TiC s kristalno orientacijo, prikazano na sliki.

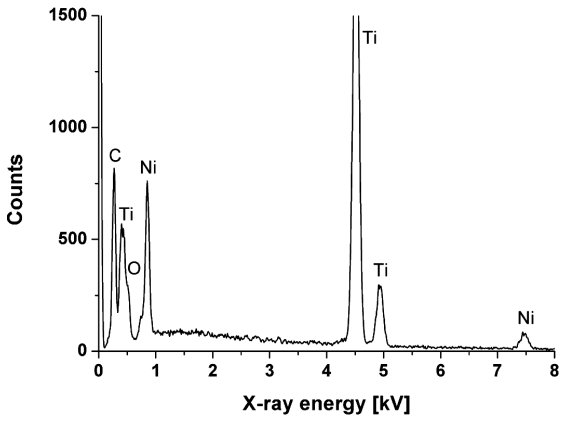

Figure 4: EDS spectrum of carbides shows slightly larger amount of carbon that belongs to the TiC. The excess amount is due to carbon build up under the electron beam.

Slika 4: EDS-spekter karbidov, ki prikazuje nekoliko povišan delež ogljika glede na TiC. Presežek ogljika je zaradi nalaganje pod elektronskim curkom.

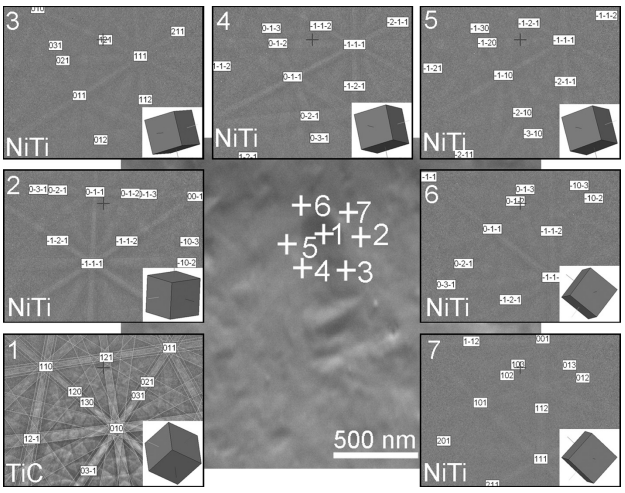

Figure 5: Marked area of EBSD spot analysis with corresponding EBSD pattern. Spot 1 shows the carbides, spots 2 to 7 show Ni-Ti matrix with nanograins.

Slika 5: Označeno mesto EBSD točkovne analize s pripadajočo EBSD uklonsko sliko. Mesto 1 prikazuje karbid, mesta od 2 do 7 prikazujejo Ni-Ti matrico z nanozrni.

the EDS spectra. It was reported previously that the presence of carbon and oxygen can result in the formation of different titanium carbides and oxides [23].

To prepare the Ni-Ti alloy for the EBSD investigation was a demanding task. Two different approaches were tested: polishing of the surface with argon ions and polishing by using silica oxide nanoparticles. The latter was more successful, however. It is believed that the highly energetic ions may affect the lattice and induce some internal stresses, which could be reflected in the EBSD pattern, as observed during the EBSD mapping. In these analyses the indexing and the band-contrast image constantly deteriorated during the EBSD mapping. The explanation for this may also be found in the austenite-martensite transformation as well as the martensite twining caused by the interaction of electrons and the specimen being analyzed. Most likely this problem is related to the contamination of the surface during EBSD analysis as well as local oxidation of the surface.

The orientational relationship of the titanium carbides (with the B1 crystal structure) and the Ni-Ti matrix (with the B2 crystal structure) was established (**Figure 5**). It was found that the majority of the TiC particles have the same orientation, and without any clear relationship with the NiTi matrix lattice. However, it is related to the longitudinal direction of the wire, as the EBSD analysis showed that majority of titanium carbides had the longitudinal direction [111]. The grain size of the Ni-Ti phase was in the range of 200 nm.

4 CONCLUSIONS

The present study was conducted in order to characterize a commercially available Ni-Ti shape-memory alloy. It was found that the microstructure of the analyzed shape-memory alloy consisted of nanosized crystal grains of the Ni-Ti phase with a number of titanium carbides. The chemical analyses confirmed that the excess amount of carbon originated from the induction-melting process in the graphite crucible, which decreased the shape-memory effects due to the formation of TiC precipitates. The titanium carbides were rod shaped, while the transversal cross-section shape was in the form of a modified circle, although in some cases it was close to a square with rounded edges. The majority of the carbides were aligned parallel to the wire axis, which can be associated with an orientation change during the plastic deformation. It is also possible that the particles grow faster in the longitudinal direction due to the stresses produced by the wire drawing. The grain size of the Ni-Ti phase was in the range of 200 nm, and the majority of the carbides had a direction parallel to the wire's longitudinal direction [111].

Acknowledgements

The authors are grateful to Dr. Janez Rozman for providing the investigated samples.

5 REFERENCES

[1] Neelakantan L, Swaminathan S, Spiegel M, Eggeler G, Hassel A W, Selective surface oxidation and nitridation of NiTi shape memory alloys by reduction annealing *Corros. Sci.,* 51 (**2009**), 635–641

[2] Kim J I, Miyazaki S, Effect of nano-scaled precipitates on shape memory behavior of Ti-50.9at.%Ni alloy, *Acta Materialia,* 53 (**2005**), 4545–4554

[3] Saburi T, in: *Shape memory materials*, Otsuka K, Wayman C M, eds, Cambridge University Press, Cambridge, UK, 1998, p. 49

[4] Otsuka K, Ren X, Recent developments in the research of shape memory alloys *Intermet,.* 7 (**1999**), 511–528

[5] Duerig T, Pelton A, Stöckel D, An overview of nitinol medical applications, *Mater. Sci. Eng.* A, 273–275 (**1999**), 149–160

[6] Chu C L, Chung C Y, Lin P H, Wang S D, Fabrication of porous NiTi shape memory alloy for hard tissue implants by combustion synthesis *Mater. Sci. Eng.* A, 366 (**2004**), 114–119

[7] Mehrabi K, Bahmanpour H, Shokuhfar A, Kneissl A, Influence of chemical composition and manufacturing conditions on properties of NiTi shape memory alloys *Mater. Sci. Eng.* A, 481 (**2008**), 693–696

[8] Gjunter V E, *Superelastic shape memory implants in maxillofacial surgery, traumatology, orthopaedics and neurosurgery,* Tomsk University Publishing House (TUP), Tomsk, Russia, 1995

[9] Helsen J A, Breme H J, *Metals as biomaterials*, Wiley, Baffins Lane, Chichester, England, 1998

[10] Gil F X, Planell J A, Manero J M, Relevant aspects in the clinical applications of NiTi shape memory alloys *J. Mater. Sci.: Mater. Med.*,7 (**1996**), 403–406

[11] Chu C L, Guo C, Sheng X B, Dong Y S, Lin P H, Yeung K W K, Chu P K, Microstructure, nickel suppression and mechanical characteristics of electropolished and photoelectrocatalytically oxidized biomedical nickel titanium shape memory alloy *Acta Biomaterialia,* 5 (**2009**) 6, 2238–2245

[12] Williams D F, *Fundamental aspects of biocompatibility*, in: Toxicology of implanted metals, CRC Press, Boca Raton, FL, 1981, vol. II

[13] Takamura K, Hayashi K, Ishinishi N, Yamada T, Sugioka Y, Evaluation of carcinogenicity and chronic toxicity associated with

orthopedic implants in mice *J. Biomed. Mater. Res.,* 28 (**1994**), 583–589

[14] Otubo J, Rigo O D, Neto C M, The Mei P R, effects of vacuum induction melting and electron beam melting techniques on the purity of NiTi shape memory alloys *Mater. Sci. Eng.* A, 438 (**2006**), 679–682

[15] Tang W, Sundmann B, Sandström R, Qiu C, New modelling of the B2 phase and its associated martensitic transformation in the Ti-Ni system *Acta Mater.,* 47 (**1999**), 3457–3468

[16] Zhang Z H, Frenzel J, Somsen C, Pesicka J, Eggeler G, in: Progress in Crystal Growth Research, Karas G V, ed., Nova Science Publishers, New York, USA, 2005

[17] https://www.goodfellow.com (2008–2010)

[18] Zhou Y C, Wang X H, Sun Z M, Chen S Q, Electronic and structural properties of the layered ternary carbide Ti_3AlC_2 *J. Mater. Chem.,* 11 (**2001**), 2335–2339

[19] Khayenko B V, Golub V I, Arbuzow M P, *Kristallografiya* 25 (**1980**), 112–118

[20] Sundman B, Thermo-Calc Software Version S, Royal Institute of Technology, Stockholm, 2008

[21] Jeitschko W, Pottgen R, Hoffman R D, Structural chemistry of hard materials, in: Handbook of Ceramic Hard Materials, Riedel R, ed, Wiley-VCH, New York, 2003, p. 9

[22] Jonsson S, Assessment of the Ti–C system *Z. Metallkd.,* 87 (**1996**), 703–772

[23] Mentz J, Frenzel J. Wagner M F -X, Neuking K, Eggeler GBuchkremer, H P, Stöver D, Powder metallurgical processing of NiTi shape memory alloys with elevated transformation temperatures, *Mater. Sci. Eng.* A, 491 (**2008**), 270–278

UDK 669.14.018.252:539.42
Original scientific article/Izvirni znanstveni članek

ISSN 1580-2949
MTAEC9, 45(1)67(2011)

FRACTURE TOUGHNESS OF THE VACUUM-HEAT-TREATED SPRING STEEL 51CrV4

LOMNA ŽILAVOST VAKUUMSKO TOPLOTNO OBDELANEGA VZMETNEGA JEKLA 51CrV4

Bojan Senčič[1], Vojteh Leskovšek[2]

[1]Štore Steel, d. o. o., Železarska cesta 3, SI-3220 Štore, Slovenia
[2] Institute of metals and technology, Lepi pot 11, 1000 Ljubljana, Slovenia
bojan.sencicŽ

Prejem rokopisa – received: 2011-01-12; sprejem za objavo – accepted for publication: 2011-01-17

In the work the possibilities of the vacuum heat treatment of spring steel grade 51CrV4 are presented. Charpy-V notch (CVN) impact-test values are widely used in toughness specifications for spring steels, even though the fracturing energy is not directly related to the spring design. The plain-strain stress-intensity factor (K_{Ic}) at the onset of unstable crack growth can be related to the spring design; however, K_{Ic} values are not used in the toughness specifications. This is surprising since to the designer K_{Ic} values are more useful than CVN values, because the design calculations for springs from high-strength steels should also take into account the strength and the toughness of materials to prevent rapid and brittle fracture. An investigation was conducted to determine whether standardized fracture-toughness testing (ASTM E399-90), which is difficult to perform reliably for hard and low ductility materials, could be replaced with a non-standard testing method using circumferentially notched and fatigue-precracked tensile specimens. The results of this investigation have shown that using the proposed method it was possible to draw, for the normally used range of working hardness, combined tempering diagrams (Rockwell-C hardness – Fracture toughness K_{Ic} – Tempering temperature) for the vacuum-heat-treated spring steel grade 51CrV4. Fractographic and metallographic analyses of the K_{Ic}-test specimens used shows in steel the presence of positive and negative segregations. It was found that the width of the segregations bands and the distance between the positive and negative segregations influence significantly the fracture toughness due to the presence of bainite in the negative segregations.

Keywords: spring steels, vacuum heat treatment, hardness, fracture toughness, microstructures

V članku so predstavljene možnosti vakuumske toplotne obdelave vzmetnega jekla 51CrV4. Vrednosti Charpy-V udarne žilavost (CVN) so pogosto navedene v specifikacijah za vzmetna jekla, čeprav energija loma ni neposredno povezana z dimenzioniranjem vzmeti. Ravninsko deformacijski faktor intenzitete napetosti (K_{Ic}) na začetku nestabilne razpoke lahko uporabimo pri dimenzioniranju vzmeti, vendar pa vrednosti K_{Ic} ne najdemo v specifikacijah. To je presenetljivo, saj so za konstruktorje vrednosti K_{Ic} bolj uporabne od vrednosti CVN za visokotrdnostne vzmeti, pri katerih je treba upoštevati poleg trdnosti tudi žilavost materiala, da preprečimo lom. Opravljena je bila preiskava, s katero smo želeli ugotoviti, ali lahko standardizirano preizkušanje lomne žilavosti (ASTM E399-90), ki je težko izvedljivo za trde in krhke materiale z majhno duktilnostjo, nadomestimo z nestandardnim postopkom preizkušanja lomne žilavosti s cilindričnim nateznim preizkušancem z zarezo po obodu in utrujenostjo razpoko v dnu zareze. Rezultati raziskave so pokazali, da s predlagano metodo lahko konstruiramo diagram popuščanja (trdota Rockwell-C – lomna žilavost K_{Ic} – temperatura popuščanja) za vakuumsko toplotno obdelano vzmetno jeklo 51CrV4. S fraktografsko in metalografsko analizo K_{Ic} preizkusnih vzorcev smo ugotovili prisotnost pozitivnih in negativnih izcej v jeklu. Ugotovljeno je bilo, da širina izcej in razdalja med njimi pomembno vplivata na lomno žilavost, in sicer zaradi prisotnosti bainita v negativnih izcejah.

Ključne besede: vzmetno jeklo, vakuumska toplotna obdelava, trdota, lomna žilavost, mikrostruktura

1 INTRODUCTION

A manufacturer of spring steels must provide a technical steel description in their production program. Namely, the durability of the springs is limited by plastic deformation, fatigue and fracturing. From this point of view, the use of spring steel with the following properties is recommended: high ductility and toughness at operating temperatures from –40 °C to +50 °C, good hardenability that provides the required mechanical properties, even at the maximum dimensions.

Steels with a similar chemical composition may behave differently due to various mechanical properties as a consequence of the manufacturing route. The description of the spring steel includes the chemical composition and the basic mechanical and physical as well as technological properties. For the manufacturers of springs, the information relating to the heat treatment of a specific spring steel is important. Assuming that the chemical composition and initial microstructure of the steel correspond to prescribed for steel grade 51CrV4 (DIN 17221 and DIN 17222), then the mechanical properties for a specific application depend mainly on the appropriately selected parameters of the heat treatment.

Hypo-eutectoid steels, such as the spring steel 51CrV4, are usually heat treated conventionally in a furnace with or without a protective atmosphere at a temperature of 30 °C to 50 °C above the A_{c3} point soaked at the austenizing temperature to obtain "homogeneous austenite", and oil cooled to the temperature of the quench oil. The quenching is followed by a tempering at a selected temperature. The conventional tempering diagram for spring steel gives us information about the

mechanical properties, i.e., the tensile strength R_m, yield strength $R_{p0.2}$, elongation A_5 and necking Z as a function of the tempering temperature in the range from 350 °C to 700 °C for a specific austenitizing temperature. In the case of spring steels, a minimum impact toughness Charpy-V measured by standard CVN-specimens, must be given. Lately, more and more users also request measured values of the fracture toughness K_{Ic} for the springs after heat treatment, which with the known ultimate tensile strength allows us to calculate the fracture stress σ_f and the critical defect size a_{cr} at the applied stress.

The trend of the heat treatment of machine parts, including springs, is in the direction of vacuum heat treatment. Namely, cooling rates that can be achieved in modern vacuum furnaces with cooling in a stream of N_2 or in a mixture of He and N_2 under a pressure up to 25 bar, already reach cooling speeds close to the cooling rates in oil. One can expect that the obtained microstructure and mechanical properties of the springs after vacuum quenching and tempering will be comparable to those achieved with a conventional heat treatment. In vacuum heat treatment, there is no risk of decarburization, no formation of the oxide layer and no residues of quench oil on the surface. It offers then a significant advantage when compared to conventional heat treatment. The objective of our work was to create a specific tempering diagram for the investigated steel 51CrV4 from which the relations between the Rockwell-C hardness, the fracture toughness K_{Ic}, the austenizing and the tempering temperature could be determined.

2 THEORETICAL PART

2.1 Hardness, ductility and toughness

Factors contributing to the isotropic mechanical properties of steel are a high cleanliness, a low level of residual elements, of non-metallic inclusions (NMI) and primary carbides without segregations. This can be achieved with an appropriate process route of the continuous cast spring steel through the Clean Steel Concept[1] using the Continuous Soft Reduction (CSR)[2] process.

The properties used to evaluate the heat treatment of spring steel are the Rockwell-C or Brinell hardness. In the hardened state the hardness may be an indication of the austenitizing temperature, from which the spring steel has been quenched. In the tempered state, the hardness is important for users, although based on the hardness, it is not possible to distinguish between the springs that were quenched and tempered in various ways. For example, the same hardness can be achieved by varying the austenitizing and tempering temperature, but the toughness can be different. From this point of view, it has sense to introduce into the tempering diagram an additional criterion such as toughness. Unfortunately, for the determination of toughness there are no generally accepted test methods. Consequently, the literature often refers to the data determined by different test methods. The comparison of these data may sometimes lead to confusing discussions.

The Charpy-V notch (CVN) impact test is widely used in toughness specifications for spring steels, even though the fracturing energy is not directly related to the spring design. The user requirements for springs are in the direction of the operation of springs at a higher tensile strength (1800 MPa and more), which allows the use of only a single parabolic leaf spring, resulting in a lower weight of the vehicle. However, with such a high strength, the toughness is low, and therefore it is necessary to measure the toughness of such springs with a more sensitive method than the Charpy-V impact toughness. The plain-strain stress-intensity factor (K_{Ic}) at the onset of unstable crack growth can be related to the spring design; however, the test values are not used in the toughness specifications.

Introducing a linear elastic fracture mechanic (LEFM) for the evaluation of the heat treatment of springs makes it necessary to draw a distinction between the ductility and the toughness. In this context, the ability of a material to resist the initiation and spread of fracture at gross plastic deformation is ductility and the correct meaning of the toughness is the ability to resist the growth of an existing crack at a tensile load [3,4]. The ductility and toughness are, consequently, two different material properties, even though both, unfortunately, are denominated as toughness. The opposite of both properties is, however, the same, i.e., brittleness.

The most reliable measure of toughness is the plain-strain fracture toughness (K_{Ic})[5]. The minimum size of the specimens depends on the yield stress and the fracture toughness of the material, both of which are required for the plain-strain deformation. A fatigue crack of defined length is propagated from a mechanical notch in the specimens, ensuring that the notch effect is at a maximum and equal for all tests. The same value of fracture toughness should be found for tests on specimens of the same material with different geometries and with a critical combination of crack size and shape and fracture stress. Within certain limits, this is indeed the case, and information about the fracture toughness obtained under standard conditions can be used to predict the failure for different combinations of stress and crack size, and for different geometries[6].

To determine the fracture toughness K_{Ic}, of spring steels, standard CT (Compact Tension) and SENB (Single Edge Notch Bend) specimens and non-standard circumferentially notched and fatigue-precracked tensile-test specimens (K_{Ic}-test specimen) can be used[7].

2.2 Relationship between ultimate fracture stress and defect size

In metal materials there are always defects present, with their importance increasing with increasing strength

and reducing ductility and toughness. In springs the two-dimensional defects are critical. The fracture strength of brittle materials depends on the size and the orientation of the defect. It usually decreases rapidly with the increasing defect size. If LEFM can be applied to calculate the material behaviour, the fracture strength can be calculated with the following equation[8–10](1):

$$\sigma_f = \frac{K_{IC}}{Y \cdot \sqrt{\pi - a}} \quad \text{for: } \sigma_f < \sigma_{Ys} \tag{1}$$

K_{Ic} fracture toughness
a defect size
σ_f fracture stress (tensile strength)
σ_{ys} yield stress
Y correction factor (depending on the geometry: Y = 1.11 for surface cracks)

Equation (1) can be applied if fracture occurs prior to reaching the yield stress. As spring steels are relatively hard (brittle) materials, they can be compared to tool steels with low ductility and toughness. For this reason LEFM can be applied over a wide range of defect sizes.

According to the literature, equation (1) is suitable for describing the fracture behaviour of tool steels for a typical crack-nucleating defect size (e.g., carbide diameter, NMI) above 10 μm to 20 μm. In the case of conventional manufactured tool steels with a banded microstructure, the width of the carbide agglomerates has to be taken as the critical defect size and it has been further noted that the fracture occurs along a path with a high carbide density. The fracture toughness of conventionally produced tool steels depends, therefore, on the specimen orientation[8]. It is highest for a crack propagation perpendicular to the rolling direction and it is lowest for a crack propagation in the rolling direction.

If the fracture stress according to equation (1) approaches the yield stress (e.g., if no larger crack-nucleating particles are present) elastic-plastic methods have to be applied. In this region the material behaviour

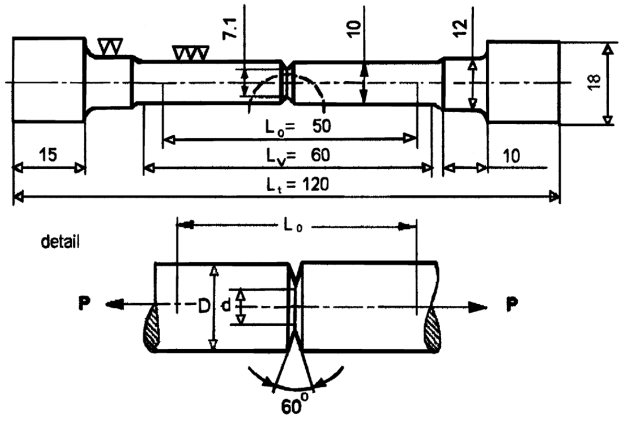

Figure 1: Circumferentially notched and fatigue-precracked K_{Ic}-test specimen. All dimensions are in mm.
Slika 1: Cilindrični natezni preizkušanec za merjenje lomne žilavosti z zarezo po obodu in utrujenostno razpoko v dnu zareze. Vse dimenzije so v milimetrih.

can be described with equation[10] (2), if the ultimate fracture strength is known.

$$\sigma_f = \frac{2}{\pi}\sigma_U \cdot \cos^{-1}\left\{\exp\left[\frac{-\pi\left(\frac{K_{Ic}}{Y}\right)^2}{8 \cdot \sigma_U^2 \cdot a}\right]\right\} \tag{2}$$

σ_U final tensile fracture stress (tensile strength R_m)

For a large defect size equation (2) approximates the results from equation (1). Deviations from equation (1) are found for small defect sizes. Especially for very small defect sizes, the influence of the defect size is almost negligible. A decrease of the fracture strength is observed if a critical defect size is exceeded.

3 EXPERIMENTAL

3.1 Hardness and fracture-toughness tests

The Rockwell-C hardness (HRc) was measured on individual groups of K_{Ic}-test specimens using a Wilson 4JR hardness machine. Circumferentially notched and fatigue-precracked tensile-test specimens[11] with the dimensions indicated in **Figure 1** were used for the investigation.

The advantage of the K_{Ic}-test specimens used here over standardized CT specimens (ASTM E399-90) is in the radial symmetry, which makes them particularly suitable for studying the influence of the microstructure of metallic materials on the fracture toughness. The advantage of these specimens is related to heat transfer, ensuring a completely uniform microstructure.

Due to the high notch sensitivity of hard and brittle metallic materials, such as continuous casted spring steel grade 51CrV4, it is very difficult – sometimes even almost impossible – to create a fatigue crack in the test specimen. However, with K_{Ic}-test specimens the fatigue crack can be created with rotating-bending loading before the final heat treatment[11]; the second advantage of such test specimens is that plain-strain conditions can be achieved using specimens with smaller dimensions than those of conventional CT test specimens[12].

For the linear elastic behaviour up to fracture of such specimens[13] the following equation is applied:

$$K_{IC} = \frac{P}{D^{3/2}}\left(-1.27 + 1.72\frac{D}{d}\right) \tag{3}$$

where P is the load at failure, D is the outside diameter, and d is the notched-section diameter of the test specimen, i.e., the diameter of the ligament next to the crack. Equation (3) is valid as long as the condition $0.5 < d/D < 0.8$ is fulfilled.

Measurements of the fracture toughness were performed at room temperature using an Instron 1255 tensile-test machine. The cross-head speed was 1.0 mm/min for standard tensile tests on specimens with a nominal

Table 1: Chemical composition of continuous-cast spring steel grade 51CrV4 in mass fractions, *w*/%
Tabela 1: Kemična sestava kontinuirno litega vzmetnega jekla 51CrV4 v masnih deležih, *w*/%

Steel grades 51CrMoV4	C	Si	Mn	P		Cr	Mo	V	Ni	AL	Cu	Ti	Sn	Ca	N
Heat 1	0.49	0.30	0.93	0.008	0.004	0.97	0.08	0.1	0.11	0.006	0.17	0.018	0.011	0,0010	0.013
Heat 2	0.50	0.33	0.94		0.008	1.00			0.14	0.009	0.20	0.019	0.010	0.0015	

test length of 100 mm. In the tests two specially prepared cardan fixed jaws, ensuring the axiality of the tensile load, were used. During the tests the tensile-load/ displacement relationship until failure was recorded. In all cases this relationship was linear, and the validity of equation (3) for the tests was confirmed.

3.2 Material, sampling and vacuum heat treatment

Commercial, continuous-cast spring steel grade 51CrV4, delivered as rolled bars of dimensions (20 ×100 × 4000) mm from two heats with similar chemical compositions (**Table 1**) were used. As can be seen from the table there is no difference in the chemical composition of the two heats. The rolled bars were delivered after hot plastic deformation in the as-rolled condition with a mixed martensitic-bainitic microstructure and a hardness of HRc 42–45. Before the sampling, the bars were soft annealed. The bars of each heat were selected at the beginning, middle and end of the rolling.

K_{Ic}-test specimens in the form of circumferentially notched and fatigue-precracked tensile-test specimens were cut from soft annealed bars with $HB_{2.5/187.5}$274–277 in the rolling direction with the fatigue crack at the notch root in the transverse direction.

The specimens were heat treated in a horizontal vacuum furnace with uniform high-pressure gas-quenching using nitrogen (N_2) at a pressure of 5 bar. After the first preheat (650 °C) the specimens were heated (10 °C/min) to the austenitizing temperature of 870 °C, soaked for 10 min, gas quenched to a temperature of 80 °C, and then single tempered for one hour at different temperatures between 200 °C and 575 °C, as shown in **Figure 2**. Sixteen K_{Ic}-test specimens were tested for each tempering temperature.

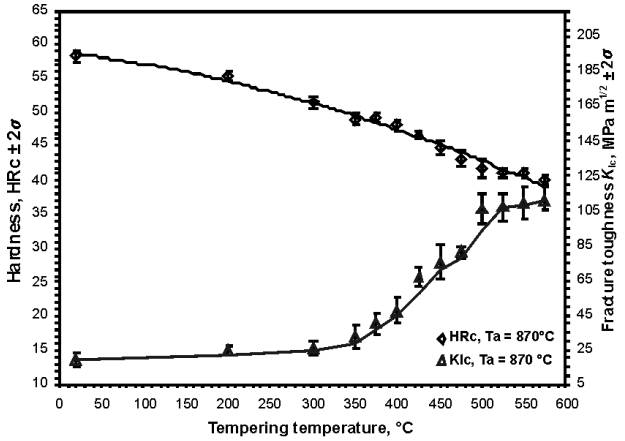

Figure 2: Tempering diagram for two heats of continuous-cast spring steel grade 51CrV4
Slika 2: Diagram popuščanja za dve šarži kontinuirno litega vzmetnega jekla 51CrV4

4 RESULTS AND DISCUSSION

The average measured hardness and fracture-toughness data are shown for the range of hardness (HRc 30–56 ; i.e. R_m = 1275–2161 MPa) in a so-called combined tempering diagram (Rockwell-C hardness – Fracture toughness K_{Ic} – Tempering temperature for austenitizing temperature 870 °C) in **Figure 2**.

From the diagram it is clear that the highest hardness of HRc 58 and the associated fracture toughness K_{Ic} i.e., 18.8 MPa m$^{1/2}$, are achieved in the as-quenched condition after vacuum quenching from the austenitizing temperature of 870 °C. In examining the course of tempering, it is observed that the minimum scatter of results within $\pm 2\sigma$ = 3.2 MPa m$^{1/2}$ is in the as-quenched state and after single tempering at 200 °C. At higher tempering temperatures between 300 °C and 575 °C, the scattering of the K_{Ic} results slightly increased up to $\pm 2\sigma$ = 9.4 MPa m$^{1/2}$, while the scatter of the Rockwell-C hardness is up to $\pm 2\sigma$ = 1.2 HRc in the whole range of used tempering temperatures. Within each group of K_{Ic}-specimens, which were quenched and tempered at the same temperature, this can be attributed to the kinetics of carbide precipitation during tempering at selected temperatures as well as to the heterogeneity of the investigated steel. Since the differences in chemical composition (**Table 1**) are minimal and the austenitizing temperature is the same, it is clear that the fracture toughness K_{Ic} is a very selective mechanical property with regard to the tempering temperature. It should be noted that the K_{Ic}-test specimens were taken from the middle of the bar, and therefore the microstructures of the K_{Ic}-test specimens with the lowest and highest fracture toughness are comparable.

In the as-quenched condition the microstructure consists of untempered martensite and bainite, **Figure 3**. Grain boundaries of the prior austenite grains are not pronounced, and therefore the determination of the austenite grain size according to ASTM E112 was not possible.

Strong positive (bright) and negative (dark) segregations are visible due to the lower etching intensity of the untempered martensite.

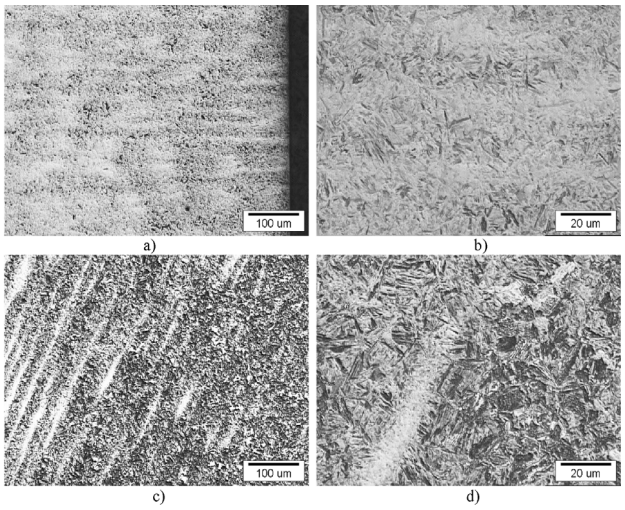

Figure 3: The microstructure of the K_{Ic}-test specimen in the as-quenched condition: a, b) specimen with the lowest fracture toughness (K_{Ic} = 16.2 MPa $m^{1/2}$ and HRc 58.9) c, d) specimen with the highest fracture toughness (K_{Ic} = 22.3 MPa $m^{1/2}$ and HRc 58.1), transverse direction, natal

Slika 3: Mikrostruktura K_{Ic}-preizkušanca v kaljenem stanju: a, b) z najmanjšo lomno žilavostjo (K_{Ic}= 16,2 MPa $m^{1/2}$ in HRc 58,9) c, d) z največjo lomno žilavostjo(K_{Ic} = 22,3 MPa $m^{1/2}$ in HRc 58,1), prečna smer

The fractured surface of the K_{Ic}-test specimens from the same heat with the highest and lowest fracture toughness tempered at 457 °C examined in binocular at 16-times magnification, Figure 4.

From **Figure 4**, it is evident that on the fractured surface of the K_{Ic}-test specimen the highest fracture toughness is higher with the density of positive segregations (black features), the size of segregation is smaller and the distribution is more even in comparison to the

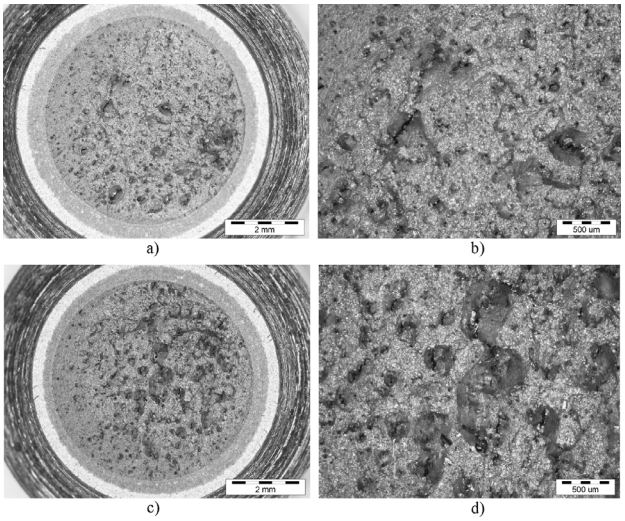

Figure 4: Fractured surfaces of K_{Ic}-test specimen, tempered at 475 °C: a, b) specimen with the lowest fracture toughness (K_{Ic} = 75.7 MPa $m^{1/2}$, HRc 43.8) c, d) specimen with the highest fracture toughness (K_{Ic} = 82.2 MPa $m^{1/2}$, HRc 43.2)

Slika 4: Prelomna površina K_{Ic}preizkušancev, popuščenih na 475 °C: a, b) z najmanjšo lomno žilavostjo (K_{Ic} = 75,7 MPa $m^{1/2}$ in HRc 43,8) c, d) z največjo lomno žilavostjo(K_{Ic} = 82,2 MPa $m^{1/2}$ in HRc 43,2)

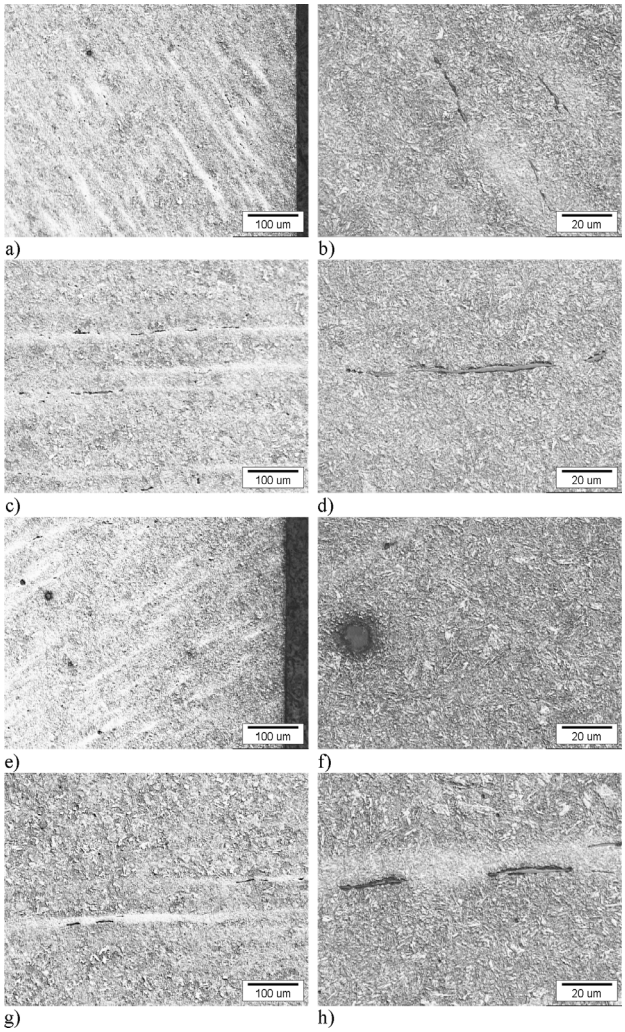

Figure 5: Typical microstructure of K_{Ic}-test specimens a, b) specimen with the lowest fracture toughness (K_{Ic} = 75.7 MPa $m^{1/2}$, HRc 43.8) in transverse direction and c, d) in longitudinal direction and e, f) specimen with the highest fracture toughness (K_{Ic} = 82.2 MPa $m^{1/2}$, HRc 43.2) in transverse direction and g, h) in longitudinal direction

Slika 5: Značilna mikrostruktura K_{Ic} -preizkušanca: a, b) z najmanjšo lomno žilavostjo (K_{Ic} = 75,7 MPa $m^{1/2}$ in HRc 43,8), prečna smer c, d) vzdolžna smer; e, f) z največjo lomno žilavostjo (K_{Ic} = 82,2 MPa $m^{1/2}$ in HRc 43,2), prečna smer; g, h) vzdolžna smer

fractured surface of the K_{Ic}-test specimen with the lowest fracture toughness with nearly the same hardness.

The microstructure of the same K_{Ic}-specimens just below the fractured surface was examined in the optical microscope, **Figure 5**.

The microstructure in the quenched and tempered condition consists of tempered martensite and bainite (≈ 20 %). In the microstructure, non-metallic inclusions of the sulphide type can be observed that are located in positive segregations and oriented in the rolling direction.

The microhardness $HV_{0.025}$ on the positive (bright) and negative (dark) segregations of the K_{Ic}-test specimens with the highest fracture toughness is shown in **Figure 6**. The microhardness in the positive segregations

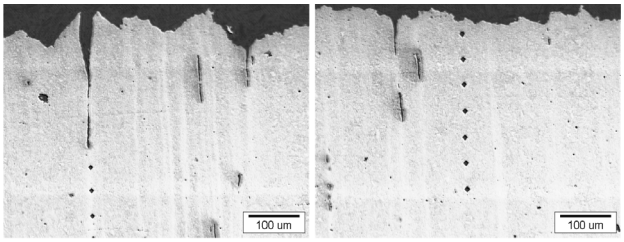

a) b)

Figure 6: Microhardness measurements on positive (bright) a) and negative (darker), b) segregations of the K_{Ic} -test specimens with the highest fracture toughness

Slika 6: Mikrotrdota a) na pozitivnih (svetli pasovi) in b) na negativnih (temnejši pasovi) izcejah K_{Ic}-preizkušanca z največjo lomno žilavostjo

was 554–584 $HV_{0.025}$, in negative segregations it was ≈458 $HV_{0.025}$. From the difference of the microhardness one can conclude that the microstructure in positive segregations consists of tempered martensite and in negative segregations with a lower microhardness of martensite and bainite.

The microstructure of the K_{Ic} -test specimens with the highest fracture toughness was examined in the SEM on positive and negative segregations in the longitudinal direction, **Figure 7**.

At higher magnification it can be seen that the microstructure in the positive segregations consist of tempered martensite and in negative of tempered martensite with islands of bainite, **Figure 8**.

From the comparison of the microstructures of the K_{Ic}-test specimens with the lowest and highest fracture toughness from the same heat and nearly the same hardness and fracture toughnesses, it can be concluded that the density, the size and the distribution of segregations have a significant influence on the fracture toughness. The increase in the fracture toughness can be ascribed to the presence of bainite in the negative segregations.

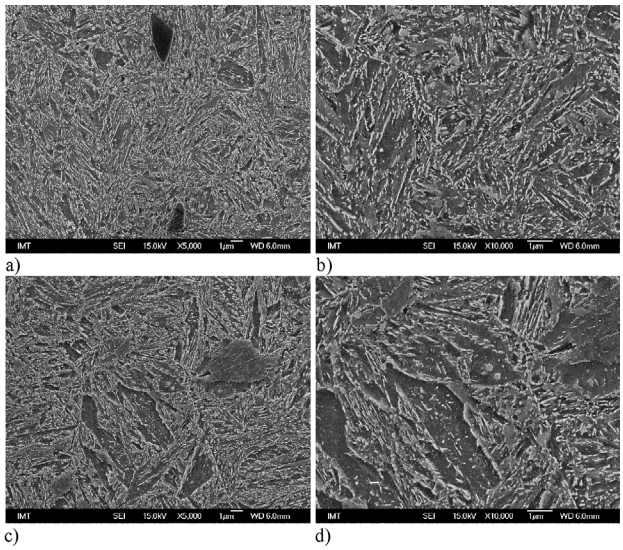

a) b)

c) d)

Figure 7: SEM Microstructure of the K_{Ic}-test specimens with the highest fracture toughness: a, b) positive segregations and c, d) negative segregations, longitudinal direction

Slika 7: SEM-mikrostruktura K_{Ic}-preizkušanca z največjo lomno žilavostjo: a, b) pozitivna izceja, c, d) negativna izceja

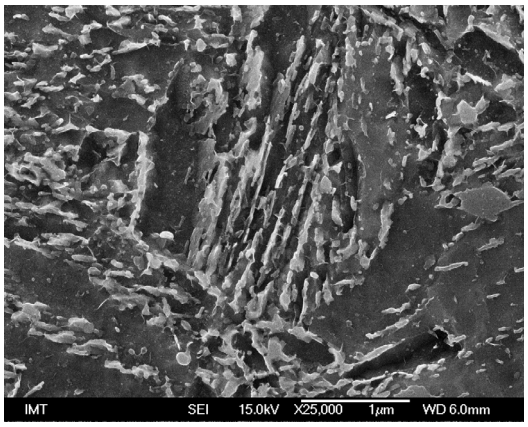

Figure 8: Bainite grain from **Figure 7**

Slika 8: Kristalno zrno bainita s **slike 7**

As mentioned above, if the fracture stress according to equation (1) approaches the yield stress (e.g., if no larger crack-nucleating particles are present), elastic-plastic methods have to be applied. In this region the material behaviour can be described with equation (2), if the ultimate fracture strength is known, **Figure 9**.

In the diagram the decrease of the fracture strength is observed when the critical defect size a_{cr} is exceeded, i.e., a_{cr} = 50 μm and 100 μm, respectively.

5 CONCLUSIONS

The investigated spring steel grade 51CrV4 was successfully vacuum quenched in a horizontal vacuum furnace with uniform high-pressure gas-quenching using nitrogen (N_2) at a pressure of 5 bar. The obtained as-quenched Rockwell-C hardness was HRc 58.4 ± 0.8,

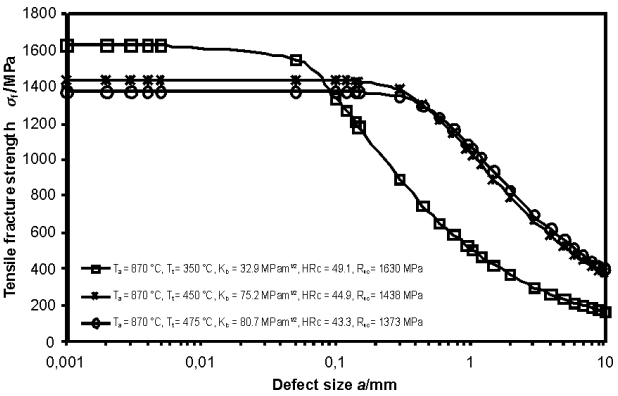

Figure 9: Fracture stress σ_f calculation for the investigated spring steel tempered at various temperatures, ultimate fracture strength (σ_u = R_{uc}) was calculated from the Rockwell-C hardness according to DIN 50150.

Slika 9: Lomna napetost σ_f za preiskovano vzmetno jeklo, popuščeno pri različnih temperaturah; končna natezna napetost (σ_u = R_{uc}) izračunana iz trdote Rockwell-C, DIN 50150

i.e., high enough to obtain, after a single tempering, the required hardnesses from HRc 30 to HRc 50.

The obtained microstructure consists of tempered martensite and bainite (≈ 20 %). Such a microstructure is allowed according to the criteria TB1402 (Scania Standard STD512090 and STD4153) permitting that the microstructure consists of volume fraction $\varphi \approx 80$ % of martensite in the middle of the spring. This condition was met for the investigated spring steel. From the results we can conclude that the investigated spring steel 51CrV4 with a thickness up to 20 mm is suitable for heat treatment in a vacuum furnace with uniform high-pressure gas-quenching using nitrogen (N_2) at a pressure of 5 bar or higher.

The fracture toughness of the steel was determined with a non-standard circumferentially notched and fatigue-precracked tensile-test specimen (K_{Ic}-test specimen). In all cases the load-displacement relationship was linear and the validity of equation (3) for the tests was confirmed. Because of the radial symmetry of the heat transfer, the microstructure of the metallic material along the circumferential area is completely uniform; therefore, the scatter of the fracture toughness could be ascribed to the heterogeneity of the investigated steel only.

For three tempering temperatures and the associated ultimate fracture strength calculated from the Rockwell-C hardness according to DIN 50150, the critical defect size a_{cr} was estimated, i.e., a_{cr} = 50–100 μm, respectively.

The fractured surfaces of the K_{Ic}-test specimens show positive segregations (black features) and confirmed with metallographic analyses as well as with the microhardness $HV_{0.025}$ measurements. The microstructure of the positive segregations consists of tempered martensite with a microhardness $HV_{0.025}$554–584. In the microstructure, non-metallic inclusions of the sulphide type can be observed, which are located in the positive segregations and oriented in the rolling direction. The microstructure in the negative segregations with a lower microhardness consists of low-alloyed tempered martensite and bainite.

In analyzing the fracture surfaces of the K_{Ic}-test specimens of the same heat with the highest and lowest fracture toughness, tempered at the same tempering temperature, as well as from the examined microstructure, which confirmed the presence of positive and negative segregations, we found that specimens with a higher density of positive segregations (black features), which are smaller in size and evenly distributed over the fractured surface, exhibit up to 27 % higher fracture toughness. This finding, which is also very interesting for the automotive industry, will be the subject of a further investigation.

Acknowledgement

Štore Steel, d. o. o., Železarska cesta 3, SI-3220 Štore, Slovenia, is thanked for financial support as well as for the supply of test materials. Thanks also to Prof. dr. Franc Vodopivec and dr. Matjaž Godec for helpful discussions.

6 REFERENCES

[1] A. Sandberg, M. Nzotta, High performance matrix tool steels produced via a clean steel concept, 7th Tooling Conference, Torino, May 2–6, 2006

[2] P. Hansson, New multi-purpose pre-hardened tool steels, 7th Tooling Conference, Torino, May 2–6, 2006

[3] H. Jesperson, Toughness of tool steels, *Proceeding of the 5th International Conference on Tooling*, Leoben, Sept. 29th to October 1st, 1999, University of Leoben, p. 93

[4] R. Ebner, H. Leitner, F. Jeglitch, D. Caliskanoglu, Methods of property oriented tool steel design, *Proceeding of the 5th International Conference on Tooling*, Leoben, Sept. 29th to October 1st, 1999, University of Leoben, p. 3

[5] J. F. Knott, *Fundamentals of fracture mechanic*, Butterworth, 1973

[6] M. Janssen, J. Zuidema, R. J. H. Wanhill: *Fracture mechanics*, 2-nd Edition, Delft University Press, Delft, Netherlands, 2002,15

[7] B. Ule, V. Leskovšek, B. Tuma, *Eng. Frac. Mech.*, 65 (**2000**), 559/72

[8] H. F. Fischmeister, L. R. Olson: Cutting tool materials, *Proc. Int. Conf. on Cutting* Tool Materials, September 15–17(**1980**), Ft. Mitchell, Kentucky, p. 111

[9] S. Kargagöz, H. F. Fischmeister: *Steel Research,* 58 (**1987**) 8, 353

[10] P. Billgren: Hot isostatic pressing of high speed steels, *Proc. First Int. High Speed Steel Conference*, March 26–29, Leoben, Avstrija, (**1990**), 115

[11] V. Leskovsek, B. Ule, B. Liscic, *Journal of Materials Processing Technology*, 127 (**2002**) 3, 298–308

[12] Wei Shen, Tingshi Zhao, Daxing Gao, Dunkang Liu, Poliang Li, Xiaoyun Qiu: *Engng. Fract. Mech.,* 16 (**1982**) 1, 69–92

[13] H. F. Bueckner: *ASTM-STP,* 381 (**1965**), 82

UDK 621.771:621.892
Original scientific article/Izvirni znanstveni članek

ISSN 1580-2949
MTAEC9, 45(1)75(2011)

SIMILARITY CRITERIA AND EFFECT OF LUBRICANT INERTIA AT COLD ROLLING

MERILA PODOBNOSTI IN VPLIV VZTRAJNOSTI MAZIVA PRI HLADNEM VALJANJU

Dušan Ćurčija[1], Ilija Mamuzić[1], Franc Vodopivec[2]

[1]Croatian Metallurgical Society, Berislavićeva 6, 10000 Zagreb, Croatia
[2]Institute of Metals and technology, Lepi pot 11, 1000 Ljubljana, Slovenia
plutonijanac21@net.hr

Prejem rokopisa – received: 2010-09-01; sprejem za objavo – accepted for publication: 2011-01-17

Modern rolling mills operate at speed requiring the consideration of inertial forces for the explanation of the behaviour of lubricant layer in the enter gap of the metal deformation zone. For this calculation a similarity criterium and the improved Mizun-Grudev equation were applied. Good results were obtained in comparison with the numerical Monte Carlo method. A significant point of the calculation is the definition of the initial state in the point of singularity.

Key words: cold rolling, lubrification, lubricant inertia, gripping angle, Reynolds equation, Monte Carlo method

Moderne valjarne obratujejo pri hitrostih valjanja, ki zahtevajo upoštevanje sile vztrajnosti za razlago vedenja plasti maziva na vhodni reži zone deformacije metala. Za izračun sta bili uporabljeni merilo podobnosti in Mizum-Gridevova enačba. Dobljeni so dobri rezultati v primerjavi z numerično metodo Monte Carlo. Pomembna točka izračuna je definicija začetnega stanja v točki singularnosti.

Ključne besede: hladno valjanje, mazanje, vztrajnost maziva, kot oprijema, Reynoldsova enačba, metoda Monte Carlo

1 INTRODUCTION

The lubricant achieves in the enter gap of the metal deformation[1–5] zone a wedge shape determined with the geometry of the rolls and the rolled sheet, as shown in **Figure 1**. The flow of lubricant in the rolling gap can be described with the simplified Reynol's differential [6–9] equations:

$$\frac{\partial p}{\partial x} = \mu \frac{\partial^2 v_x}{\partial y^2} \tag{1a}$$

$$\frac{\partial p}{\partial y} = 0 \tag{1b}$$

$$\frac{\partial v_x}{\partial x} + \frac{\partial^2 v_y}{\partial y} = 0 \tag{1c}$$

$$Z = -\int \frac{\partial v_x}{\partial x} \mathrm{d}y + C(x) \tag{1d}$$

According to the differential equation (1b), the pressure in the lubricant layer is constant over the gap height and that it changes along the layer length, only, and the approximate analytical solution of equation (1a) is:

$$v_x = \frac{1}{\mu} \frac{dp}{dx} \frac{y^2}{2} + C_1(y) + C_2 \tag{1e}$$

Assuming boundary conditions from **Figure 1**

$$\begin{aligned} v_x &= v_0 \quad y = 0 \\ v_x &= v_R \quad y = \varepsilon(x) \end{aligned} \tag{1f}$$

the integration constants are:

$$C_1 = \frac{v_{Rx} - v_0}{\varepsilon(x)} - \frac{1}{\mu} \frac{dp}{dx} \frac{\varepsilon(x)}{2} \tag{1g}$$

$$C_2 = v_0 \tag{1h}$$

Including (1g) and (1h) in (1d) we obtain

$$v_x = \frac{1}{2\mu} \frac{dp}{dx} \left[y^2 - \varepsilon(x) y \right] + \left[\frac{v_{Rx} - v_0}{\varepsilon(x)} \right] y + v_0 \tag{1i}$$

The lubricant consumption along the strip perimeter is:

$$Q(x) = \int_0^{\varepsilon(x)} v_x \, dy = -\frac{1}{12\mu} \frac{dp}{dx} \varepsilon(x) + \left[\frac{v_0 + v_{Rx}}{2} \right] \varepsilon(x) \tag{1j}$$

For $x = 0$ $\qquad Q = \left(\frac{v_0 + v_R}{2} \right) \varepsilon_0$ (1k)

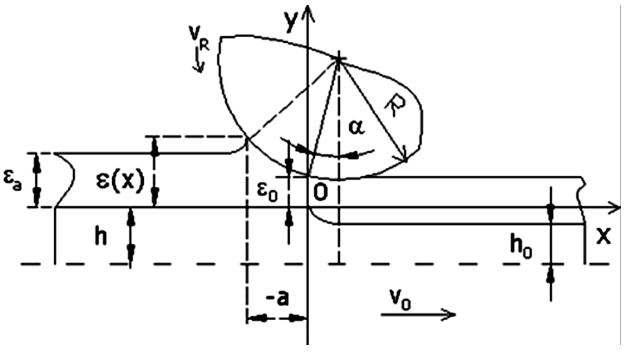

Figure 1: Scheme of cold rolling with lubricant
Slika 1: Shema hladnega valjanja z mazivom

Equalizing (1j) and (1k) we obtain[3–9]:

$$\frac{\mathrm{d}p}{\mathrm{d}x}=\frac{6\mu\left(v_0+v_R\right)}{\varepsilon^2(x)}-\frac{12\mu Q}{\varepsilon^2(x)} \tag{1l}$$

The equation was solved applying numerical methods[10,11] for dressing rolling including inertial forces. The solution is:

$$\frac{\mathrm{d}p}{\mathrm{d}x}=\frac{6\mu\left(v_0+v_R\right)}{\varepsilon^2(x)}+\frac{C_1\mu}{\varepsilon^2(x)}+ +\frac{x\rho}{120R\varepsilon^3(x)}\left[16(v_0+v_\mathrm{R})^2\varepsilon^2(x)-C_1^2\right] \tag{2}$$

$$C_1=\frac{k}{2}-\sqrt{\frac{k^2}{4}+2(v_0+v_R)\varepsilon_0\left[8(v_0+v_R)\varepsilon_0+3k\right]} \tag{3}$$

$$k=120vR \tag{4}$$

The lubricant thickness in the gap range (–a, 0) is:

$$\varepsilon(x)=\varepsilon_0+R\left\{\cos\alpha-\sqrt{1-\left(\sin\alpha-\frac{x}{R}\right)^2}\right\} \tag{5a}$$

This equation can be developed in the power series:

$$\varepsilon(x)=\varepsilon_0-\varepsilon x+\frac{1}{2R}x^2-\frac{1}{2R^2}x^3+\ldots \tag{5b}$$

Neglecting inertia forces, analytical solutions can be developped in the form:

$$(\varepsilon_0)^d=\varepsilon_0^1-\left[(\varepsilon_0^1-\varepsilon_0^1)/\alpha^*\right]\alpha \tag{6}$$

$$\mathrm{A}=\frac{-\alpha}{2\varepsilon_0\psi}+\left[\frac{1}{R\psi x^{1/2}}\right]\Omega+\frac{3\alpha}{2R\psi^2}-\left[3\varepsilon_0/2R^2\psi^2\xi^{1/2}\right]\Omega \tag{7}$$

With: R/m – rolls diameter, v_0 and v_R/(m/s) – rolling speeds, μ_0/(Pa s) – dynamical viscosity of the lubricant, ρ/(kg/m^3) – fluid (lubricant) density, v/(m^2/s) – kinematical viscosity of the lubricant, α (rad) – rolling grip angle, A/m^{-1} – technological parameter, ε_0/m – lubricant layer thickness in the initial section of metal deformation zone, $\varepsilon^1{}_0$/m – lubricant layer thickness for $\alpha\rightarrow 0$, v_x and v_y/(m/s) – speeds in Descartes coordinates x and y, γ/(m^2/N) – pieso coefficient of lubricant viscosity, $\varepsilon_0{}^*$ – lubricant layer thickness in the singularity point α^*, p_0/(N/m^2) – rolling pressure. The parametric symbols are explained in **Table 1**.

These equations can be used for calculations and computer modelling of the behaviour of the lubricant layer in the zone of plastic deformation[1,10,11,12] of metals with cold rolling.

The characteristics of thin sheets rolling process allow to find analytical solutions for equation (1l), however, it is difficult to find a solution for equation (2). For lubricated rolling of sheets, the analytical solutions are acceptable for high gripping angles, while simulation models are mostly used for continous rolling [12,13].

Table 1: Parametrical symbols for **Figure 1** and equations (1) to (7)
Tabela 1: Parametrični simboli za **sliko 1** in enačbe od (1) do (7)

$\varepsilon_0{}^1$	$(\pi^2R/128A^2)^{1/3}$
$\varepsilon_0{}^*$	$(1/2)R(\alpha*)^2$
α^*	$(8/15RA)^{1/3}$
D	Square determinant of equation (6) for the members ($\alpha*$: $\varepsilon_0{}^*$)
ζ	$-\psi$
ψ	$(2/R)\varepsilon_0-\alpha^2$
Ω	$\ln[-\alpha-(\zeta)^{1/2}/(-\alpha+(\zeta)^{1/2}]$
A	$[(1-\exp(-\gamma p_0))/6\mu_0\gamma(v_0+v_\mathrm{R})]$
Linear interaction	$\alpha^*\cong 1.246(\varepsilon_0{}^1/R)^{1/2}$; $\varepsilon_0{}^*\cong 0.7726\ \varepsilon_0{}^1$; $\varepsilon_0{}^*=R(\alpha^*)^2/2$
Mizun-Grudev equation	$\varepsilon^\mathrm{M}{}_0=1/2A\alpha$
$(\varepsilon_0)^\mathrm{d}$	Linearisation for the dressing rolling

2 SIMILARITY CRITERIA

Similarity criteria are frequently used in fluid mecanics calculations. Basic data for calculation related to the behaviour of the lubricant in the metal deformation zone in **Table** 2 for the term $\varepsilon^\mathrm{M}{}_0$ and for the transcendent equation (7) were deduced for the following processing conditions: A = 1.965512 · 10^6 m^{-1}, v_0 = 6 m/s, v_R = 10 m/s, $\alpha_i=(m)\pm^{(1/3)}\alpha$. The iso values are based on investigations aimed to obtain a better equation than that of Mizunov-Grudev given in **Table 2** and analytically more acceptable than the transcendent equation (7). The

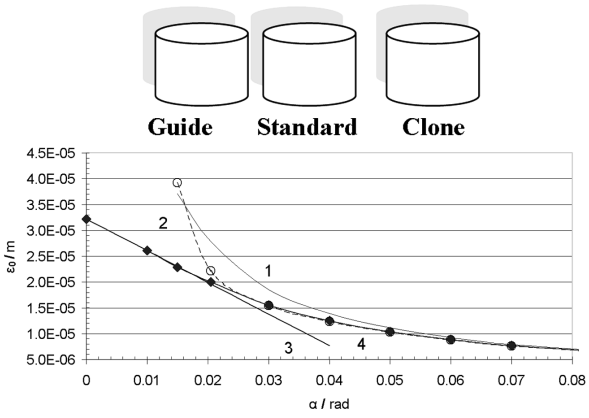

Figure 2: Comparison of different methods for the calculation of the lubricant layer thickness (R = 0.35 m, A = 898519 m^{-1}. 1 – Mizunov-Grudev equation, 2. o – improved Mizunov-Grudev equation (8), 3 – method of linearisation of the equation (6), 4. ♦ – numerical Monte Carlo solution.

Guide	R = 0.35 m	A = 1965512 m^{-1}
Standard	R = 0.35 m	A = 800 000 m^{-1}
Clone	R = 0.35m	A = 898 519 m^{-1}

Slika 2: Primerjava različnih metod za izračun debeline plasti maziva (R = 0.35m, A = 898 519 m^{-1}. 1 – Mizunov-Grudev enačba, 2. o – izboljšana Mizunov-Grudev enačba (8), 3 – metoda of linearizacije enačbe (6), 4. ♦ – numerična Monte Carlo rešitev

Vodilo	R = 0.35 m	A = 1 965 512 m^{-1}
Standard	R = 0.35 m	A = 800 000 m^{-1}
Klon	R = 0.35m	A = 898 519 m^{-1}

Table 2: Etalon (standard) for theoretical investigations of similarity criteria ($m = R/R_i$)
Tabela 2: Etalon (standard) za teoretično raziskavo meril podobnosti ($m = R/R_i$)

R/m	Rolling grip angle/rad							
	0.01	0.02	0.03	0.04	0.05	0.06	0.07	0.08
0.05		1.725186	1.385324	1.234872	1.155365	1.108717	1.079329	1.059809
0.1		1.510205	1.259770	1.153034	1.098537	1.067490	1.048406	1.035988
0.15		1.410961	1.203689	1.117577	1.074549	1.050460	1.035857	1.026462
0.2		1.350680	1.170418	1.096966	1.060832	1.040848	1.028848	1.021185
0.25		1.309130	1.147908	1.083234	1.051802	1.034578	1.024310	1.017789
0.30	1.833992	1.278294	1.131459	1.073322	1.045345	1.030127	1.021105	1.015400
0.35	1.774128	1.254262	1.118808	1.065776	1.040466	1.026783	1.018708	1.013621
0.40	1.725186	1.234872	1.108718	1.059809	1.036633	1.024169	1.016841	1.012238
0.45	1.684164	1.218813	1.100447	1.054955	1.033532	1.022062	1.015341	1.011130
0.50	1.649108	1.205241	1.093520	1.050917	1.030965	1.020324	1.014107	1.010220
0.55	1.618683	1.193583	1.087620	1.047498	1.028800	1.010886	1.013072	1.009458
0.60	1.591942	1.183434	1.082523	1.044561	1.026947	1.017615	1.012190	1.008810
-	-	-	-	-	-	-	-	-
0.8	1.510205	1.153034	1.067490	1.035988				

Table 3: Comparison of different methods to the Monte-Carlo method for bridging the problematic area in **Figure 3** for $a = 0.02$ to $a = 0.035$ rad
Tabela 3: Primerjava različnih metod z metodo Monte-Carlo za premostitve problematične površine na **sliki 3** za $a = 0.02$ do $a = 0.035$ rad

Gripping angle / rad	Equation (6)	Method of linearisation	Monte-Carlo	Equation (8)
$\alpha = 0.02$	$19.909 \cdot 10^{-6}$	$19.949 \cdot 10^{-6}$	$19.916 \cdot 10^{-6}$	-
$\alpha = 0.025$	-	$17.532 \cdot 10^{-6}$	$17.499 \cdot 10^{-6}$	-
$\alpha = 0.03$	-	$15.536 \cdot 10^{-6}$	$15.509 \cdot 10^{-6}$	$15.471 \cdot 10^{-6}$
$\alpha = 0.035$	-	$13.884 \cdot 10^{-6}$	$13.866 \cdot 10^{-6}$	$13.716 \cdot 10^{-6}$
	Second part			
$\alpha = 0.04$	-	$12.304 \cdot 10^{-6}$	$12.501 \cdot 10^{-6}$	$12.341 \cdot 10^{-6}$
$\alpha = 0.045$	-	$11.342 \cdot 10^{-6}$	$11.353 \cdot 10^{-6}$	$11.215 \cdot 10^{-6}$
$\alpha = 0.05$	-	$10.352 \cdot 10^{-6}$	$10.387 \cdot 10^{-6}$	$10.271 \cdot 10^{-6}$
$\alpha = 0.055$	-	-	$9.560 \cdot 10^{-6}$	$9.467 \cdot 10^{-6}$
	Third part			
		Derivation method	Monte-Carlo	Equation (8)
$\alpha = 0.07$		$7.884 \cdot 10^{-6}$	$7.686 \cdot 10^{-6}$	$7.639 \cdot 10^{-6}$
$\alpha = 0.08$		$6.950 \cdot 10^{-6}$	$6.784 \cdot 10^{-6}$	$6.754 \cdot 10^{-6}$
$\alpha = 0.09$		$6.224 \cdot 10^{-6}$	$6.067 \cdot 10^{-6}$	$6.046 \cdot 10^{-6}$

authors have developed the following aproximation for this equation:

$$\left(\frac{4V-10}{\alpha R}\right)(\varepsilon_0^w)^2 + 2\alpha\varepsilon_0^w - A^{-1} = 0$$

$$V = \ln\left(\frac{2\alpha^2\ \mathrm{Re}}{\varepsilon_0^M}\right) \qquad (8)$$

With: e – natural logarithm base.

Tests have shown that the error is for equation (8) in comparison to equation (7) smaller than 1 % for gripping angles $\alpha > 0.03$ rad. Further, equation (8) preserves the same law of iso values than the Mizunov-Grudev equation. It follows, that by applying the criteria of iso values it is possible by cold rolling to pass over from a greater to a smaller gripping angle and to calculate the lubricant layer thickness according to equation (8) using the relation $\alpha_i = (m)^{\pm(1/3)}\alpha$. The values in **Table 2** cannot be calculated using equation (1) developed to a polynome of the third or higher order but only to the square polynome according to equation (5b).

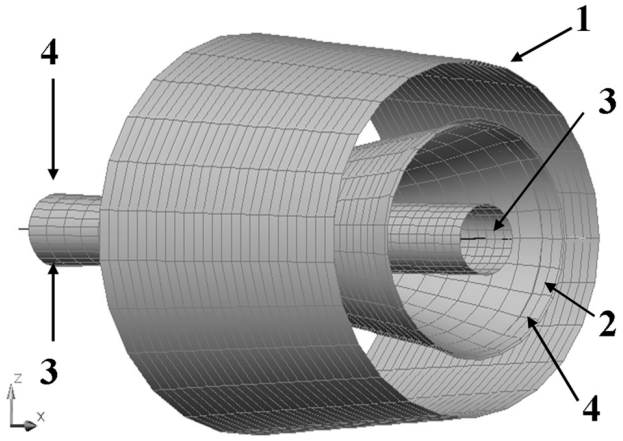

Figure 3: Modelled solutions for **Figure 2** at $\alpha = 0.03$ rad. Same denotations as in **Figure 2**. The tool REVSURF allows the rotation around the linearisatioin method (curve 3).
Slika 3: Modelirane rešitve za **sliko 2** pri $\alpha = 0.03$ rad. Iste označbe kot na **sliki 2**. Orodje REVSURF omogoča rotacijo okoli metode linearizacije (krivulja 3).

In **Figure 2** the comparison of results of the calculation of the lubricant layer thickness according to different methods is shown. The figures show that the linearisation method can be applied only for the dressing rolling. For cold rolling the Mizunov-Grudev solution differs from the numerical solution for aproximately α = 0.06 rad, while equation (8) differs for only α = 0.025 rad. For the range α = 0.02 to α = 0.03 rad on **Figure 2** the criterium of similarity can be used and an approximate solution can be obtained with interpolation from known values.

The criterium of similarity is based on equation (6) and the selected transfer function was a hyperbola. The thickness of the lubricant layer is calculated using the linearisation method and applying the standard data in **Table 2** over the guider to the case on **Figure 2**. The hyperbola is used to transmit the lubricant layer thickness defined by the equation (8), as in this case, or using the boundary conditions for a = 0.02 and a = 0.03, as shown in **Table 3**. In this table the comparison is given of the lubricant layer thickness calculated using the similarity criteria and the Monte Carlo method for the gripping angles indicated. The guider is defined for R = 0.35 and $A = 8 \cdot 10^5$ m^{-1}. It is clear from **Table 3** that the methods of linearisation according to equation (6), of similarity criteria and of the improved Mizunov-Grudev equation are complementar and represent an algorithm for the thickness of the lubricant layer suitable for fast practical application.

In **Figure 3** the AutoCAD modelling of **Figure 2** using different modelling methods is shown. In the initial part of abscissa a good approximation is obtained between the numerical and the linearisation method and that in the border part of abscissa with α = 0.03 the agreement between the corrected equation (9) and the numerical Monte-Carlo calculation is acceptable. Straight lines obtained with linear programming and derivation at the point of singularity are shown in **Figure 4**. The linear representation was selected to obtain the optimal transfer of similarity criteria to the cylinder-clone for which the solution of differential equation is obtained using the known solutions for the guider and the standard on the base of only one solution for the singular point ($\alpha*$, ε^*_0).

This approach is valid for gripping angles in the range 0.0124 rad to 0.0404 rad with allowed angle change for $\Delta\alpha \approx 0.00362$ rad. In the second part of **Table 3** the transfer of similarity criteria from the standard over the guider to the cylinder clone using the straight lines 4, 5 and 6 in **Figure 5**, is shown. If the strainght lines transferring the accuracy from the first to the fourth quadrant become unreliable for the transfer of similarity criteria, it is possible to use, as help, the singular point derivation with direction of transfer of similarity criteria to the first quadrant for which the calculation of the lubricant layer thickness is performed. The singular point transfers well the calculation of the lubricant film, although the gripping angle is relatively distant. It is usefull to remind that the method of derivation in **Table 3** offers the possibility of increasing the mathematical accuracy in comparison to the Monte-Carlo method. In this case, the simple analytical definition would approach a form approaching equation (8). Further, data in **Table 3** show that the improved equation (8) can, for smooth surfaces of rolls and of rolled metal, substitute the Monte Carlo method. In this case, the transfer of similarity criteria for the standard and the guider can be calculated using equation (8), while the clone cylinder is defined mathematically with differential equations connecting the longitudinal and transverse roughness and with possible analytical solutions for the point of singularity.

The solution of differential equations related to the equation (1a), as for instance equation (2), can be obtained through the solution for one point, as boundary condition, in this case the solution for the singular point. If the accuracy as in **Table 1** is expected, the calculation of the lubricant layer for smooth surfaces can not be simplified further.

Using a complex method of statistical analysis of data in **Table 2** and for the rolls of diameter of R = 0.3 m the following relation was developed for the lubricant layer thickness:

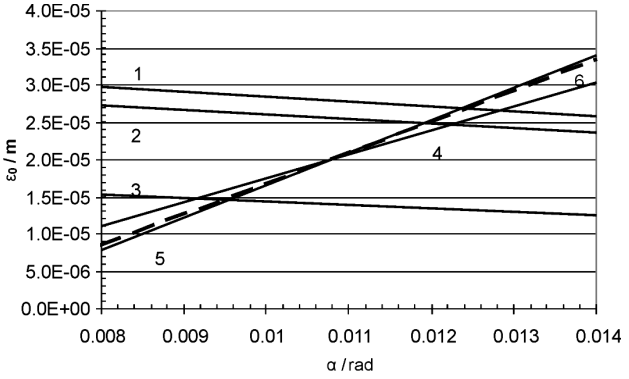

Figure 4: The method of linearisation (1, 2, 3) through the points (0 : ε^1_0) and ($a*$: ε^*_0) and of derivation in the point ($a*$: ε^*_0) (4, 5, 6)
Standard (3, 4), guider (1, 5), Clone cylinder (2, 6)
Slika 4: Metoda linearizacije (1, 2, 3) skozi točke (0 : ε^1_0) in ($a*$: ε^*_0) in derivacije v točki ($a*$: ε^*_0) (4, 5, 6).
Standard (3, 4), vodilo (1, 5), valj klon (2, 6)

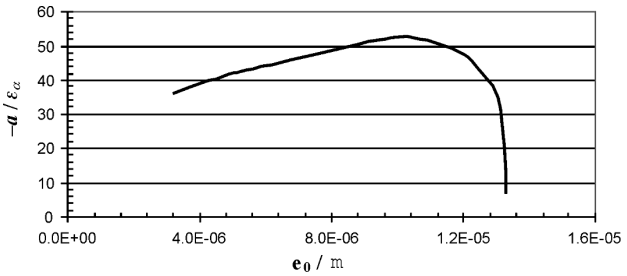

Figure 5: Relationship lubricant layer thickness – rolling gap geometrical shape
Slika 5: Odvisnost debeline plasti maziva od geometrične oblike valjalniške reže

$$\frac{\varepsilon_0^M}{\varepsilon_0^T} = (S\alpha^{1/2} + B)/\alpha + (C\alpha^{1/2} + L)/\alpha^2$$

$$Q = \alpha^{1/2} \qquad W = (\varepsilon_0^{\mathrm{M}} / \varepsilon_0^{\mathrm{T}})\alpha^2 \tag{9}$$

The results of the calculation are shown in **Table 4**.

Table 4: Some statistical data on the regression analysis
Tabela 4: Nekateri statistični podatki o regresijski analizi

S	0.8519
B	–0.2633
C	0.0346
L	–0.0015
R_{sq}	0.99999
F	66829.2
d. f.	5
Q, *W*	Abscissa and ordinate

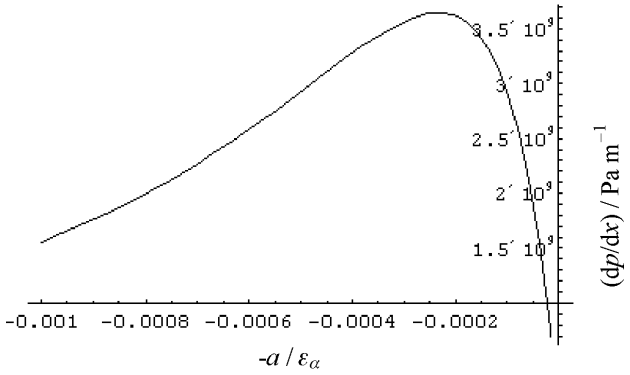

Figure 6: Change of pressure gradient for the gripping angler α = 0,02 rad and rolls diameter R = 0.2 m in dependence of the ratio $(-a) / (\varepsilon_{-a})$ in the range of – 0.001 m to – 0.000015 m and other parameters as for **Table 2**
Slika 6: Sprememba gradienta pritiska za kot oprijema α = 0,02 rad in premer valjev R = 0,2 m v odvisnosti od razmerja $(-a)/(\varepsilon_{-a})$ v območju od –0.001 m do – 0.000015 m in drugih pamaterov kot za **tabelo 2**

3 EFFECTS OF LUBRICANT INERTIA

The effect of lubricant inertia depends on the speed of the processing, the gap geometry and the rheological characteristics of the lubricant. In this work only investigations of the effect in the gap geometry is discussed. It was deduced with a numerical solution of the equation (1) applying the Monte-Carlo method with A = 1 965 512 m^{-1}, R = 0.2 m, ρ = 854 kg/m^3, dressing angle 0.02 rad and other data as in **Table 2** and it is shown in **Figure 4**.

The reliable analysis range lies both sides near of the point 2 in **Figure 5**. On the arc 2∩3 of the curve, by increasing of the strip lubricant layer thickness, the thickness of the lubricant layer in the initial section of the metal deformation zone is increased and the effect of inertia forces is decreased, while, on the arc 2∩1 of the curve the effect is opposite. For a selected processing, the vertex at the point 2 can be deduced with a regression analysis for determined processing parameters. In **Table 5** data on the effect of inertia forces on ε_0 calculated from equations (1a) and (2) using the Monte-Carlo method are given. The calculation was similar as for the curves in **Figure 2** and the data in **Table 2**. For the arc 2∩3 and dressing processing the correction for the lubricant layer thickness would be unnecessary, while, considering the inertia forces it is significant for the arc 2∩1. If the working velocity is increased from 16 m/s, as in **Table 5**, to 50 m/s for the angle 0,05 rad ε_0 = 13.854 · 10^{-6} m is deduced, while the consideration of inertia forces gives $\varepsilon^{\mathrm{IN}}{}_0$ = 14,951 · 10^{-6} m.

Data in **Table 5** show that the shape of the gap in the area (–*a*, 0) prevails over the lubricant rheological cha-

Table 5: Effect of inertia forces($\varepsilon^{\mathrm{IN}}{}_0$) for dressing rolling
Tabela 5: Vpliv sil vztrajnosti ($\varepsilon^{\mathrm{IN}}{}_0$) za oblikovalno valjanje

α/rad	0	0.011335	0.02	0.03	0.04	0.05
ε_0 /m	15.863 · 10^{-6}	12.255 · 10^{-6}	9.416 · 10^{-6}	7.244 · 10^{-6}	5.797 · 10^{-6}	4.695 · 10^{-6}
$\varepsilon^{\mathrm{IN}}{}_0$ /m	15.863 · 10^{-6}	12.335 · 10^{-6}	9.542 · 10^{-6}	7.447 · 10^{-6}	5.959 · 10^{-6}	4.906 · 10^{-6}

Table 6: Dependence of the lubricant layer thickness on the gripping angle and the lubricant layer thickness on the strip ahead the deformation zone. Calculated using equations (1a) i (2).
Tabela 6: Odvisnost debeline plasti maziva od kota oprijema in debeline plasti maziva na traku pred zono deformacije. Izračunano z uporabo enačb (1a) in (2).

α/rad	ε_a/ m	ε_a/m	ε_a/m	ε_a/m	ε_a/m
	0.001	0.002	0.003	0,004	0.005
Without inertia	12.613· 10^{-6}	12.642· 10^{-6}	12.648· 10^{-6}	12.651· 10^{-6}	12.652· 10^{-6}
α = 0.01	12.793 · 10^{-6}	12.853 · 10^{-6}	12.884 · 10^{-6}	12.903 · 10^{-6}	12.912 · 10^{-6}
Without inertia	9.390 · 10^{-6}	9.407 · 10^{-6}	9.412 · 10^{-6}	9.414 · 10^{-6}	9.415 · 10^{-6}
α = 0.02	9.491 · 10^{-6}	9.539 · 10^{-6}	9.562 · 10^{-6}	9.578 · 10^{-6}	9.589 · 10^{-6}
Without inertia	7.225 · 10^{-6}	7.238 · 10^{-6}	7.241 · 10^{-6}	7.242 · 10^{-6}	7.243 · 10^{-6}
α = 0.03	7.286 · 10^{-6}	7.322 · 10^{-6}	7.340 · 10^{-6}	7.352 · 10^{-6}	7.361 · 10^{-6}
Without inertia	5.786 · 10^{-6}	5.793 · 10^{-6}	5.795 · 10^{-6}	5.796 · 10^{-6}	5.796 · 10^{-6}
α = 0.04	5.820 · 10^{-6}	5.848 · 10^{-6}	5.862 · 10^{-6}	5.871 · 10^{-6}	5.878 · 10^{-6}
Without inertia	4.788 · 10^{-6}	4.793 · 10^{-6}	4.794 · 10^{-6}	4.795 · 10^{-6}	4.795 · 10^{-6}
α = 0.05	4.809 · 10^{-6}	4.830 · 10^{-6}	4.841 · 10^{-6}	4.848 · 10^{-6}	4.854 · 10^{-6}

racteristics and the kinematics of the processing because the gripping angle approaches to zero. For this reason, the inertia forces do not affect significantly the lubricant behaviour by dressing processes, while these forces shold be considered by cold rolling. In **Table 6** the effect of ε_a (lubricant layer thickness on the sheet) on ε_0 (lubricant layer thickness at entrance cross section) is shown, as deduced using equation (2) and the Monte-Carlo calculation with $R = 0.2$ m and other data, as for **Table 5**. The value of ε_0 is increased for ≈1–2 %, while the value of ε_a increases for the sheet for five times for the rolling velocity up to 16 m/s.

In **Table 6** the effect of lubricant height on the sheet on the lubricant sheet on the entering section of the deformation zone is shown as function of lubricant inertia and gripping angle. The inertia effect increases significantly with the gripping angle and even faster with the lubricant height on the sheet ahead the rolls.

On **Figure 6** the change of pressure gradient ahead the rolling gap is shown with the maximum for x = –0.00025 m.

It is very difficult to obtain approximate analytical solutions of the differential equation (2). For this reason, it is analysed applying the numerical Monte-Carlo integration. The analysis should be complemented[13] considering surface roughness and with correlations with dependences to dynamkcal viscosity and rolling pressure.

4 CONCLUSIONS

On the base of the results of the calculations presented the following conclusions are proposed:

- The criteria of similarity are transferred acceptably with the solution of the equation (1a) from the standard over the guider to the cylinder clone applying the method of linearisation up to a gripping angle determined by linear programming. For a greater gripping angle the transfer of similarity criteria can be achieved using straight lines obtained with derivation in the point of singularity.
- The effect of inertia forces can be neglected for lower dressing speed, while this effect becomes significant for incresead speed of cold rolling.
- The use of the improved Mizunov-Grudev equation (8) gives solutions in good agreement with the numerical solution of equation (1) applying the Monte-Carlo method. Also, it is more practical for use than the transcendent equation (7).
- For a determined relation rolls diametere versus gripping angle very similar results are obtained using the Mizunov – Grudev relation and the transcendent equation (7).

5 REFERENCES

[1] D. Ćurčija, I. Mamuzić, Schemes of metal-working processes and the related tribological equations of fluid mechanics, Mater. Tehnol., 43 (**2009**) 1, 23–30

[2] R. Boman, Jean-Philippe Ponthot, Numerical simulation of lubricated contact in rolling processes, J. Mater. Process. Techn., 125–126 (**2002**), 405–411

[3] S. Thiruvarudchelvan, M. J. Tan, Recent developments in friction-assisted sheet metal forming processes, J. Mater. Process. Techn., 167 (**2005**) 2–3, 161–166

[4] Dengyue Sun, Xun Chen, Fengshan Du, Guangming Zhu, Jiangang Zhou, Dynamic thickness simulation of five-stand continuous cold rolling, J. Mater. Process. Techn., 167 (**2005**) 2–3, 218–223

[5] W. R. D. Wilson, Friction and lubrication bulk metal forming process, J. Appl. Met. Work, 1 (**1979**), 7–19

[6] D. Ćurčija, I. Mamuzić, Lubrication flow during the rolling of seamless tubes, Mater. Tehnol., 42 (**2008**) 2, 59–63

[7] S. V. Mazur, Postanovka zadači i zakonomernosti tečenija smazki v očage deformacii pri prokatke trub, Sučasni problemi metalurgii, Plastična deformacija metaliv, 8 (**2005**), 447–452

[8] O. P. Maksimenko, A. A. Semenča, Issledovanie kontaktno-gidrodinamičeskoj smazki pri prokatke, Sučasni problemi metalurgii, Plastična deformacija metaliv, 8 (**2005**), 99–103

[9] W. Huang, D. B. Bogy, Three-dimensional direct simulation Monte Carlo methods for slider air bearings, Phys. Fluids, 9 (**1997**) 6, 1764–1769

[10] M. I. Sobol: Die Monte Carlo Metode, Ver. H. Deutsch, Frankfurth a. Main, 1986

[11] D. Ćurčija, I. Mamuzić, Mathematical Modelling of Metal Drawing Process, Metalurgija, 44 (**2005**) 2, 113–118

[12] M. R. Jensen, L. Olovsson, J. Danckert, Numerical model for the oil pressure distribution in the hydromechanical deep drawing process, J. Mater. Process. Techn., 103 (**2000**), 74–79

[13] P. Heyer, J. Läuger, Corelation between friction and flow of lubricating greases in a new tribometer device, Lubrication Science, 21 (**2009**) 7, 253–268

The authors are indebted to professor **Marica Pešić** and professor **Desanka Radunović** of the Faculty of Natural Sciences and Matematics of the University of Belgrade for reviewing the mathematical treatment.

In memoriam
OSKAR KÜRNER
1925–2010

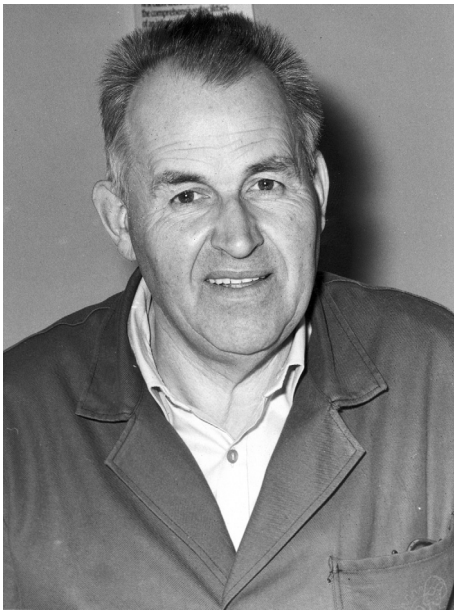

Konec septembra nas je zapustil Oskar Kürner, univ. dipl. inž. metalurgije in višji strokovni sodelavec v Raziskovalnem oddelku Železarne Jesenice.

Rodil se je 21. 10. 1925 v Ljubljani. Po diplomi leta 1956 se je zaposlil v Železarni Jesenice kot asistent martinarne in kasneje v metalurškem oddelku tehnične kontrole. V istem letu je bil imenovan za višjega strokovnega sodelavca in leta 1983 za vodjo sektorja tehnične kontrole, kjer je ostal do upokojitve leta 1989.

Njegovo strokovno delo je bilo pestro in inovativno. Najprej je prevzel nalogo, da dopolni proizvodnjo elektropločevine, tako da je bilo opuščeno valjanje jekla v obliki pločevine, ki je bilo nadomeščeno z izdelavo v obliki hladno valjanih trakov. Tehnološko je dopolnil izdelavo jekla tako, da se bile elektromagnetne karakteristike jekla v skladu s takratnimi DIN-normami.

Postavil in opremil je eksperimentalno linijo v raziskovalnem oddelku, tako da je bilo mogoče spreminjati posamezne parametre za doseganje najboljših elektromagnetnih karakteristik jekla.

Brez dvoma je s svojimi rezultati prispeval k tehnologiji procesov v hladni valjarni na Beli in so se rezultati kot mozaik vgrajevali v temelje razvoja hladne valjarne Bela in kasneje v ACRONI ter tudi v odločitve o konfiguraciji tehnoloških procesov v novi jeklarni.

Usmeril se je predvsem v razvoj elektropločevin, od mehkega relejnega železa, siliciranih dinamopločevin do poizkusov izdelave transformatorske pločevine v skladu z mednarodnimi standardi. Uspelo mu je pridobiti nove merilne naprave. Začel je ustvarjati interne predpise in z njimi dosegati kvaliteto elektropločevin po mednarodnih standardih. Z novimi merilnimi napravami so se opravljale meritve po metodi Epstein in z njimi je lahko posredoval porabnikom elektropločevin podatke o kvaliteti, ki so bili kompatibilni s svetovnimi normami za te materiale.

Da bi lahko uresničil nadaljnji razvoj elektropločevine v železarni, je projektiral in v okviru eksperimentalne delavnice v oddelku tudi udejanil pripravo laboratorija za te namene, saj je bilo mogoče žarenje pločevin v različnih plinskih mešanicah in pri različni vsebnosti vlage. V žarilni peči je bilo mogoče po kontinuirnem postopku izvajati različno toplotno obdelavo za doseganje optimalnih magnetnih lastnosti pločevine ter pripraviti tehnološka navodila za industrijsko proizvodnjo. Ugotavljati je bilo mogoče tudi vpliv oligoelementov na proces staranja jekla in vpliv na elektromagnetne karakteristike.

Inženir Kürner je deloval tudi na naslednjih področjih:

- vodil je raziskovalni oddelek, ki ga je opremil za izvajanje posebnih raziskovalnih in tehnoloških posegov;
- ustanovil je oddelek za statistične preiskave in spremljanje tehnoloških parametrov v proizvodnji jekla;
- uvedel je pripravo interne tehnološke dokumentacije za izdelavo in predelavo jekla v obliki regulativov oziroma internih standardov; ti so obsegali tudi interno kontrolo proizvodov v železarni.
- reševal je tekočo proizvodno problematiko v železarni in sodeloval pri razvoju novega jekla.
- v letu 1961 je začel razvijati novo vrsto jekla za rudarske verige in jekla za kroglične ležaje; rudarske verige so bile izvozni izdelek tovarne.

Delo inž. Kürnerja je bilo zelo raznoliko in obsežno, saj je bil vključen v reševanje različnih proizvodnih problemov, ki so se pojavljali v vsakdanji proizvodnji.

Bil je mehkega značaja, razumel je težave in stiske sodelavcev, pod njegovim vodstvom pa so se le-ti tudi strokovno izpopolnjevali.

Za svoje raziskovalno delo je prejel Pantzovo priznanje za leto 1981, najvišjo nagrado, ki mu jo je podelila Železarna Jesenice.

Veliko dogodkov je povezanih z delom pokojnega Oskarja. Zato lahko trdimo, da je bil eden izmed zaslužnih stebrov, ki so nosili razvoj železarne na Jesenicah in s tem ohranjali železarstvo na Gorenjskem. V razvoj stroke je vložil veliko truda in znanja, ki se prenaša na naslednike in je to dejansko kapital podjetja.

Nam, ki smo ga poznali, bo ostal v trajnem spominu.

Prof. dr. inž. Marin Gabrovšek